Astronomy & Astrophysics

The Close AGN Reference Survey (CARS)

No obvious signature of AGN feedback on star formation, but subtle trends

I. Smirnova-Pinchukova[1], B. Husemann[1], T. A. Davis[2], C. M. A. Smith[2], M. Singha[3], G. R. Tremblay[4],
R. S. Klessen[5,6], M. Powell[7], T. Connor[8,9], S. A. Baum[3], F. Combes[10], S. M. Croom[11], M. Gaspari[12,13],
J. Neumann[14], C. P. O'Dea[3], M. Pérez-Torres[15,16], D. J. Rosario[17], T. Rose[17], J. Scharwächter[18], and N. Winkel[1]

[1] Max-Planck-Institut für Astronomie, Königstuhl 17, 69117 Heidelberg, Germany
  e-mail: smirnova@mpia.de
[2] School of Physics & Astronomy, Cardiff University, Queens Buildings, The Parade, Cardiff CF24 3AA, UK
[3] Department of Physics & Astronomy, University of Manitoba, Winnipeg, MB R3T 2N2, Canada
[4] Center for Astrophysics | Harvard & Smithsonian, 60 Gardent St., Cambridge, MA 02138, USA
[5] Universität Heidelberg, Zentrum für Astronomie, Institut für Theoretische Astrophysik, Albert-Ueberle-Str. 2, 69120 Heidelberg,
  Germany
[6] Universität Heidelberg, Interdisziplinäres Zentrum für Wissenschaftliches Rechnen, Im Neuenheimer Feld 205, 69120 Heidelberg,
  Germany
[7] Kavli Institute of Particle Astrophysics and Cosmology, Stanford University, 452 Lomita Mall, Stanford, CA 94305, USA
[8] Jet Propulsion Laboratory, California Institute of Technology, 4800 Oak Grove Drive, Pasadena, CA 91109, USA
[9] Department of Physics & Astronomy, Michigan State University, 567 Wilson Road, East Lansing, MI 48824, USA
[10] Observatoire de Paris, LERMA, Collège de France, CNRS, PSL University, Sorbonne University, 75014 Paris, France
[11] Sydney Institute for Astronomy, School of Physics, A28, The University of Sydney, Sydney, NSW 2006, Australia
[12] INAF – Osservatorio di Astrofisica e Scienza dello Spazio, Via P. Gobetti 93/3, 40129 Bologna, Italy
[13] Department of Astrophysical Sciences, Princeton University, 4 Ivy Lane, Princeton, NJ 08544-1001, USA
[14] Institute of Cosmology and Gravitation, University of Portsmouth, Burnaby Road, Portsmouth PO1 3FX, UK
[15] Instituto de Astrofísica de Andalucía, Glorieta de las Astronomía s/n, 18008 Granada, Spain
[16] Departamento de Física Teórica, Facultad de Ciencias, Universidad de Zaragoza, 50009 Zaragoza, Spain
[17] Center for Extragalactic Astronomy, Durham University, Durham DH1 3LE, UK
[18] Gemini Observatory/NSF's NOIRLab, 670 N. A'ohoku Place, Hilo, HI 96720, USA

ABSTRACT

Context. Active galactic nuclei (AGN) are thought to be responsible for the suppression of star formation in massive $\sim 10^{10}\,M_\odot$ galaxies. While this process is a key feature in numerical simulations of galaxy formation, it has not been unambiguously confirmed in observational studies yet.
Aims. The characterization of the star formation rate (SFR) in AGN host galaxies is challenging as AGN light contaminates most SFR tracers. Furthermore, the various SFR tracers are sensitive to different timescales of star formation from approximately a few to 100 Myr. We aim to obtain and compare SFR estimates from different tracers for AGN host galaxies in the Close AGN Reference Survey (CARS) to provide new observational insights into the recent SFR history of those systems.
Methods. We constructed integrated panchromatic spectral energy distributions to measure the far infrared (FIR) luminosity as a tracer for the recent (<100 Myr) SFR. In addition we used the integral-field unit observation of the CARS targets to employ the Hα luminosity decontaminated by AGN excitation as a proxy for the current (<5 Myr) SFR.
Results. We find that significant differences in specific SFR of the AGN host galaxies as compared with the larger galaxy population disappear once cold gas mass, in addition to stellar mass, is used to predict the SFR for a specific AGN host. Only a tentative trend with the inclination of the host galaxy remains, such that SFR appears slightly lower than expected when the galaxies of unobscured AGN appear more edge-on along our line-of-sight, particular for dust-insensitive FIR-based SFRs. We identify individual galaxies with a significant difference in their SFR which can be related to a recent enhancement or decline in their SFR history that might be related to various processes including interactions, gas consumption, outflows, and AGN feedback.
Conclusions. AGN can be present in various stages of galaxy evolution which makes it difficult to relate the SFR solely to the impact of the AGN. Our study shows that stellar mass alone is an insufficient parameter to estimate the expected SFR of an AGN host galaxy compared to the underlying non-AGN galaxy population. We do not find any strong evidence for a global positive or negative AGN feedback in the CARS sample. However, there is tentative evidence that (1) the relative orientation of the AGN engine with respect to the host galaxies might alter the efficiency of AGN feedback and that (2) the recent SFH is an additional tool to identify rapid changes in galaxy growth driven by the AGN or other processes.

Key words. galaxies: active – galaxies: evolution – galaxies: star formation – surveys – techniques: photometric – techniques: imaging spectroscopy

1. Introduction

The evolution of galaxies is driven by many different physical processes, which we can indirectly study by probing various galactic properties across cosmic time. One key parameter is the star-formation rate (SFR), which changes with redshift and discloses essential information about the evolution of galaxies (e.g., Madau & Dickinson 2014). Furthermore, at lower redshifts the galaxy population shows a clear bi-modality in the color-magnitude diagram (e.g., Strateva et al. 2001; Baldry et al. 2004; Wyder et al. 2007; Brammer et al. 2009) of which the specific SFR versus stellar mass (sSFR–$M_\star$) diagram (e.g., Brinchmann et al. 2004; Noeske et al. 2007; Karim et al. 2011; Renzini & Peng 2015) is a more physical representation. Such diagrams separate star-forming from passive galaxies where the so-called star-forming main sequence (SFMS, Noeske et al. 2007) indicates the average location of star-forming galaxies as a function of stellar mass. Moreover, the SFMS tends to be present across a wide range of redshifts as a tight correlation (e.g., Elbaz et al. 2007; Speagle et al. 2014). How this galaxy bi-modality is established is one of the open key questions in our current galaxy evolution model. One option is that accreting super-massive black holes (SMBHs) release enough energy to suppress the star formation in their host galaxies as they pass quickly through from the blue cloud to the red sequence (e.g., Faber et al. 2007; Schawinski et al. 2014), but also opposite tracks via rejuvenation of star forming have been proposed (e.g., Hasinger 2008; Mancini et al. 2019; Chauke et al. 2019). Furthermore, environmental processes (e.g., Balogh et al. 2004; Peng et al. 2010; Schaefer et al. 2019) and gas consumption (e.g., Colombo et al. 2020) may facilitate this transformative process.

The ability both to rapidly quench and maintain low levels of star formation in red-sequence massive galaxies has often been attributed to the impact of active galactic nuclei (AGN). Radiatively-driven winds, mechanical energy, and/or thermal pressure release from the AGN are physical processes routinely incorporated into numerical simulations of galaxy evolution to solve the overcooling problem (e.g., Vogelsberger et al. 2014a; Schaye et al. 2015; Pillepich et al. 2018; Bassini et al. 2019; Wittor & Gaspari 2020), so that the characteristics of the observed galaxy population can be reproduced (e.g., Vogelsberger et al. 2014b; Nelson et al. 2018). Often two types of the AGN feedback mode are being distinguished, which are called the quasar mode or radiative mode (e.g., Di Matteo et al. 2005; Hopkins et al. 2008; Hopkins & Elvis 2010) and the radio mode also known as kinetic or maintenance mode (e.g., Bower et al. 2006; Croton et al. 2006; Fabian 2012; Gaspari et al. 2020). The quasar mode is thought to initially quench star formation through powerful radiatively driven winds that remove the gas from the galaxy (e.g., Nesvadba et al. 2008; Feruglio et al. 2010; Maiolino et al. 2012) and thereby suppress star formation. The radio mode is a heating mechanism affecting the gaseous halo that prevents continuous condensation of cold and warm gas, thereby quenching star formation over long timescales and maintaining a low level of star formation in red sequence galaxies (e.g., Brüggen & Kaiser 2002; McNamara et al. 2005; Gaspari et al. 2019; McDonald et al. 2021). Strong observational evidence for radio mode feedback has been collected from galaxy clusters hosting powerful radio galaxies (e.g., Fabian et al. 2006; McNamara & Nulsen 2007). The role of quasar mode feedback is much more controversial from an observational perspective. Various studies have reported negative (Ho 2005; Nandra et al. 2007; Schawinski et al. 2009; Farrah et al. 2012; Page et al. 2012; Mullaney et al. 2015; Shimizu et al. 2015; Wylezalek &

Zakamska 2016; Kakkad et al. 2017; Catalán-Torrecilla et al. 2017; Bing et al. 2019; Bluck et al. 2020; Ramos Padilla et al. 2020; Brownson et al. 2020; Smith et al. 2020), positive (Kim et al. 2006; Cresci et al. 2015a,b; Bernhard et al. 2016; Santoro et al. 2016; Maiolino et al. 2017; Koss et al. 2021), or no effect from feedback (Elbaz et al. 2011; Bongiorno et al. 2012; Harrison et al. 2012; Husemann et al. 2014; Balmaverde et al. 2016; Leung et al. 2017; Woo et al. 2017; Shangguan et al. 2018; Scholtz et al. 2020) on the star formation rates of observed AGN host galaxies.

One common difficulty in observational studies is the measurement of the basic AGN host galaxy parameters such as SFR and stellar mass, because the AGN light can dominate the total emission of the host galaxy across nearly the entire electromagnetic spectrum from radio to X-rays. Hence, it can be challenging to measure the SFR or stellar mass from commonly used proxies and various strategies have been used in the literature to mitigate the issue. The stellar mass can be easily determined from optical spectra or NIR-optical photometry in obscured AGN (e.g., Kauffmann et al. 2003; Silverman et al. 2009; Aird et al. 2012; Mignoli et al. 2013) as the light from the central AGN is blocked by dust along our line of sight. However, the drawback is that AGN parameters such as black hole (BH) mass can usually not be directly inferred for obscured AGN, except for few very nearby systems using the narrow-line region (NLR) kinematics (e.g., Barth et al. 2001; Walsh et al. 2013).

The SFR of a galaxy is usually determined either from the UV radiation of young stars (e.g., Salim et al. 2007), the ionizing photons from H II regions using Hα or [O II] (e.g., Kennicutt & Kent 1983; Kewley et al. 2004), the reheated warm and cold dust at MIR and FIR wavelengths (e.g., Kennicutt 1998a), or the radio emission produced in supernova explosions (e.g., Condon 1992). All those tracers can be significantly contaminated by AGN emission even in obscured AGN. The UV or radio emission can be spatially separated through high-angular observations (Fernández-Ontiveros et al. 2018; Rosario et al. 2021). Alternatively, the overall spectral energy distribution (SED) is decomposed into various emitting components of a galaxy including AGN, star-formation heated dust and stars. Examples of such SED fitting codes are (X-)Cigale (Noll et al. 2009; Yang et al. 2020), Magphys (da Cunha et al. 2008), AGNfitter (Calistro Rivera et al. 2016) or FortesFit (Rosario 2019), which can be used to infer stellar mass, IR-based SFR and AGN luminosity simultaneously even for unobscured type 1 AGN. One potential drawback of IR-based SFR tracers for AGN feedback studies is that it traces the SFR on relatively long timescales of ~100 Myr and therefore the SFR can be significantly over or underestimated for a strongly declining or rising SFR within that timescale (Hayward et al. 2014).

Considering that the quasar-mode feedback is expected to be a fast process, the Hα line may be a more viable tracer for the feedback, considering that it probes the current SFR on <5 Myr timescales. Unfortunately, the Hα line can be strongly boosted by AGN ionization. In order to use Hα as a SFR tracer, optical emission lines diagnostic diagrams such as the Baldwin-Phillips-Terlevich diagrams (Baldwin et al. 1981) have been extensively used to distinguish between AGN and H II region excitation. A comprehensive classification scheme with such diagnostic diagrams has been developed Kewley et al. (2006). In particular with integral-field unit (IFU) spectroscopy, the usage of BPT diagrams has been extended to map the ionization conditions across galaxies to exclude regions from the SFR estimation dominated by AGN ionization using such BPT demarcation lines (e.g., Husemann et al. 2014; Nascimento et al. 2019). However, the superposition of different ionization conditions along

the line-of-sight is a common scenario. The observed AGN mixing sequence (MS) arises from such a superposition, and an analytic approach to separate the relative contribution was presented in Davies et al. (2014a,b, 2016, 2017).

In this paper, we infer and compare the SFR estimated from Hα and the IR for a sample of 41 galaxies as part of the Close AGN Reference Survey (CARS[1]). CARS aims to shed light on the relationship between the central AGN and its host galaxy by following a spatially resolved multiwavelength approach. As presented in Husemann et al. (2022), the 41 CARS targets are a subsample of 99 luminous unobscured AGN at $z < 0.06$ previously identified with the flux-limited Hamburg/ESO AGN survey (Wisotzki et al. 2000). The AGN targeted by CARS therefore correspond to the most luminous unobscured AGN in the nearby Universe allowing a detailed investigation of AGN – host galaxies interactions at relatively high spatial resolution.

In this work we use both panchromatic SEDs (to estimate stellar masses and FIR-based SFRs), and analyze the CARS IFU data to infer Hα based SFRs (adopting a new algorithm to separate the contribution to the Hα-line from other excitation mechanisms). In addition, we explore the use of different prescriptions to predict the expected SFR from the non-AGN galaxy population as control samples. This allows us to investigate links with AGN parameters depending on the actual SFR tracers and control sample properties being used as well as to distinguish between potentially declining and increasing star formation histories amongst the AGN host galaxies. Throughout the paper, we assume a flat cosmological model with $H_0 = 70\,\mathrm{km\,s^{-1}\,Mpc^{-1}}$, $\Omega_M = 0.3$, and $\Omega_\Lambda = 0.7$.

2. Observational data set

2.1. Archival broad-band photometry

We collect publicly available broad-band photometry from archival sources combined with dedicated observations for CARS targets to construct their panchromatic spectral energy distributions (SEDs). Where catalogs are not available or do not properly handle extended sources, we extract consistent aperture photometry from the public survey images. All photometric measurements are listed in Table 1 and their origin is described below (see Fig. 1 for photometric band compilation).

2.1.1. Catalog data

We directly took data from the *Herschel*/SPIRE point source catalog (250 μm, 350 μm, and 500 μm bands, Schulz et al. 2017), the AKARI/FIS bright source catalog (N60, N160, WIDE-L, and WIDE-S bands, Yamamura et al. 2009), and the 2MASS extended source catalog (J, H, and K_s bands, Jarrett et al. 2000) without further processing. The GALEX source catalog (FUV and NUV bands, Bianchi et al. 2017) were used only to compare the fluxes to our own aperture photometry measurements.

2.1.2. Aperture photometry

For the following data sets we performed customized aperture measurements on the survey images: *Herschel*/PACS 70, 100, and 160 μm images from the *Herschel* science archive[2], WISE atlas images (Cutri et al. 2011), 2MASS J, H and K_s images

from the interactive image service[3], VISTA/Paranal J, H, and K_s band images from the Cambridge astronomical survey unit[4], optical *grizy* photometric images[5] from the Pan-STARRS DR1 (Chambers et al. 2016) and *ugriz* images[6] from the SDSS-III DR12 (Alam et al. 2015), and GALEX and *Swift*/UVOT ultraviolet images from the Barbara A. Mikulski Archive for Space Telescopes[7].

The elliptical apertures are defined for each instrument to cover the entire galaxy in the sequence of the bands. The aperture fluxes are computed using the AstroPy Python package PHOTUTILS[8] (Bradley et al. 2020). Since the images of CARS targets are extended at these wavelengths the apertures are not affected by beam smearing and PSF matching as done for higher redshift targets is not a concern for our sample.

2.2. Galactic extinction and AGN broad-line correction

The observed photometry for external galaxies is attenuated by the dust in the Milky Way depending on the specific line-of-sight. We apply an extinction correction to the NIR, optical, and UV photometry of the SED using the Fitzpatrick (1999) Milky Way attenuation curve. The normalization of the attenuation curve is anchored to the measured V band extinction (A_V) along our line-of-sight toward the target is taken from Schlafly & Finkbeiner (2011) and retrieved from the NASA/IPAC Extragalactic Database (NED)[9]. All corresponding photometric data in Table 1 are provided after extinction correction.

The broad emission lines of unobscured AGN can significantly contribute to broad-band photometry. Because the SED model library used for the fitting assumes smooth power-law for the optical-UV accretion disk component we need to subtract the broad emission line contribution from the photometry. We used the available IFU spectroscopy of the CARS sample to measure Hβ and Hα fluxes, and subtract them from the optical bands (mainly g and r). The values presented in Table 1 are presented after correction for the BLR contribution.

2.3. Dedicated broad-band imaging

Given the lack of available data in some bands for some of the CARS targets, we obtained dedicated observations to fill the missing gaps in our photometry. Optical observations were mainly missing in the u band which Pan-STARRS does not cover and HE 0108−4743 and HE 2211−3903 are not covered by SDSS or Pan-STARRS, given their low declination. Therefore, we obtained deep wide-field optical imaging with the Dark Energy Camera (DECam, DePoy et al. 2008) mounted to the 4 m Blanco telescope of the Cerro Tololo Inter-American Observatory (CTIO) and with the Wide-Field Imager (WFI, Baade et al. 1999) mounted to the 2.2 m telescope of the La Silla observatory. Missing NIR imaging were obtained with the PAnoramic Near-Infrared Camera (PANIC, Cárdenas Vázquez et al. 2018) mounted to the 2.2 m telescope at the Calar Alto Observatory. Finally, deeper FIR observations were obtained for most of the CARS targets undetected with AKARI using the High-resolution

---

Table 1. Multiband aperture photometry measurements.

| Object | GALEX | | SDSS/DECAM/PanSTARRS1 | | | | | | WFI | | |
	FUV [mJy]	NUV [mJy]	u [mJy]	g [mJy]	r [mJy]	i [mJy]	z [mJy]	y [mJy]	U [mJy]	B [mJy]	V [mJy]
HE 0021−1810	0.17 ± 0.02	0.21 ± 0.02	. . .	1.4 ± 0.1	2.3 ± 0.2	3.2 ± 0.3	3.6 ± 0.4	4.8 ± 0.5	0.5 ± 0.1	. . .	. . .
HE 0021−1819	0.18 ± 0.02	0.25 ± 0.03	. . .	1.0 ± 0.1	1.6 ± 0.2	2.1 ± 0.2	2.3 ± 0.2	2.9 ± 0.3	0.3 ± 0.0	. . .	. . .
HE 0040−1105	0.09 ± 0.01	0.18 ± 0.02	0.62 ± 0.06	1.5 ± 0.1	2.4 ± 0.2	3.4 ± 0.3	4.0 ± 0.4	. . .	. . .	. . .	. . .
HE 0045−2145	. . .	. . .	. . .	. . .	. . .	. . .	. . .	. . .	. . .	. . .	. . .
HE 0108−4743	0.69 ± 0.07	1.29 ± 0.13	. . .	. . .	. . .	. . .	. . .	. . .	1.7 ± 0.2	4.9 ± 0.5	8.0 ± 0.8
HE 0114−0015	0.21 ± 0.02	0.34 ± 0.03	0.68 ± 0.07	1.8 ± 0.2	3.1 ± 0.3	4.3 ± 0.4	5.3 ± 0.5	. . .	. . .	. . .	. . .
HE 0119−0118	0.84 ± 0.02	1.26 ± 0.03	1.66 ± 0.17	3.5 ± 0.3	5.1 ± 0.5	6.9 ± 0.7	8.0 ± 0.8	. . .	. . .	. . .	. . .
HE 0150−0344	0.32 ± 0.03	0.44 ± 0.04	0.65 ± 0.07	1.3 ± 0.1	1.6 ± 0.2	2.1 ± 0.2	2.3 ± 0.2	. . .	. . .	. . .	. . .
HE 0203−0031	1.78 ± 0.18	1.95 ± 0.19	4.61 ± 0.46	9.1 ± 0.9	15.5 ± 1.5	21.6 ± 2.2	26.4 ± 2.6	. . .	. . .	. . .	. . .
HE 0212−0059	0.81 ± 0.08	1.26 ± 0.13	4.66 ± 0.47	17.2 ± 1.7	32.9 ± 3.3	46.3 ± 4.6	58.4 ± 5.8	. . .	. . .	. . .	. . .
HE 0224−2834	0.19 ± 0.02	0.35 ± 0.03	. . .	2.0 ± 0.2	3.0 ± 0.3	3.9 ± 0.4	4.3 ± 0.4	5.2 ± 0.5	0.7 ± 0.1	. . .	. . .
HE 0227−0913	3.23 ± 0.32	4.25 ± 0.43	5.74 ± 0.57	9.4 ± 0.9	14.5 ± 1.5	17.9 ± 1.8	22.1 ± 2.2	. . .	. . .	. . .	. . .
HE 0232−0900	4.46 ± 0.45	5.22 ± 0.52	7.48 ± 0.75	12.0 ± 1.2	16.9 ± 1.7	23.1 ± 2.3	27.4 ± 2.7	. . .	. . .	. . .	. . .
HE 0253−1641	0.14 ± 0.01	0.31 ± 0.03	1.16 ± 0.12	3.1 ± 0.3	5.1 ± 0.5	6.8 ± 0.7	8.3 ± 0.8	. . .	. . .	. . .	. . .
HE 0345+0056	2.79 ± 0.28	4.32 ± 0.43	6.36 ± 0.64	8.3 ± 0.8	9.7 ± 1.0	10.2 ± 1.0	11.5 ± 1.2	. . .	. . .	. . .	. . .
HE 0351+0240	0.86 ± 0.09	1.14 ± 0.11	. . .	2.0 ± 0.2	3.2 ± 0.3	3.8 ± 0.4	4.3 ± 0.4	5.2 ± 0.5	. . .	. . .	. . .
HE 0412−0803	0.30 ± 0.03	0.45 ± 0.05	. . .	4.8 ± 0.5	7.5 ± 0.7	8.2 ± 0.8	9.5 ± 1.0	11.5 ± 1.1	2.1 ± 0.2	. . .	. . .
HE 0429−0247	. . .	. . .	. . .	1.6 ± 0.2	2.4 ± 0.2	2.8 ± 0.3	3.1 ± 0.3	3.6 ± 0.4	. . .	. . .	. . .
HE 0433−1028	4.72 ± 0.47	4.88 ± 0.49	. . .	10.2 ± 1.0	15.1 ± 1.5	17.5 ± 1.7	20.3 ± 2.0	25.3 ± 2.5	5.3 ± 0.5	. . .	. . .
HE 0853−0126	0.32 ± 0.03	0.53 ± 0.05	1.07 ± 0.11	2.1 ± 0.2	3.2 ± 0.3	4.3 ± 0.4	5.1 ± 0.5	. . .	. . .	. . .	. . .
HE 0853+0102	0.15 ± 0.01	0.20 ± 0.02	0.43 ± 0.04	1.2 ± 0.1	1.9 ± 0.2	2.5 ± 0.3	3.1 ± 0.3	3.8 ± 0.4	. . .	. . .	. . .
HE 0934+0119	0.69 ± 0.07	0.84 ± 0.08	1.79 ± 0.18	2.5 ± 0.3	3.3 ± 0.3	4.0 ± 0.4	3.8 ± 0.4	4.6 ± 0.5	. . .	. . .	. . .
HE 0949−0122	0.45 ± 0.05	0.71 ± 0.07	2.14 ± 0.21	5.8 ± 0.6	10.7 ± 1.1	12.6 ± 1.3	16.7 ± 1.7	. . .	. . .	. . .	. . .
HE 1011−0403	2.39 ± 0.24	2.86 ± 0.29	2.39 ± 0.24	4.0 ± 0.4	5.3 ± 0.5	6.5 ± 0.6	7.0 ± 0.7	8.5 ± 0.9	. . .	. . .	. . .
HE 1017−0305	0.65 ± 0.06	0.84 ± 0.08	1.51 ± 0.15	3.1 ± 0.3	5.1 ± 0.5	7.1 ± 0.7	8.6 ± 0.9	. . .	. . .	. . .	. . .
HE 1029−1831	0.61 ± 0.06	1.13 ± 0.11	1.52 ± 0.15	4.0 ± 0.4	6.1 ± 0.6	7.1 ± 0.7	8.2 ± 0.8	10.1 ± 1.0	. . .	. . .	. . .
HE 1107−0813	1.26 ± 0.13	2.30 ± 0.23	. . .	5.7 ± 0.6	7.2 ± 0.7	7.9 ± 0.8	8.2 ± 0.8	9.6 ± 1.0	. . .	. . .	. . .
HE 1108−2813	. . .	. . .	3.80 ± 0.38	10.9 ± 1.1	16.2 ± 1.6	19.6 ± 2.0	22.8 ± 2.3	26.6 ± 2.7	. . .	. . .	. . .
HE 1126−0407	1.54 ± 0.15	2.77 ± 0.28	4.16 ± 0.42	6.7 ± 0.7	7.7 ± 0.8	10.8 ± 1.1	10.5 ± 1.1	12.0 ± 1.2	. . .	. . .	. . .
HE 1237−0504	4.94 ± 0.49	9.47 ± 0.95	. . .	72.1 ± 7.2	136.8 ± 13.7	189.6 ± 19.0	217.0 ± 21.7	261.6 ± 26.2	. . .	. . .	. . .
HE 1248−1356	0.49 ± 0.05	0.97 ± 0.10	2.91 ± 0.29	12.2 ± 1.2	21.5 ± 2.2	28.7 ± 2.9	34.7 ± 3.5	41.2 ± 4.1	. . .	. . .	. . .
HE 1310−1051	1.19 ± 0.12	1.32 ± 0.13	1.42 ± 0.14	3.2 ± 0.3	4.3 ± 0.4	4.7 ± 0.5	5.2 ± 0.5	5.6 ± 0.6	. . .	. . .	. . .
HE 1330−1013	. . .	. . .	1.83 ± 0.18	6.5 ± 0.7	11.2 ± 1.1	15.1 ± 1.5	18.2 ± 1.8	22.0 ± 2.2	. . .	. . .	. . .
HE 1338−1423	1.86 ± 0.19	2.18 ± 0.22	3.26 ± 0.33	6.7 ± 0.7	10.9 ± 1.1	13.2 ± 1.3	15.6 ± 1.6	18.7 ± 1.9	. . .	. . .	. . .
HE 1353−1917	0.21 ± 0.02	0.50 ± 0.05	0.86 ± 0.09	3.0 ± 0.3	6.3 ± 0.6	7.7 ± 0.8	9.7 ± 1.0	11.4 ± 1.1	. . .	. . .	. . .
HE 1417−0909	0.54 ± 0.05	0.51 ± 0.05	0.73 ± 0.07	1.1 ± 0.1	1.9 ± 0.2	2.4 ± 0.2	2.6 ± 0.3	3.2 ± 0.3	. . .	. . .	. . .
HE 2128−0221	0.14 ± 0.01	0.24 ± 0.02	0.49 ± 0.05	0.8 ± 0.1	1.2 ± 0.1	1.6 ± 0.2	1.9 ± 0.2	. . .	. . .	. . .	. . .
HE 2211−3903	0.69 ± 0.07	1.03 ± 0.10	. . .	. . .	. . .	. . .	. . .	. . .	2.6 ± 0.3	4.5 ± 0.5	. . .
HE 2222−0026	0.13 ± 0.01	0.19 ± 0.02	0.35 ± 0.04	0.8 ± 0.1	1.3 ± 0.1	1.9 ± 0.2	2.4 ± 0.2	. . .	. . .	. . .	. . .
HE 2233+0124	0.07 ± 0.01	0.10 ± 0.01	1.07 ± 0.11	1.9 ± 0.2	3.3 ± 0.3	5.2 ± 0.5	6.8 ± 0.7	. . .	. . .	. . .	. . .
HE 2302−0857	1.85 ± 0.18	2.04 ± 0.20	3.25 ± 0.33	6.6 ± 0.7	11.2 ± 1.1	16.5 ± 1.7	20.2 ± 2.0	. . .	. . .	. . .	. . .

Airborne Wideband Camera Plus (HAWC+, Harper et al. 2018) aboard the Stratospheric Observatory for Infrared Astronomy (SOFIA) and the Submillimetre Common-User Bolometer Array 2 (SCUBA-2, Holland et al. 2013) camera mounted to the *James Clark Maxwell* Telescope (JCMT). The data characteristics and data reduction of all those new observations are described in more detail below.

2.3.1. DECam optical observations

DECam imaging in the *u* band was obtained for 14 CARS targets during the nights of 1−3 April 2017 as part of the program 2017A-0914 (P.I.: Grant Tremblay). DECam covers almost 3 sq. deg using a mosaic of 62 2 k × 4 k CCDs with a pixel size of 0.27″. The total exposure times for each target ranged from 1200 s to 4800 s. The data were automatically reduced by the DECam community pipeline (Valdes et al. 2014) and retrieved from the NOAO archive. Absolute flux calibration for individual images was achieved by comparing detected stars in the field with the photometrically-calibrated SkyMapper DR1 (Wolf et al. 2018) catalog magnitudes.

2.3.2. WFI optical observations

WFI imaging in the *UBV* bands was obtained for HE 0108−4743 and HE 2211−3903 to provide optical photometry given the missing Pan-STARRS and SDSS coverage. The observations were taken during a larger observing run from 18 to 28 October under program 0100.A-9003 (P.I.: Bernd Husemann). WFI covers a 34′ × 33′ FoV using a mosaic of 8 2 k × 4 k CCDs. At the time of observations 2 of the CCDs were broken so that a two-pointing offset scheme plus dithering was used to cover the same field. A total exposure time of 3600 s was obtained for the *U* band.

The images were fully reduced and combined with the latest version of the THELI pipeline[10] (version 3) (Schirmer 2013). The absolute magnitude zero-point for each combined image was obtained by comparing stellar counts with catalog values from the SkyMapper DR1 and APASS DR1 (Henden et al. 2009) for the *UBV* bands.

---

[10] https://github.com/schirmermischa/THELI

Table 1. continued.

Object	2MASS/PANIC/VISTA			WISE				Herschel/PACS		
	J [mJy]	H [mJy]	K_s [mJy]	$W1$ [mJy]	$W2$ [mJy]	$W3$ [mJy]	$W4$ [mJy]	70 μm [mJy]	100 μm [mJy]	160 μm [mJy]
HE 0021−1810	5.6 ± 0.6	7.4 ± 0.7	. . .	4.6 ± 0.5	3.8 ± 0.4	5 ± 0	8 ± 1	. . .	. . .	. . .
HE 0021−1819	3.4 ± 0.3	. . .	3.6 ± 0.4	2.3 ± 0.2	2.3 ± 0.2	8 ± 1	21 ± 2	. . .	. . .	. . .
HE 0040−1105	5.4 ± 0.5	6.9 ± 0.7	. . .	5.4 ± 0.5	6.4 ± 0.6	15 ± 2	34 ± 3	. . .	. . .	. . .
HE 0045−2145	15.9 ± 1.6	. . .	16.2 ± 1.6	13.0 ± 1.3	10.1 ± 1.0	99 ± 10	516 ± 52	. . .	. . .	. . .
HE 0108−4743	18.0 ± 1.8	20.9 ± 2.1	18.9 ± 1.9	16.8 ± 1.7	15.5 ± 1.5	63 ± 6	121 ± 12	. . .	. . .	. . .
HE 0114−0015	6.7 ± 0.7	10.7 ± 1.1	. . .	6.5 ± 0.7	6.2 ± 0.6	17 ± 2	38 ± 4	. . .	. . .	. . .
HE 0119−0118	11.8 ± 1.2	13.1 ± 1.3	. . .	14.9 ± 1.5	19.2 ± 1.9	60 ± 6	239 ± 24	. . .	. . .	. . .
HE 0150−0344	2.6 ± 0.3	3.0 ± 0.3	2.8 ± 0.3	2.3 ± 0.2	2.0 ± 0.2	16 ± 2	54 ± 5	. . .	. . .	. . .
HE 0203−0031	31.8 ± 0.8	38.5 ± 1.1	36.3 ± 1.6	31.0 ± 3.1	32.1 ± 3.2	42 ± 4	65 ± 6	77 ± 12	. . .	. . .
HE 0212−0059	73.0 ± 7.3	81.0 ± 8.1	71.6 ± 7.2	43.3 ± 4.3	31.1 ± 3.1	92 ± 9	242 ± 24	413 ± 21	. . .	1975 ± 99
HE 0224−2834	5.5 ± 0.5	7.9 ± 0.8	7.5 ± 0.7	10.2 ± 1.0	14.4 ± 1.4	35 ± 3	89 ± 9	. . .	. . .	. . .
HE 0227−0913	27.0 ± 2.7	. . .	40.4 ± 4.0	43.4 ± 4.3	50.1 ± 5.0	96 ± 10	159 ± 16	. . .	. . .	. . .
HE 0232−0900	35.4 ± 3.5	45.1 ± 4.5	. . .	44.7 ± 4.5	54.8 ± 5.5	156 ± 16	409 ± 41	1197 ± 26	. . .	1450 ± 57
HE 0253−1641	11.3 ± 1.1	14.5 ± 1.4	. . .	12.4 ± 1.2	15.8 ± 1.6	58 ± 6	155 ± 16	. . .	. . .	. . .
HE 0345+0056	. . .	21.1 ± 2.1	. . .	58.9 ± 5.9	80.8 ± 8.1	181 ± 18	315 ± 32	. . .	. . .	. . .
HE 0351+0240	. . .	8.0 ± 0.8	. . .	9.8 ± 1.0	13.8 ± 1.4	32 ± 3	85 ± 9	186 ± 17	. . .	. . .
HE 0412−0803	. . .	16.5 ± 1.7	. . .	43.1 ± 4.3	66.0 ± 6.6	175 ± 17	386 ± 39	587 ± 19	. . .	423 ± 51
HE 0429−0247	4.5 ± 0.4	5.8 ± 0.6	. . .	8.1 ± 0.8	9.9 ± 1.0	15 ± 1	27 ± 3	. . .	. . .	. . .
HE 0433−1028	. . .	38.6 ± 3.9	. . .	50.8 ± 5.1	77.6 ± 7.8	239 ± 24	598 ± 60	2474 ± 49	. . .	2334 ± 47
HE 0853−0126	4.9 ± 0.5	. . .	6.3 ± 0.6	4.9 ± 0.5	4.2 ± 0.4	11 ± 1	19 ± 2	. . .	. . .	. . .
HE 0853+0102	5.1 ± 0.5	6.8 ± 0.7	7.3 ± 0.7	5.8 ± 0.6	6.0 ± 0.6	9 ± 1	14 ± 1	. . .	. . .	. . .
HE 0934+0119	6.0 ± 0.6	6.9 ± 0.7	8.7 ± 0.9	5.9 ± 0.6	7.7 ± 0.8	25 ± 2	59 ± 6	219 ± 1	248 ± 8	257 ± 9
HE 0949−0122	28.4 ± 0.7	53.3 ± 1.4	96.1 ± 2.3	175.1 ± 17.5	256.3 ± 25.6	490 ± 49	921 ± 92	. . .	. . .	. . .
HE 1011−0403	. . .	11.0 ± 1.1	. . .	10.6 ± 1.1	12.7 ± 1.3	34 ± 3	73 ± 7	165 ± 2	209 ± 9	234 ± 10
HE 1017−0305	14.2 ± 1.4	. . .	10.8 ± 1.1	14.0 ± 1.4	16.1 ± 1.6	36 ± 4	71 ± 7	. . .	. . .	. . .
HE 1029−1831	11.4 ± 1.1	. . .	14.9 ± 1.5	15.2 ± 1.5	16.5 ± 1.6	86 ± 9	306 ± 31	. . .	. . .	. . .
HE 1107−0813	. . .	20.9 ± 2.1	26.6 ± 2.7	21.5 ± 2.1	24.7 ± 2.5	30 ± 3	46 ± 5	. . .	. . .	. . .
HE 1108−2813	26.4 ± 2.6	. . .	33.7 ± 3.4	39.7 ± 4.0	41.2 ± 4.1	127 ± 13	471 ± 47	. . .	. . .	. . .
HE 1126−0407	11.5 ± 1.1	18.9 ± 1.9	28.5 ± 2.8	34.7 ± 3.5	46.1 ± 4.6	98 ± 10	262 ± 26	454 ± 9	. . .	354 ± 7
HE 1237−0504	415.0 ± 10.5	494.2 ± 13.9	426.5 ± 14.6	241.1 ± 24.1	181.5 ± 18.2	362 ± 36	829 ± 83	. . .	. . .	. . .
HE 1248−1356	43.7 ± 4.4	48.0 ± 4.8	46.2 ± 4.6	28.6 ± 2.9	21.5 ± 2.1	68 ± 7	138 ± 14	. . .	. . .	. . .
HE 1310−1051	6.6 ± 0.7	7.8 ± 0.8	8.8 ± 0.9	10.8 ± 1.1	17.2 ± 1.7	53 ± 5	113 ± 11	95 ± 2	115 ± 8	116 ± 11
HE 1330−1013	26.8 ± 2.7	33.7 ± 3.4	29.4 ± 2.9	16.2 ± 1.6	12.1 ± 1.2	23 ± 2	50 ± 5	. . .	. . .	. . .
HE 1338−1423	21.5 ± 2.1	26.7 ± 2.7	28.0 ± 2.8	27.0 ± 2.7	33.3 ± 3.3	78 ± 8	149 ± 15	141 ± 18	. . .	. . .
HE 1353−1917	15.3 ± 1.5	20.5 ± 2.1	20.9 ± 2.1	14.1 ± 1.4	13.2 ± 1.3	34 ± 3	73 ± 7	246 ± 5	. . .	768 ± 15
HE 1417−0909	3.4 ± 0.3	3.9 ± 0.4	4.2 ± 0.4	4.3 ± 0.4	5.5 ± 0.6	13 ± 1	28 ± 3	. . .	. . .	. . .
HE 2128−0221	2.5 ± 0.3	3.2 ± 0.3	3.4 ± 0.3	3.2 ± 0.3	3.9 ± 0.4	10 ± 1	22 ± 2	. . .	. . .	. . .
HE 2211−3903	. . .	15.3 ± 1.5	37.0 ± 3.7	58.2 ± 5.8	83.1 ± 8.3	188 ± 19	371 ± 37	. . .	. . .	. . .
HE 2222−0026	3.1 ± 0.3	4.6 ± 0.5	. . .	5.0 ± 0.5	6.4 ± 0.6	13 ± 1	21 ± 2	. . .	. . .	. . .
HE 2233+0124	8.2 ± 0.8	10.9 ± 1.1	. . .	11.4 ± 1.1	11.3 ± 1.1	13 ± 1	14 ± 1	. . .	. . .	. . .
HE 2302−0857	43.0 ± 4.3	53.0 ± 5.3	. . .	75.1 ± 7.5	87.0 ± 8.7	114 ± 11	239 ± 24	441 ± 9	. . .	641 ± 13

2.3.3. PANIC NIR observations

Additional NIR imaging was also obtained with the Panoramic Near-Infrared Camera (PANIC, Cárdenas Vázquez et al. 2018) mounted to the 2.2 m telescope at the Calar Alto observatory. Although PANIC consists of 4 Hawaii-2RG detectors only 2 were operational at the time of observations of which only one had nominal performance. 20 CARS targets were observed as part of programmes F17-2.2-014 and H17-2.2-008 (P.I.: Bernd Husemann). For the first program only the best performing chip was used covering a FoV of 15′ × 15′. For the second program a mosaic strategy was used to cover the nominal 30′ × 30′ with the two operational detectors. The sampling of PANIC is 0.′′45 per pixel. For the analysis in this paper we only use a small part of the images covering the AGN host galaxies so that the full FoV is not relevant.

Total exposure times ranged from 1−2 h for the J, H, and K_s bands, but not all NIR bands could be obtained for all the targets. A spiral dither pattern was used along all observations for background subtraction, excluding satellite tracks and image cosmetics. The PANIC exposures were reduced and combined with the dedicated PANIC pipeline[11]. The astrometric registration and absolute photometry was further optimized with the PhotometryPipline (PP, Mommert 2017) software package using 2MASS as photometric reference.

2.3.4. SCUBA-2 FIR observations

SCUBA-2 is a 10 000 pixel bolometer camera simultaneously operating at 450 μm and 850 μm and covering an area of 41 arcmin² on the sky (Holland et al. 2013). Effective beam sizes are 10′′ and 15′′ at 450 μm and 850 μm, respectively.

Given the angular size of our AGN hosts on the sky, we observe using the 'constant velocity (CV) Daisy' mapping mode which provides uniform sensitivity in the central 3′ of the observation. The 'CV Daisy' is a circular scanning pattern designed so that the target is always within the field-of-view of the array throughout the integration while moving at a constant 155′′ s⁻¹. The observation provides usable coverage out to ∼6.0′ in radius,

---

[11] https://github.com/ppmim/PAPI

Table 1. continued.

Object	AKARI				SOFIA		Herschel/SPIRE			JWST/SCUBA2	
	N60 [mJy]	WIDE-S [mJy]	WIDE-L [mJy]	N160 [mJy]	D band [mJy]	E band [mJy]	250 μm [mJy]	350 μm [mJy]	500 μm [mJy]	450 μm [mJy]	850 μm [mJy]
HE 0021−1810	...	...	...	...	<296	...	...	...	...	...	...
HE 0021−1819	...	...	...	...	228 ± 23	...	...	...	...	...	...
HE 0040−1105	...	...	...	...	<873	...	...	...	...	<76	<5
HE 0045−2145	3130 ± 82	3904 ± 103	3518 ± 391	4134 ± 954	...	...	...	...	...	<239	12 ± 6
HE 0108−4743	<450	1006 ± 71	3778 ± 328	2245 ± 979	...	...	...	...	...	...	...
HE 0114−0015	...	...	...	...	...	...	214 ± 17	86 ± 16	...	...	...
HE 0119−0118	...	1411 ± 98	1879 ± 605	<1917	...	...	573 ± 23	198 ± 20	66 ± 22	...	...
HE 0150−0344	<330	720 ± 65	<1445	<1261	...	...	293 ± 21	108 ± 23	...	...	...
HE 0203−0031	...	...	...	...	...	...	82 ± 16	72 ± 16	...	...	...
HE 0212−0059	<701	747 ± 69	2648 ± 929	...	...	...	612 ± 37	349 ± 31	186 ± 21	...	...
HE 0224−2834	...	...	...	...	...	...	...	...	...	...	...
HE 0227−0913	<989	455 ± 85	<1072	...	...	407 ± 41	...	...	...	<270	<12
HE 0232−0900	...	1291 ± 16	2204 ± 389	...	...	...	699 ± 21	356 ± 24	144 ± 28	...	...
HE 0253−1641	...	...	...	...	661 ± 66	...	...	...	...	...	...
HE 0345+0056	...	...	...	...	...	...	...	...	...	...	...
HE 0351+0240	...	...	...	...	...	...	...	...	...	<129	<9
HE 0412−0803	...	...	...	...	...	...	...	...	...	<105	<8
HE 0429−0247	...	...	...	...	<445	...	...	...	...	...	...
HE 0433−1028	...	2572 ± 103	<4505	...	...	...	1102 ± 20	496 ± 26	204 ± 18	...	...
HE 0853−0126	...	...	...	...	...	...	...	...	...	...	...
HE 0853+0102	...	...	...	...	...	...	100 ± 11	...	...	...	...
HE 0934+0119	...	...	...	...	...	...	...	...	...	<229	<10
HE 0949−0122	...	1375 ± 164	...	...	...	...	...	...	...	...	...
HE 1011−0403	...	...	...	...	...	...	126 ± 12	51 ± 12	...	...	...
HE 1017−0305	...	...	...	...	...	...	...	...	...	<323	<10
HE 1029−1831	2134 ± 407	2596 ± 93	3535 ± 984	...	...	...	...	...	...	<331	15 ± 7
HE 1107−0813	...	...	...	...	...	...	...	...	...	...	...
HE 1108−2813	3203 ± 109	3330 ± 174	...	...	...	...	...	...	...	191 ± 120	14 ± 6
HE 1126−0407	...	484 ± 30	...	<1163	...	...	198 ± 14	80 ± 15	...	...	...
HE 1237−0504	2659 ± 345	2926 ± 174	5120 ± 423	4676 ± 808	...	...	...	...	...	...	...
HE 1248−1356	...	972 ± 100	2409 ± 1520	...	...	...	...	...	...	<172	10 ± 6
HE 1310−1051	...	...	...	...	...	...	61 ± 11	...	...	...	...
HE 1330−1013	...	...	...	...	...	...	...	...	...	<137	6 ± 4
HE 1338−1423	...	...	...	...	...	...	127 ± 18	83 ± 16	...	...	...
HE 1353−1917	...	<585	...	...	...	...	444 ± 52	216 ± 32	85 ± 16	...	...
HE 1417−0909	...	...	...	...	...	...	...	...	...	...	...
HE 2128−0221	...	...	...	...	<457	...	...	...	...	...	...
HE 2211−3903	...	657 ± 70	...	...	...	...	...	...	...	...	...
HE 2222−0026	...	...	...	...	...	...	...	...	...	...	...
HE 2233+0124	...	...	...	...	<527	...	...	...	...	...	...
HE 2302−0857	...	647 ± 119	...	...	...	...	282 ± 14	...	...	...	...

but beyond a radius of 1.5′ the map sensitivity decreases rapidly.

The observations were performed in service mode between February and December 2019 during grade 3 weather conditions ($0.08 < \tau_{225} < 0.12$) as part of project M19AP019 (P.I.: Timothy Davis). On-source exposure times ranged from 1 h to 7.5 h. The resulting maps were reduced using the Dynamic Iterative Map Maker (DIMM) within the sub-mm user reduction facility (SMURF, Chapin et al. 2013). For a full overview of the procedure see Chapin et al. (2013).

The data were reduced using the blank field reduction in order to detect point sources within the map. The maps were then calibrated using the standard flux calibration factors of $FCF_{450} = 491$ Jy beam^{-1} pW^{-1} and $FCF_{850} = 537$ Jy beam^{-1} pW^{-1} (Dempsey et al. 2013). To improve the point source detection, a matched filter was applied to the maps. This matched filtering caused a ~10% loss in flux (determined by inserting artificial sources into the map and comparing the flux before and after), so an additional 10% was applied to the FCFs to account for this.

2.3.5. SOFIA HAWC+ FIR observations

The HAWC+ FIR camera (Harper et al. 2018) aboard SOFIA was used to obtain FIR photometry for CARS targets that could not be detected with all-sky AKARI FIR survey and that were not targeted with *Herschel*. Observations were taken for 8 out of 11 proposed targets as part of a SOFIA survey program (Plan ID: 07_193, P.I.: Bernd Husemann) with exposure times ranging from 15 min to 60 min. HE 0227−0913 was observed in the E band (214 μm) while all other targets were observed in the D band (154 μm). The FWHM of the HAWC+ beam is 18″2 and 13″5 for the E and D band, respectively. All data were reduced by the HAWC+ SOFIA team using a dedicated instrument pipeline. The pipeline was run specifically with the faint object flag to account for the faint signal in our targets.

2.4. Integral-field spectroscopy observations

IFU observations for the CARS sample were mainly obtained with the MUSE instrument at the Very Large Telescope (VLT; Bacon et al. 2010) for 37 targets under programs 094.B-0345(A),
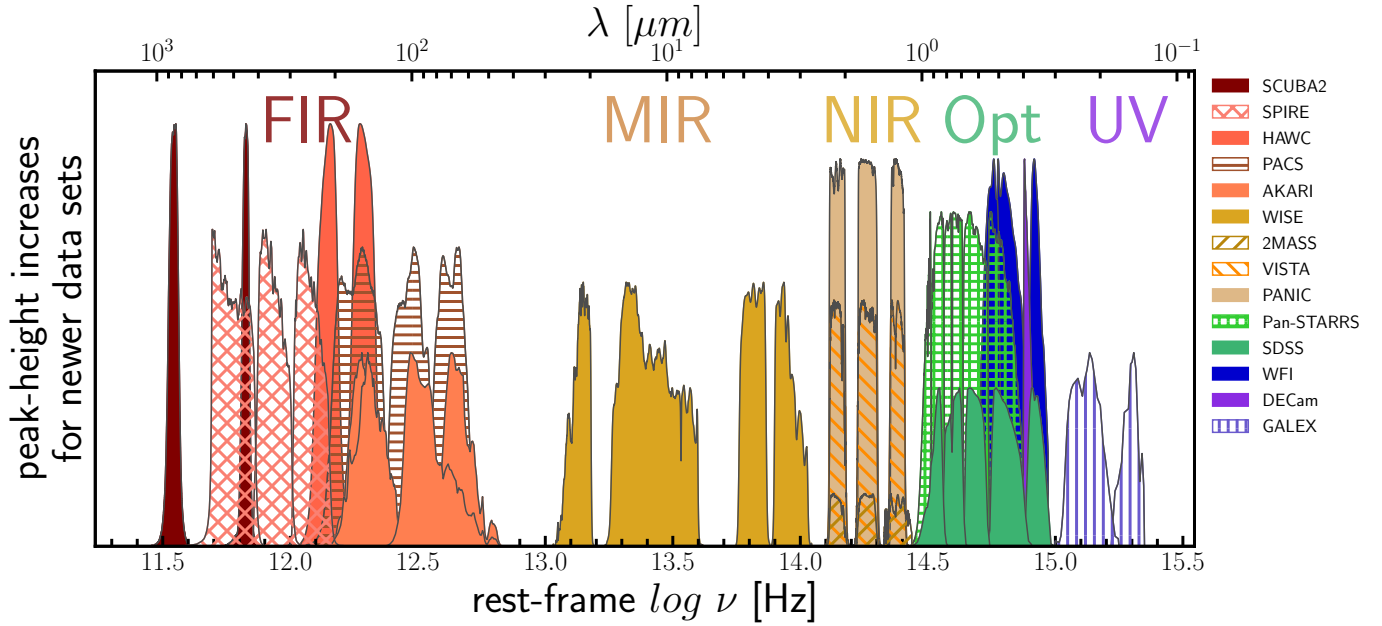
Fig. 1. Photometric broad bands from a number of surveys and instruments used for the SED modeling. The *y*-axis is normalized roughly by the year of observational campaign to visually compare bands with similar coverage. When more than one option was available for certain bands, the preference was given to the band sets, which are temporally closer to each other (especially in near infrared and optical ranges) to minimize the impact of AGN variability.

095.B-0015(A), 099.B-0242(A), and 099.B-0249(B), with the VIMOS instrument at the VLT (Le Févre et al. 2003) for 2 targets under program 083.B-0801(A), and with the PMAS instrument at the 3.5 m Calar Alto telescope (Roth et al. 2005) for 2 targets under program H18-3.5-010. MUSE covers a $1' \times 1'$ FoV at a sampling of $0\farcs2$, VIMOS covers a $27'' \times 27''$ FoV at a sampling of $0\farcs67$ and PMAS covers a $16'' \times 16''$ FoV with a sampling of $1''$. All details of the IFU observations and their data reduction are presented in Husemann et al. (2022) to which the interested reader is referred.

For the present paper, we are working with emission line maps that were created after the AGN point-like emission was removed from the reconstructed IFU datacube as described in Husemann et al. (2022). Emission-line fluxes are extracted by fitting Gaussian profiles after modeling and subtracting the stellar continuum with PyParadise (see Walcher et al. 2015; Weaver et al. 2018; Husemann et al. 2022, for details) from the AGN-subtracted data. All the details of this process and its application to the CARS IFU data are presented in Husemann et al. (2022). For the analysis presented in this paper we use the 2D emission line maps of [O III] λ5007, Hβ, [N II] λ6583, Hα, [S II] $\lambda\lambda$6716,6731 and their associated errors. All those data are also accessible from the CARS data release 1[12].

3. Analysis

3.1. modeling the panchromatic spectral energy distribution

In order to infer primary physical parameters such as the stellar mass $M_\star$ or the SFR, we need to model the panchromatic SED constructed for all the sources. We decided to perform the SED fitting with the publicly available AGNfitter package (Calistro Rivera et al. 2016). AGNfitter models the observed photometry as a super-position of various template libraries for the stellar continuum, the AGN accretion disk emission, AGN-heated dust emission from the torus and the cold dust emission excited by star formation.

The stellar library is taken from Bruzual & Charlot (2003) and parametrized by a stellar age of the galaxy and an exponential decay time of the starburst τ which can be further modified by reddening and normalized in absolute flux. The accretion disk emission is represented by an empirical composite spectrum generated from 259 type-1 AGN from the Sloan Digital Sky Survey (SDSS, York et al. 2000), which can be reddened using the Small Magellanic Cloud reddening law of Prevot et al. (1984). This leaves the flux normalization and the reddening as the only two free parameters for this component. The hot dust component of the AGN is reconstructed from the empirical SED library collected by Silva et al. (2004) based on photometric observations of AGN that were modeled with the radiative transfer code GRASIL Silva et al. (1998) to obtain the full NIR SEDs. The library is divided in a range of absorbing neutral hydrogen column densities N_H through the torus along our line-of-sight as the main free parameter in addition to the normalization. Semi-empirical starburst template spectra from Chary & Elbaz (2001) and Dale & Helou (2002) are used to model the cold dust component from star formation which are denoted by a luminosity parameter and can be normalized.

AGNfitter uses the emcee package (Foreman-Mackey et al. 2013) for an affine-invariant Markov-chain Monte Carlo (MCMC) ensemble sampling to explore the 10-dimensional parameter space associated with the underlying template library of spectra. The advantage of AGNfitter is that it natively accepts upper limits in the photometry, allows to set priors on parameters and additional constraints can be incorporated easily to break degeneracies. Particularly, one big issue in the SED modeling of luminous type 1 AGN is that the accretion disk model is competing with the stellar population model in the UV–optical rest-frame wavelength regime. This leads to a degeneracy between the accretion disk and stellar continuum model when

---

[12] http://cars.aip.de
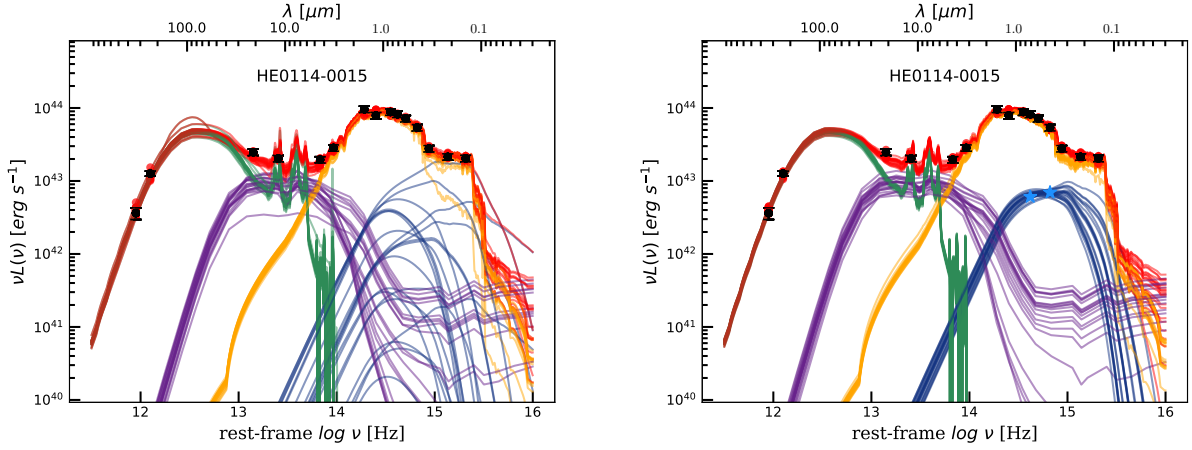
Fig. 2. SED for HE 0114−0015 and the best-fit model determined by `AGNfitter` (Calistro Rivera et al. 2016). 20 MCMC realizations of the SED model are shown for the broadband photometric data (black points with error bars) where the red points are the corresponding predictions from the model. The red lines represent the total model, which consists of four components: the cold and warm dust in star-forming regions (green lines), the torus of AGN-heated dust (purple lines), the stellar continuum (yellow lines), and the AGN accretion disk (blue lines). On the *right panel* is an additional constraint to the accretion disk model (e.g. *g* and *i* AGN photometry is included).

fitting the observed integrated broad-band photometry as shown in Fig. 2 (left panel).

This degeneracy could be solved by linking the UV radiation field with the corresponding re-emission in the IR as an additional constraint implemented for example in the `CIGALE` or `MAGPHYS` SED fitting codes. However, this method requires an assumption of the UV escape fractions and dust content of the galaxies, which can be very different for starburst galaxies and AGN-dominated galaxies. Due to the low redshift of the CARS sample, it is possible to spatially separate the AGN and host galaxy light using 2D image synthesis modeling even in ground-based images. This allows us to obtain direct measurements for the AGN brightness in the optical bands. The AGN magnitudes in the *g* and *i* bands are obtained by modeling the ground-based images as a super-position of two Sersic profiles and a point source for the AGN with the `galfit` package (Peng et al. 2002, 2010) as described in Husemann et al. (2022). Hence, we adjusted the likelihood function within the `AGNfitter` code to consider these additional photometric data as constraints solely for the AGN accretion disk component model. The effectiveness of this approach is shown in Fig. 2 in comparison to the modeling without those additional AGN constraints.

With the additional photometric constraints we reduced the uncertainties of the various physical quantities that are directly computed by `AGNfitter` from the posterior parameter distribution. For our work we are most interested in the stellar mass $M_\star$ that are based on the stellar population model and its associated luminosity normalization. In addition we report the integrated luminosity of the torus model (L_{tor}), and the luminosities of the cold dust component integrated between entire IR 8–1000 μm ($L_{8-1000\,μm}$) wavelength range and a restricted range of 42.5–122.5 μm ($L_{42.5-122.5\,μm}$) for literature comparisons. `AGNfitter` estimates a SFR from the integrated IR luminosity using the calibration established by Murphy et al. (2011):

$$\left(\frac{\text{SFR}_{\text{IR}}}{[M_\odot\,\text{yr}^{-1}]}\right) = 3.88 \times 10^{-44} \left(\frac{L_{8-1000\,μm}}{[\text{erg s}^{-1}]}\right). \tag{1}$$

In cases where the cold dust SED is not well constrained due to upper limits in the FIR photometry, we determine 5σ upper limits from the posterior distribution function of the integrated luminosities and SFR. We list all the inferred parameters from SED

fitting as described above in Table 2 and all the corresponding SED models with `AGNfitter` are shown in Fig. A.1.

3.2. Measuring Hα-based star formation rates

The IFU observations for the CARS sample as presented in Husemann et al. (2022) are well suited to measure the current star formation rate of the host galaxies in comparison to the FIR-based SFR. Various calibrations have been determined to convert the extinction-corrected Hα luminosity into a SFR from which we use the calibration of (Calzetti et al. 2007)

$$\left(\frac{\text{SFR}_{\text{H}\alpha}}{[M_\odot\,\text{yr}^{-1}]}\right) = 5.3 \times 10^{-42} \left(\frac{L_{\text{H}\alpha}}{[\text{erg s}^{-1}]}\right) \tag{2}$$

in this work to estimate the integrated SFR based on the integrated Hα. However, not all of the Hα emission is associated with star-forming H II regions in AGN host galaxies. A detailed spatially resolved emission line diagnostic analysis is therefore essential for AGN host galaxies to separate the contribution from AGN photoionization and star-forming H II regions to the excitation of Hα.

In order to provide reliable Hα-based SFR estimates, we use a combination of line maps from pixel-by-pixel and binned IFU cubes after subtracting the AGN point-source emission as described in Husemann et al. (2022) in more detail. While the pixel-by-pixel maps provide high-spatial resolution information for bright emission line regions, the binned maps provide higher signal-to-noise ratio (S/N) information on the more extended ionized gas. We only consider the diagnostic lines Hα, Hβ, [N II] and [O III] as detected above a 3σ level. For the maps we also include the weaker spaxels where only Hα S/N is required to be more than 3.

Here, we consider several ways to correct the Hα flux by the AGN contribution as described in more detail in the following subsections. All those methods leverage the potential of the IFU data to perform flexible spatially resolved emission-line diagnostics that open possibilities for de-contamination compared to traditional narrow-band imaging or long-slit spectroscopy.

Table 2. AGN host galaxy properties inferred from SED modeling.

Object	z [a]	$\log\left(\frac{M_\star}{[M_\odot]}\right)$ [b]	$\log\left(\frac{L_{\rm tor}}{[{\rm erg\,s^{-1}}]}\right)$ [c]	$\log\left(\frac{L_{42.5-122.5\,\mu{\rm m}}}{[{\rm erg\,s^{-1}}]}\right)$ [d]	$\log\left(\frac{L_{8-1000\,\mu{\rm m}}}{[{\rm erg\,s^{-1}}]}\right)$ [e]	$\mathrm{SFR_{IR}}$ [f]	$\log\left(\frac{L_{\rm CO}}{[{\rm K\,km\,s^{-1}\,pc^2}]}\right)$ [g]
HE 0021−1810	0.054	$10.64^{+0.04}_{-0.05}$	$43.02^{+0.07}_{-0.19}$	<43.67	<43.98	<3.7	<6.8
HE 0021−1819	0.053	$10.50^{+0.04}_{-0.05}$	$42.82^{+0.16}_{-0.59}$	$43.76^{+0.05}_{-0.04}$	$44.04^{+0.05}_{-0.04}$	$4.2^{+0.6}_{-0.3}$	7.6 ± 2.1
HE 0040−1105	0.042	$10.16^{+0.13}_{-0.10}$	$43.50^{+0.05}_{-0.04}$	<43.82	<44.03	<4.1	7.7 ± 1.7
HE 0045−2145	0.021	$9.36^{+0.03}_{-0.02}$	...	$44.18^{+0.01}_{-0.01}$	$44.45^{+0.01}_{-0.01}$	$10.9^{+0.2}_{-0.2}$	8.1 ± 0.4
HE 0108−4743	0.024	$9.77^{+0.18}_{-0.10}$	$43.12^{+0.07}_{-0.08}$	$43.67^{+0.02}_{-0.02}$	$44.04^{+0.02}_{-0.02}$	$4.3^{+0.2}_{-0.2}$	7.6 ± 0.6
HE 0114−0015	0.046	$10.47^{+0.13}_{-0.19}$	$43.26^{+0.10}_{-0.09}$	$43.74^{+0.03}_{-0.03}$	$44.02^{+0.03}_{-0.03}$	$4.0^{+0.3}_{-0.3}$	7.8 ± 2.9
HE 0119−0118	0.055	$10.91^{+0.02}_{-0.06}$	$43.76^{+0.10}_{-0.24}$	$44.65^{+0.01}_{-0.02}$	$44.89^{+0.01}_{-0.02}$	$30.4^{+1.0}_{-1.1}$	8.4 ± 0.8
HE 0150−0344	0.048	$9.57^{+0.12}_{-0.09}$	...	$44.10^{+0.02}_{-0.02}$	$44.36^{+0.02}_{-0.02}$	$9.0^{+0.4}_{-0.4}$	7.8 ± 3.4
HE 0203−0031	0.043	$10.88^{+0.02}_{-0.02}$	$43.90^{+0.04}_{-0.07}$	$43.00^{+0.08}_{-0.09}$	$43.34^{+0.06}_{-0.09}$	$0.8^{+0.1}_{-0.2}$	<7.0
HE 0212−0059	0.026	$10.59^{+0.01}_{-0.01}$	...	$43.54^{+0.01}_{-0.02}$	$43.87^{+0.01}_{-0.01}$	$2.9^{+0.1}_{-0.1}$	7.9 ± 0.6
HE 0224−2834	0.060	$10.13^{+0.19}_{-0.17}$	$44.27^{+0.04}_{-0.03}$	<44.06	<44.38	<9.3	7.9 ± 3.2
HE 0227−0913	0.016	$9.92^{+0.17}_{-0.12}$	$43.44^{+0.05}_{-0.05}$	$42.85^{+0.11}_{-0.10}$	$43.16^{+0.10}_{-0.08}$	$0.6^{+0.1}_{-0.1}$	7.2 ± 1.9
HE 0232−0900	0.043	$10.88^{+0.23}_{-0.12}$	$44.45^{+0.06}_{-0.04}$	$44.31^{+0.01}_{-0.01}$	$44.59^{+0.01}_{-0.01}$	$14.9^{+0.2}_{-0.2}$	8.6 ± 1.0
HE 0253−1641	0.032	$10.28^{+0.11}_{-0.24}$	$42.76^{+0.54}_{-1.39}$	$44.17^{+0.04}_{-0.05}$	$44.41^{+0.04}_{-0.05}$	$10.0^{+0.9}_{-1.2}$	8.0 ± 1.1
HE 0345+0056	0.031	$8.85^{+0.62}_{-0.26}$	$44.42^{+0.03}_{-0.03}$	<43.84	<44.13	<5.2	<6.7
HE 0351+0240	0.035	$9.85^{+0.34}_{-0.70}$	$43.75^{+0.04}_{-0.04}$	$43.28^{+0.04}_{-0.05}$	$43.56^{+0.05}_{-0.05}$	$1.4^{+0.2}_{-0.1}$	<6.9
HE 0412−0803	0.038	$10.08^{+0.10}_{-0.12}$	$44.57^{+0.02}_{-0.02}$	$43.78^{+0.02}_{-0.02}$	$44.04^{+0.02}_{-0.04}$	$4.2^{+0.2}_{-0.3}$	<6.8
HE 0429−0247	0.042	$9.18^{+0.51}_{-0.10}$	$43.55^{+0.03}_{-0.05}$	<44.10	<44.43	<10.5	<7.3
HE 0433−1028	0.036	$10.80^{+0.08}_{-0.09}$	$44.55^{+0.03}_{-0.03}$	$44.43^{+0.00}_{-0.00}$	$44.70^{+0.00}_{-0.00}$	$19.4^{+0.2}_{-0.2}$	8.6 ± 0.6
HE 0853−0126	0.060	$10.32^{+0.06}_{-0.08}$	$43.54^{+0.07}_{-0.24}$	<44.05	<44.42	<10.1	8.2 ± 2.4
HE 0853+0102	0.053	$10.54^{+0.04}_{-0.10}$	$43.31^{+0.08}_{-0.05}$	$43.16^{+0.09}_{-0.30}$	$43.51^{+0.08}_{-0.20}$	$1.3^{+0.3}_{-0.5}$	<7.2
HE 0934+0119	0.051	$10.13^{+0.25}_{-0.31}$	$43.75^{+0.05}_{-0.05}$	$43.71^{+0.00}_{-0.01}$	$43.98^{+0.00}_{-0.01}$	$3.7^{+0.0}_{-0.0}$	<7.0
HE 0949−0122	0.020	$10.02^{+0.09}_{-0.31}$	$44.54^{+0.02}_{-0.02}$	$43.45^{+0.07}_{-0.10}$	$43.74^{+0.10}_{-0.09}$	$2.1^{+0.5}_{-0.4}$	7.2 ± 2.3
HE 1011−0403	0.059	$10.74^{+0.07}_{-0.17}$	$44.16^{+0.04}_{-0.03}$	$43.69^{+0.01}_{-0.01}$	$43.98^{+0.01}_{-0.01}$	$3.7^{+0.1}_{-0.1}$	8.2 ± 1.8
HE 1017−0305	0.049	$10.93^{+0.10}_{-0.15}$	$44.06^{+0.05}_{-0.05}$	<44.10	<44.45	<11.0	8.0 ± 1.6
HE 1029−1831	0.041	$10.49^{+0.06}_{-0.18}$	$43.89^{+0.05}_{-0.08}$	$44.57^{+0.01}_{-0.02}$	$44.84^{+0.01}_{-0.02}$	$27.1^{+0.8}_{-1.3}$	8.4 ± 1.0
HE 1107−0813	0.059	$11.17^{+0.20}_{-0.38}$	$43.78^{+0.17}_{-1.34}$	<44.46	<44.87	<28.6	8.0 ± 2.5
HE 1108−2813	0.024	$10.29^{+0.11}_{-0.05}$	$43.74^{+0.07}_{-0.09}$	$44.24^{+0.01}_{-0.01}$	$44.50^{+0.02}_{-0.01}$	$12.4^{+0.4}_{-0.4}$	8.2 ± 0.7
HE 1126−0407	0.060	$10.59^{+0.37}_{-0.46}$	$44.73^{+0.03}_{-0.04}$	$44.15^{+0.01}_{-0.01}$	$44.42^{+0.01}_{-0.01}$	$10.2^{+0.2}_{-0.1}$	8.2 ± 2.0
HE 1237−0504	0.008	$10.92^{+0.01}_{-0.01}$	$43.12^{+0.06}_{-0.06}$	$43.26^{+0.03}_{-0.02}$	$43.58^{+0.02}_{-0.03}$	$1.5^{+0.1}_{-0.1}$	7.2 ± 1.5
HE 1248−1356	0.015	$10.31^{+0.01}_{-0.01}$	$42.65^{+0.10}_{-0.16}$	$43.22^{+0.06}_{-0.07}$	$43.49^{+0.05}_{-0.06}$	$1.2^{+0.1}_{-0.2}$	7.3 ± 1.1
HE 1310−1051	0.034	$10.35^{+0.06}_{-0.18}$	$43.90^{+0.02}_{-0.02}$	$42.87^{+0.02}_{-0.02}$	$43.17^{+0.02}_{-0.02}$	$0.6^{+0.0}_{-0.0}$	<6.8
HE 1330−1013	0.022	$10.69^{+0.03}_{-0.13}$	$42.93^{+0.10}_{-0.49}$	<43.69	<43.89	<3.0	7.5 ± 1.8
HE 1338−1423	0.041	$11.02^{+0.06}_{-0.20}$	$44.24^{+0.03}_{-0.05}$	$43.18^{+0.06}_{-0.08}$	$43.52^{+0.05}_{-0.07}$	$1.3^{+0.2}_{-0.2}$	<6.9
HE 1353−1917	0.035	$10.99^{+0.03}_{-0.06}$	$43.37^{+0.07}_{-0.07}$	$43.50^{+0.01}_{-0.01}$	$43.86^{+0.01}_{-0.01}$	$2.8^{+0.1}_{-0.1}$	8.1 ± 1.4
HE 1417−0909	0.044	$10.23^{+0.10}_{-0.17}$	$43.54^{+0.04}_{-0.05}$	<43.39	<43.67	<1.8	<6.7
HE 2128−0221	0.053	$9.93^{+0.21}_{-0.67}$	$43.58^{+0.04}_{-0.05}$	<43.75	<44.02	<4.0	<6.9
HE 2211−3903	0.040	$9.83^{+0.22}_{-0.21}$	$44.64^{+0.02}_{-0.03}$	$43.84^{+0.06}_{-0.05}$	$44.16^{+0.07}_{-0.08}$	$5.6^{+0.9}_{-1.0}$	8.0 ± 1.2
HE 2222−0026	0.058	$10.20^{+0.09}_{-0.15}$	$43.81^{+0.02}_{-0.04}$	<44.11	<44.46	<11.2	7.4 ± 3.9
HE 2233+0124	0.057	$10.71^{+0.10}_{-0.03}$	$41.55^{+0.71}_{-0.58}$	$43.84^{+0.03}_{-0.05}$	$44.22^{+0.03}_{-0.05}$	$6.4^{+0.4}_{-0.6}$	8.0 ± 1.8
HE 2302−0857	0.047	$11.20^{+0.09}_{-0.13}$	$44.31^{+0.06}_{-0.06}$	$43.96^{+0.01}_{-0.01}$	$44.24^{+0.01}_{-0.01}$	$6.7^{+0.1}_{-0.1}$	8.2 ± 1.4

Notes. [a]Redshift directly measured from the CARS IFU data as reported in Husemann et al. (2022). [b]Stellar masses and 1σ uncertainties from stellar template fitting reported by `AGNFitter`. [c]Integrated luminosity of the torus template reported by `AGNFitter`. [d]Luminosity of the matched star-forming IR template reported by `AGNFitter` integrated over the $42.5-122.5\,\mu{\rm m}$ wavelength range. [e]Same as (d) but integrated over the full $8-1000\,\mu{\rm m}$ wavelength range. [f]Estimated SFR based on $L_{8-1000\,\mu{\rm m}}$ using calibration of Murphy et al. (2011), see Eq. (1). [g]CO(1−0) line luminosity based on the flux measurements from Bertram et al. (2007) and listed in Husemann et al. (2022).
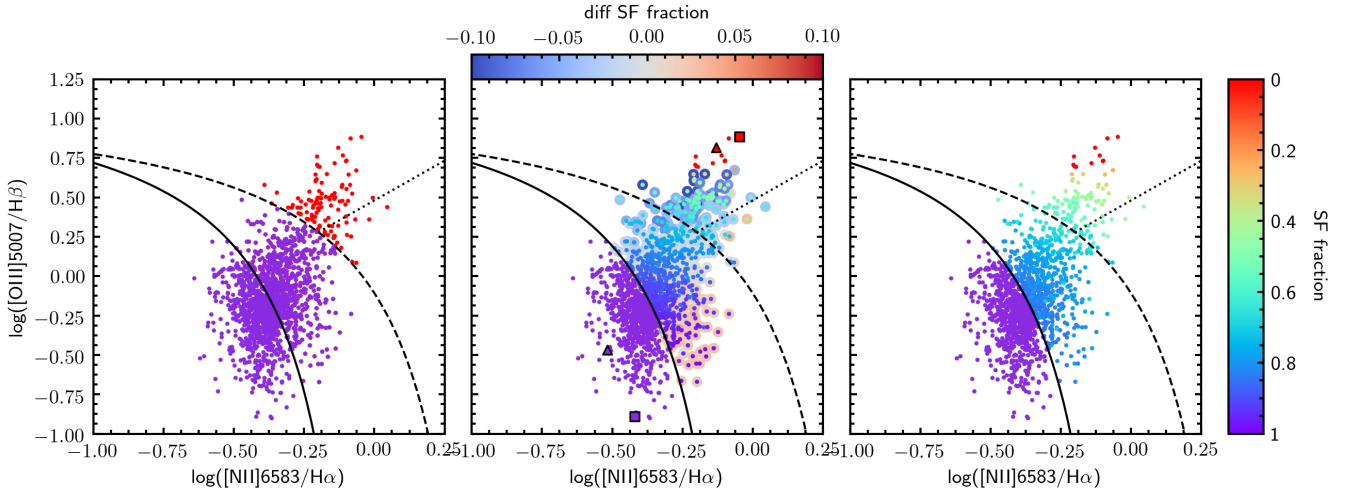
Fig. 3. BPT diagram of HE 0853+0102 as an example for a mixing sequence between H II regions and AGN photoionization across the host galaxy. We highlight three ways of determining the SF fraction from the BPT diagram. *Left panel*: a simple demarcation line approach where everything above the Kewley et al. (2001) line is classified as pure AGN and below as pure star formation. *Middle panel*: simple linear combination with a χ^2 fit using a fixed line vector as a reference point for the characteristic AGN and H II line ratios. The colored halos around the points represent the difference between the calculated SF fraction adopting two different different reference pairs (triangle and square symbols) to highlight the systematic uncertainties introduced by a certain choice. *Right panel*: MCMC fitting results of the star formation fraction adopting a large cloud of potential reference points for the AGN (red points) and H II region (magenta points) which are explored during the MCMC sampling.

3.2.1. Demarcation lines

The simplest approach to correct for the AGN affected Hα emission is to ignore those spaxels displaying AGN ionization and integrate only the Hα flux from regions clearly associated with H II regions. Specific BPT demarcation lines are often used as hard boundaries to distinguish between different ISM ionization processes in galaxies even though physically (due to line-of-sight blending and other physical processes) those demarcations cannot be hard boundaries.

The theoretical "maximum starburst" demarcation line proposed by Kewley et al. (2001) divides the region where ionization could still be explained by pure star-formation from the region where AGN ionization is required to contribute to the emission. Similarly, the empirical 'pure star-forming' BPT demarcation line proposed by Kauffmann et al. (2003) defines a part in the BPT assumed to be powered purely by H II regions whereas other mechanisms can play a role in the remaining part. The gap in between the stricter "pure star-forming" and the "maximum starburst" demarcation lines is often referred to as the mixed or composite BPT region.

The AGN contamination to Hα across the BPT and, in particular, through the composite region can be tackled in different ways. Nascimento et al. (2019) considers the pure star-forming region and the composite region to be entirely associated with star formation assuming that the AGN contribution in the composite region compensates for the 'hidden' star formation. Wylezalek et al. (2018) assigns a fixed fraction of 80% of AGN ionization contribution to Hα in the BPT region above the "maximum starburst" demarcation line and only a 20% contribution to the composite region. We use the former approach (illustrated in Fig. 3, left panel) to be able to consistently compare our results (Table 3) with previous works and the more sophisticated methods as described below.

3.2.2. BPT mixing sequence

In contrast to the fixed contribution assumed before, there is likely a smooth transition of ionization contributions across

galaxies. AGN host galaxies therefore often show a mixing sequence which appears as an elongated structure in the BPT diagram. This mixing sequence (MS) usually exhibits a prominent dependency on the distance from the AGN. As proposed by Davies et al. (2014a,b, 2016, 2017), one can pick basis vectors of emission line ratios to characterize pure AGN and star-forming ionization and treat the composite data points of the MS as a linear combination of the basis vectors:

$$
\begin{pmatrix} [\text{O\,III}]/\text{H}\beta \\ [\text{N\,II}]/\text{H}\alpha \\ [\text{S\,II}]/\text{H}\alpha \end{pmatrix}_{\text{MS}} = f_{\text{AGN}} \times \begin{pmatrix} [\text{O\,III}]/\text{H}\beta \\ [\text{N\,II}]/\text{H}\alpha \\ [\text{S\,II}]/\text{H}\alpha \end{pmatrix}_{\text{AGN}} + f_{\text{SF}} \times \begin{pmatrix} [\text{O\,III}]/\text{H}\beta \\ [\text{N\,II}]/\text{H}\alpha \\ [\text{S\,II}]/\text{H}\alpha \end{pmatrix}_{\text{SF}} .
$$
(3)

Here, the parameters f_{AGN} and f_{SF} represent the non-negative linear coefficient for the AGN and star-forming ionization fractions, correspondingly. An important additional basic constraint of $f_{\text{AGN}} + f_{\text{SF}} = 1$ ensures that flux is preserved. In principle more excitation mechanisms could be added to this equation, but this will lead to degeneracies in the basis vector as they are not fully orthogonal.

The emission line columns are normalized to either Hα or Hβ, which minimizes the impact of internal extinction within the host on the results. Here, we include the [S II]/Hα line ratio from the other classical BPT diagram and more line ratios could in principle be considered if S/N are high enough to be informative.

The idea behind the method is to pick emission-line basis vectors at the extreme ends of the mixing sequence, which should best reflect the assumption of two completely independent excitation mechanisms. The process of picking such emission-line ratio basis vectors allows considerable freedom and uncertainty. For example, the selected pair of basis vectors may not fully capture the different ISM conditions across the galaxies such as metallicity or ionization parameter. In the Fig. 3, middle panel, the example of two different bases pairs – triangle and square symbols – leads to a 10% difference in the resulting SF fraction.

Table 3. Hα-based SFRs and metallicity estimated from the IFU emission lines.

| Object | Demarcation line approach | | BPT rainbow method | | | | |
	$f_{H\alpha}$ [a] $[10^{-16}\,\mathrm{erg\,s^{-1}\,cm^{-2}}]$	$\mathrm{SFR}_{H\alpha}$ [b] $[M_\odot\,\mathrm{yr}^{-1}]$	Class [c]	$f_{H\alpha}$ [a] $[10^{-16}\,\mathrm{erg\,s^{-1}\,cm^{-2}}]$	$\mathrm{SFR}_{H\alpha}$ [b] $[M_\odot\,\mathrm{yr}^{-1}]$	$12 + \log(\mathrm{O/H})$ [d] $[r_{\mathrm{eff}}^{-1}]$	$\alpha_{\mathrm{O/H}}$ [e] $[r_{\mathrm{eff}}^{-1}]$
HE 0021−1819	359 ± 36	1.3 ± 0.1	MS	342 ± 34	1.2 ± 0.1	8.89 ± 0.02	−0.031 ± 0.010
HE 0040−1105	16 ± 2	0.03 ± 0.00	AGN	<41	<0.1	8.85 ± 0.02	0.040 ± 0.016
HE 0045−2145	5672 ± 567	3.1 ± 0.3	LMS	4687 ± 477	2.5 ± 0.3	9.16 ± 0.02	−0.018 ± 0.003
HE 0108−4743	8594 ± 859	5.9 ± 0.6	MS	8251 ± 825	5.7 ± 0.6	9.05 ± 0.01	−0.055 ± 0.009
HE 0114−0015	978 ± 98	2.5 ± 0.3	LMS	901 ± 90	2.3 ± 0.2	9.06 ± 0.02	−0.007 ± 0.011
HE 0119−0118	1107 ± 111	4.1 ± 0.4	MS	1006 ± 101	3.8 ± 0.4	8.99 ± 0.01	0.026 ± 0.020
HE 0150−0344	3961 ± 396	10.5 ± 1.0	. . .	. . .	. . .	8.88 ± 0.02	−0.029 ± 0.005
HE 0203−0031	71 ± 7	0.16 ± 0.02	AGN+SF	<202	<0.5	9.08 ± 0.02	−0.006 ± 0.003
HE 0212−0059	4163 ± 416	3.5 ± 0.4	MS	3978 ± 398	3.4 ± 0.3	8.99 ± 0.00	−0.050 ± 0.013
HE 0224−2834	368 ± 37	1.7 ± 0.2	MS+AGN	397 ± 40	1.8 ± 0.2	8.88 ± 0.01	−0.006 ± 0.007
HE 0227−0913	2970 ± 297	1.0 ± 0.1	MS	2933 ± 293	0.9 ± 0.1	8.96 ± 0.01	−0.017 ± 0.007
HE 0232−0900	8226 ± 823	19.0 ± 1.9	MS	8197 ± 820	19.0 ± 1.9	9.00 ± 0.01	−0.017 ± 0.004
HE 0253−1641	197 ± 20	0.24 ± 0.02	MS	232 ± 23	0.28 ± 0.03	8.97 ± 0.02	−0.025 ± 0.023
HE 0345+0056	3474 ± 348	4.1 ± 0.4	SF	3477 ± 348	4.1 ± 0.4	8.81 ± 0.09	0.066 ± 0.073
HE 0351+0240	143 ± 14	0.23 ± 0.02	AGN	<240	<0.4	8.80 ± 0.03	−0.010 ± 0.013
HE 0412−0803	93 ± 9	0.17 ± 0.02	AGN	<192	<0.3	8.85 ± 0.02	0.009 ± 0.007
HE 0429−0247	262 ± 26	0.6 ± 0.1	AGN	<338	<0.7	8.80 ± 0.02	0.016 ± 0.015
HE 0433−1028	5997 ± 600	9.3 ± 0.9	MS+SF	6700 ± 671	10.4 ± 1.0	8.97 ± 0.01	−0.049 ± 0.009
HE 0853+0102	407 ± 41	1.4 ± 0.1	MS	381 ± 38	1.3 ± 0.1	8.89 ± 0.02	−0.005 ± 0.021
HE 0853−0126	142 ± 14	0.6 ± 0.1	SF	130 ± 13	0.6 ± 0.1	8.60 ± 0.16	0.130 ± 0.154
HE 0934+0119	650 ± 65	2.1 ± 0.2	MS+SF	599 ± 60	1.9 ± 0.2	8.92 ± 0.02	−0.098 ± 0.011
HE 0949−0122	26 ± 3	0.01 ± 0.00	AGN	<214	<nan	8.90 ± 0.04	0.049 ± 0.039
HE 1011−0403	328 ± 33	1.4 ± 0.1	LMS	294 ± 29	1.3 ± 0.1	9.03 ± 0.01	−0.022 ± 0.014
HE 1017−0305	353 ± 35	1.1 ± 0.1	LMS	340 ± 34	1.1 ± 0.1	9.00 ± 0.02	−0.007 ± 0.021
HE 1029−1831	4689 ± 469	9.4 ± 0.9	SF	3732 ± 377	7.5 ± 0.8	9.12 ± 0.01	−0.099 ± 0.006
HE 1107−0813	121 ± 12	0.5 ± 0.1	MS+AGN	115 ± 12	0.49 ± 0.05	9.08 ± 0.02	−0.003 ± 0.006
HE 1108−2813	6094 ± 609	4.2 ± 0.4	MS+SF	5840 ± 587	4.1 ± 0.4	9.01 ± 0.01	−0.110 ± 0.008
HE 1126−0407	195 ± 20	1.0 ± 0.1	MS	217 ± 22	1.1 ± 0.1	9.08 ± 0.03	−0.048 ± 0.022
HE 1237−0504	1501 ± 150	0.14 ± 0.01	LMS	3249 ± 425	0.31 ± 0.04	9.10 ± 0.00	−0.144 ± 0.025
HE 1248−1356	2766 ± 277	0.7 ± 0.1	MS	3034 ± 303	0.8 ± 0.1	9.05 ± 0.01	−0.128 ± 0.012
HE 1310−1051	1294 ± 129	1.9 ± 0.2	SF	1258 ± 127	1.8 ± 0.2	8.84 ± 0.07	0.010 ± 0.049
HE 1330−1013	763 ± 76	0.45 ± 0.05	MS	716 ± 72	0.42 ± 0.04	9.13 ± 0.04	−0.146 ± 0.053
HE 1338−1423	742 ± 74	1.6 ± 0.2	AGN	1319 ± 135	2.9 ± 0.3	9.04 ± 0.06	−0.019 ± 0.075
HE 1353−1917	609 ± 61	0.9 ± 0.1	MS+A+S	594 ± 59	0.9 ± 0.1	8.96 ± 0.02	−0.119 ± 0.013
HE 1417−0909	6 ± 1	0.01 ± 0.00	AGN	<23	<0.1	8.73 ± 0.08	0.106 ± 0.066
HE 2128−0221	154 ± 15	0.5 ± 0.1	MS	140 ± 14	0.49 ± 0.05	8.93 ± 0.04	−0.047 ± 0.020
HE 2211−3903	2419 ± 242	4.7 ± 0.5	MS+SF	2534 ± 253	4.9 ± 0.5	9.08 ± 0.01	−0.145 ± 0.010
HE 2222−0026	43 ± 4	0.19 ± 0.02	SF	34 ± 3	0.15 ± 0.02	8.80 ± 0.05	0.088 ± 0.050
HE 2233+0124	355 ± 36	1.4 ± 0.1	MS+AGN	339 ± 34	1.4 ± 0.1	9.05 ± 0.02	−0.057 ± 0.018
HE 2302−0857	1339 ± 134	3.7 ± 0.4	MS	1618 ± 162	4.4 ± 0.4	8.92 ± 0.01	−0.074 ± 0.013

Notes. [a] Integrated extinction-corrected Hα flux decontaminated by AGN contribution either using a demarcation line cut or the rainbow method presented here. Given the high S/N of the data the error is dominated by the systematics in the absolute photometric zero-point which is assumed to be 10%. [b] Hα-based SFR determined from the asscoicated Hα luminosity following the calibration of Calzetti et al. (2007), see Eq. (2). [c] Classification of the BPT in a (LINER) mixing sequence (L)MS, AGN cloud, SF cloud and any combination of the four. [d] Central oxygen abundance on the Tremonti et al. (2004) metallicity scale determined through the N2S2 index following Eq. (5). A linear fit to the radial distribution is used to determine the central abdunance as the spatial coverages varies through the sample. [e] Slope of the linear metallicity gradient normalized to the effective radius of the respective galaxy as reported in Husemann et al. (2022).

For more meaningful results, the uncertainties caused by the choice of the basis vector need to be estimated and included into the final SFR uncertainty. With Monte Carlo Markov chain (MCMC) algorithms it is possible to use the Bayesian approach and also take into account the uncertainty of the underlying model. So, our solution to the basis-picking problem is to define a large number of basis ratio sets and let the MCMC sampling to choose basis vectors for a certain spaxel and, more importantly, take the uncertainty of this choice into account. We use the MCMC python package EMCEE to develop a python package called rainbow[13] designed to handle the mixing sequence

---

[13] Publicly available open-source at https://gitlab.com/SPIrina/rainbow

fitting. For each given spaxel it tries various combinations of basis vectors and determines the posterior probability distribution of the parameters through maximizing the likelihood function:

$$\ln p(\boldsymbol{y}|\boldsymbol{x}_{\mathrm{AGN}}, \boldsymbol{x}_{\mathrm{SF}}, f_{\mathrm{SF}}, \boldsymbol{\sigma}_y, \mathscr{F}) = -\frac{1}{2}\sum\left[\frac{(\boldsymbol{y} - \boldsymbol{y}_{\mathrm{model}})^2}{\sigma^2} + \ln(2\pi\sigma^2)\right],$$

$$\sigma^2 = \sigma_y^2 + \boldsymbol{y}_{\mathrm{model}}^2 \times \mathscr{F}^2; \tag{4}$$

where $\boldsymbol{y}$ represents the vector of emission line ratios of the fitted spaxel, $\boldsymbol{\sigma}_y$ is the corresponding error vector, $\boldsymbol{x}_{\mathrm{AGN}}$ and $\boldsymbol{x}_{\mathrm{SF}}$ represent basis vectors, and the model is $\boldsymbol{y}_{\mathrm{model}}(\boldsymbol{x}_{\mathrm{AGN}}, \boldsymbol{x}_{\mathrm{SF}}, f_{\mathrm{SF}}) = (1 - f_{\mathrm{SF}})\boldsymbol{x}_{\mathrm{AGN}} + f_{\mathrm{SF}}\boldsymbol{x}_{\mathrm{SF}}$ such as the vector Eq. (3). The likelihood function here is a Gaussian where the variance is underestimated by the fractional amount parameter $\mathscr{F}$, that represents an uncertainty of the model. The star-forming ionization fraction f_{SF} and its uncertainty then is inferred from the probability distribution. An example of the MCMC fitting result from `rainbow` is shown in the right panel of Fig. 3.

Our criteria of picking SF emission-line ratio basis vectors from the mixing sequence are: first, SF bases should be below the "pure star-forming line" (Kauffmann et al. 2003); second, the signal-to-noise ratio of all the involved lines should be 3σ or more ($>3\sigma$ threshold is used to reduce the number of the basis vectors which speeds-up the fitting process); third, a certain radius may be specified to bound the basis vectors closer to the center and represent a narrower range of metallicities and ionization parameters. The criteria of picking AGN (or shock/evolved star, as described in Sect. 3.2.3) photoionization basis vector from the mixing sequence are the following: first, [O III]/Hβ is above a certain threshold, this threshold cannot be same for all galaxies, as it depends on the strength of the AGN, and, therefore, is set to a value between $0.5-0.8$ ($0.25-0.5$ for LINERs) depending on a galaxy, so that only the top spaxels are selected; second, a certain distance from the AGN may be specified to separate the AGN basis in the central spatial region and extended AGN cloud. The adopted selection is shown on a galaxy-by-galaxy case in Fig. B.1 for the entire sample.

3.2.3. BPT morphology

The idea of treating the mixing sequence as a signature of physical mixing of H II regions and AGN ionized regions suggests that different populations of spaxels on a BPT diagram can be differentiated based on their properties. We name this approach BPT morphology, as the idea is to distinguish different shapes on the diagram (see Fig. 4):

(1) The star-forming cloud is an extended structure located under the "maximum starburst line" of Kewley et al. (2001) on a BPT diagram. This emission arises from across the star forming body of a galaxy and, therefore, contains emission from regions with different metallicities, densities, and ionization parameters. The variance of these ISM parameters results in the extensive shape that covers large area in the BPT diagram. Although it spreads out to the composite area between the "pure star-forming" and the "maximum starburst" demarcation lines on the BPT diagram, we assume that there is no need to clean this group of spaxels from the AGN contamination. See HE 0150−0344 (Fig. 4 middle row, left) as an example of a galaxy without AGN but with the spaxels spreading to the composite BPT area.

(2) The AGN-ionized cloud is a structure which spans the upper region of a BPT diagram and spreads to the left side toward lower [N II]/Hα line ratios. This corresponds to the extended narrow-line region or AGN-illuminated gas. Spatially, this

region can reach from the AGN across the entire galaxy and even outside of the galaxy's main body. This group of spaxels does not contribute to the galaxy's SFR, although we can infer the upper limits considering hidden star formation as highlighted below.

(3) The mixing sequence is already described in the section above; it is an elongated structure on a BPT diagram which tends to be located in the central region of a galaxy. However, not all mixing sequences end in the AGN ionized area of the BPT diagram, where some are extending from the H II regions area to the LINER area likely due to different excitation mechanisms for the LINER emission. Nevertheless, the LINER mixing sequence can be treated in the same way as the AGN mixing sequence, following the same assumption of the two main excitation sources – star formation and LINER excitation. The model (Eq. (3)) will then have f_{LINER} instead of f_{AGN} with the same flux preservation constrain $f_{\mathrm{LINER}} + f_{\mathrm{SF}} = 1$.

An AGN host galaxy can have one of the described populations or even a combination of those (see the galaxy-by-galaxy cases in Appendix B). We separate star-forming clouds and AGN-ionized clouds with a simple yet efficient method: manually introducing fixed spatial radii for each individual galaxy (listed on the Table B.1) and separating the regions with the circles as on the bottom examples of Figs. 4 and B.1. After separating different populations we assume that the SF cloud and AGN-ionized cloud have 100% and 0% contribution to the star-formation rate, correspondingly. The mixing sequence is modeled, out to a certain radius, with RAINBOW as described in the previous section to compute SF fractions along the sequence.

However, we attempt to correct all populations for the AGN contribution (similarly as with the mixing sequence). Given that some small contribution to the Hα emission from star formation may be hidden in galaxies which display only an AGN cloud morphology, we estimate an upper limit for the SF contribution adopting AGN bases or SF bases from the other galaxies with a prominent mixing sequence and apply our `rainbow` analysis.

3.2.4. Gas-phase metallicity

Another important characteristic of the ionized gas is the metallicity. The gas-phase metallicity tracks the immediate enrichment history of the ISM due to the evolution of stars and their metal yields across the galaxy. Undisturbed disk galaxies typically have negative metallicity gradients (Sánchez et al. 2014) and their central metallicity correlates with the stellar mass of a galaxy (Tremonti et al. 2004; Kewley & Ellison 2008). As stellar evolution is a long-term process, outflows and inflows of gas on short timescales can significantly affect the observed metallicity distribution and therefore can be used as a key diagnostic to understand the origin and motions of gas on galactic scales. For example a flattening and dilution of gas-phase metallicity have been observed during galaxy mergers and interactions (e.g., Ellison et al. 2008; Kewley et al. 2010; Thorp et al. 2019), and in barred galaxies (Martin & Roy 1994; Sánchez et al. 2014) where low-metallicity gas from the outskirts is efficiently transported toward the center. On the other hand, gas outflows can enrich the circum-galactic medium with metals from the galaxy center which has been observationally confirmed from absorption line studies (e.g., Bordoloi et al. 2011; Tumlinson et al. 2011; Bouché et al. 2012; Nielsen et al. 2015; Schroetter et al. 2019).

Measuring gas-phase metallicities across AGN host galaxies is more complicated because all strong-line metallicity
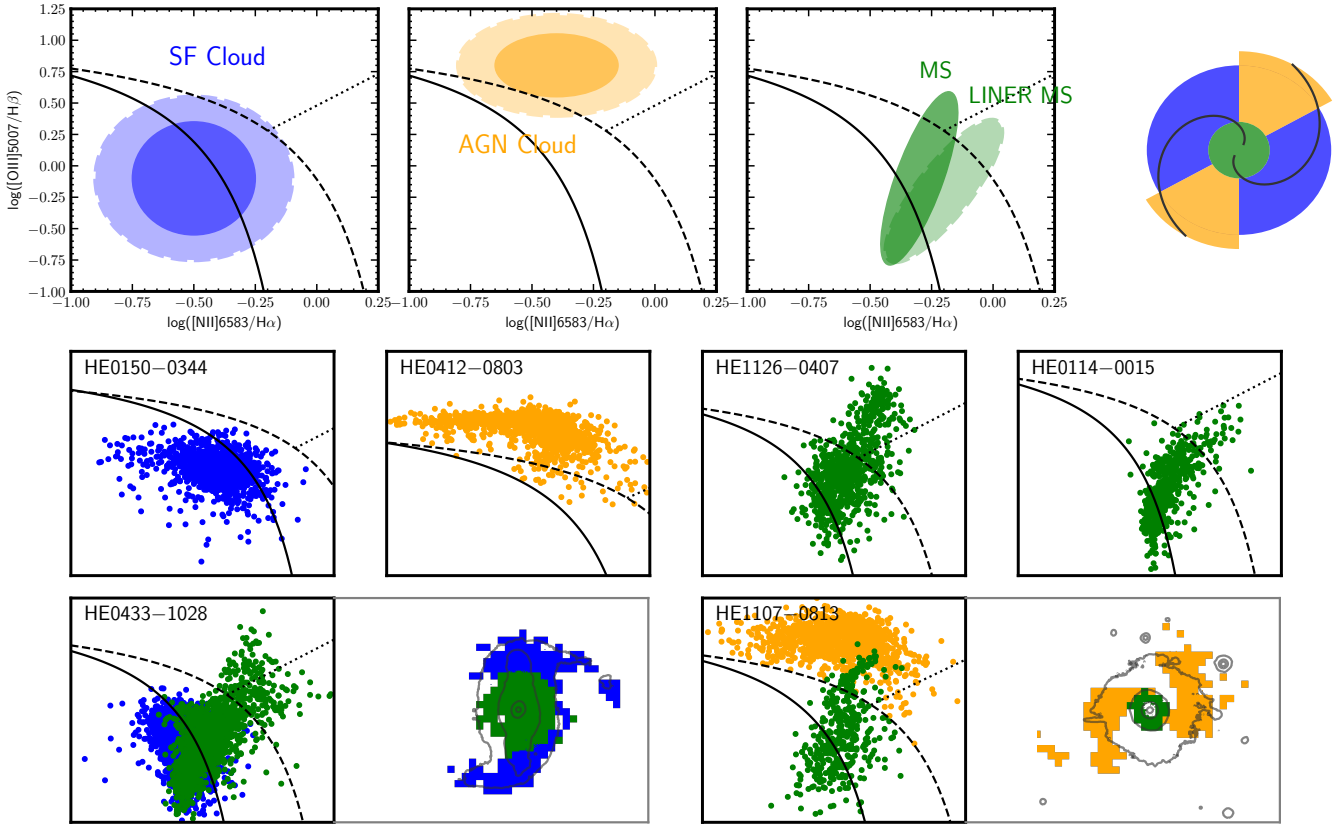
Fig. 4. Schematic sketch of the BPT morphology populations. *Upper row*: on the right there is a representation of a galaxy with a central region in green, the rest of the galactic body in blue, and an AGN ionization cone in yellow. These regions populate specific areas on the BPT diagram: *left diagram*: star-forming cloud with two different sizes; *middle diagram*: AGN-ionized cloud with two sizes; *right diagram*: mixing sequence elongated toward the AGN area and a mixing sequence elongated toward the LINER area. *Middle row*: BPT diagram schematic examples for the SF cloud, AGN cloud, mixing sequence and LINER mixing sequence dominated galaxies. *Lower row*: BPT diagram and spatial map examples for SF cloud and AGN cloud combined with a mixing sequence in one galaxy.

diagnostics are calibrated for H II regions. Their application to regions photoionized by the AGN is invalid in the majority of cases, but specific calibrations have been developed (e.g., Storchi-Bergmann et al. 1998). The metallicity measurements can in principle be restricted to H II regions ionized by star formation (as identified from BPT diagnostics) in AGN host galaxies (e.g., Husemann et al. 2014), but this approach greatly limits suitable targets and radial coverage. The [N II]/Hα (N2 index) line ratio is one of the prominent strong-line metallicity calibrators (Pettini & Pagel 2004; Marino et al. 2013) for H II regions. Photoionization models show that the N2 index should also trace the metallicity in AGN photoionized regions (e.g., Groves et al. 2006) with a different scale. That the situation is more complex was shown by Stern & Laor (2013) as they found a secondary dependence of the N2 index with AGN luminosity. At the same time they diskovered that the [N II]/[S II] (N2S2 index) is well recovering the mass–metallicity relation of galaxies for AGN hosts independent of AGN luminosity. Indeed, the N2S2 index is generally a good metallicity calibrator (Dopita et al. 2016) also for SF ionized H II regions, but not as widely used given that the diagnostic lines are significantly fainter.

In Husemann et al. (2019), we established a N2S2 index calibration based on the SDSS galaxy sample, and used it to map the gas-phase metallicity across the CARS AGN galaxy HE 1353−1917. The metallicity pattern revealed that the ENLR of the edge-on galaxy follows a very similar radial metallicity than the star forming disk. This let us conclude that the diffuse

extra-planar gas was expelled by SN-driven winds rather than an outflow from the central AGN. Here, we apply the N2S2 index calibration established in Husemann et al. (2019) for all CARS targets to infer the metallicity gradient and absolute scale of the central metallicity. In order to directly use the metallicity determined for SDSS based on Tremonti et al. (2004) we determined an N2S2 = log([N II]λ 6583/[S II]λλ 6716, 6731) calibration for this SDSS metallicity scale in the similar way as described in Husemann et al. (2019):

$$12 + \log(O/H) = 8.875 + 0.827 \times N2S2 - 0.288 \times N2S2^2. \quad (5)$$

Based on this calibration we estimated the oxygen abundance across the galaxies and reconstruct the radial metallicity gradient, as shown for the face-on disk galaxy HE 2211−3903 in Fig. 5. For this galaxy a negative radial metallicity gradient is clearly recovered with a slope of $\alpha_{O/H} = -0.055 \, \text{dex} \, r_{\text{eff}}^{-1}$ with a zero-point central metallicity of $12 + \log(O/H) = 8.732$. As expected from the work of Stern & Laor (2013), the N2S2 index indeed recovers a matching absolute metallicites even in the case of strong AGN ionization without significant offset in metallicity as shown in Fig. 5. Hence, the 2D map of the estimated oxygen abundance does not show any features related to the varying ionization conditions throughout its disk. While the [N II] and [S II] emission lines may not exactly originate from the same location within H II region, due to the ionization structure of the nebulae on 100 pc scales (e.g., Sanders et al. 2020; Mannucci et al. 2021), our calibration based on SDSS spectra (3″ apertures) consistently include also part of the surrounding diffuse
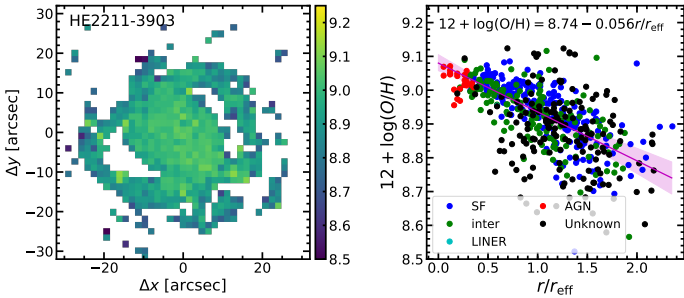
Fig. 5. Example of the 2D and radial metallicity distribution for HE 2211−3903. The oxygen abundance was measured using the N2S2 index which is almost insensitive to the excitation. On the *left panel* the full 2D distribution is shown and on the *right panel* a radial projection in units of the effective radius taken from the single Sersic model. A linear fit is performed and shown as the red line.

gas similar to our MUSE observation with typical resolutions of 0″.7–1″.0 covering 300–1000 pc depending on redshift. Because we are unable to isolate individual H II regions with CARS, any calibration based on isolated H II would be invalid.

This methodology therefore allows us an initial characterization of the metallicity for the entire sample, as listed in Table 3 and maps shown in Fig. C.1. Notably, we exclude a close star-forming companion in case of HE 0203−0031 and HE 1017−0305 from the radial fitting and fixed the center to the AGN position in all cases. As the absolute metallicity scale is strongly dependent on the underlying calibration we also transform our oxygen abundance estimate from the original O3N2 calibration scale as used in Husemann et al. (2019) to the one of Tremonti et al. (2004) so that we can more easily apply calibrations from the non-AGN SDSS sample as discussed below. Uncertainties are determined by bootstrapping; re-fitting the linear relation after randomly sub-selecting 80% of the data points.

4. Results and discussions

4.1. Finding SFR dependencies on AGN parameters

In order to investigate the potential impact of AGN on the total SFR of their host galaxies we collect the derived CARS host galaxies parameters such as AGN-corrected integrated Hα and IR luminosity and associated SFRs together with the stellar mass from our analysis presented above. From the SFRs we compute the specific SFR (sSFR) by dividing with the stellar mass, that is sSFR = SFR/$M_\star$ and compare it against the stellar mass as shown in the Fig. 6 for the Hα and IR-based SFRs, respectively.

We compare the CARS host galaxies with the non-AGN galaxy population at low redshifts using the data from SDSS (Brinchmann et al. 2004; Abazajian et al. 2009), xCOLD GASS (Saintonge et al. 2017), KINGFISH (Skibba et al. 2011), and the *Herschel* Reference Survey (HRS, Smith et al. 2012; Boselli et al. 2015). Those reference samples highlight the position of the so-called star-forming main-sequence (SFMS) as determined by various authors and is indicated on Fig. 6, with blue dashed lines. These were derived from SDSS galaxies in the Hα diagram by Renzini & Peng (2015) and Shimizu et al. (2015) for the IR diagram.

Those SFMS relations are derived from different data sets, and as our goal is to achieve consistency between the two diagrams, we consistently determine the SFMS from the xCOLD GASS (xCG) sample. The xCG is a subsample from the SDSS sample, therefore Hα, IR, stellar mass, and also CO(1−0) and

metallicity data are available from the literature sources listed above. As there is also a BPT classification of the objects, we exclude AGN and LINER galaxies to define a clean star-forming subsample of galaxies (hereafter training sample) resulting in 197 objects for the Hα diagram and 86 objects for the IR diagram. The linear SFMS fits to the training sample data and the corresponding R^2 scores (defined below in Eq. (7)) are:

$$\log L_{H\alpha} = (0.69 \pm 0.03)\log M_\star + (34.3 \pm 0.3); R^2 = 0.50$$
$$\log L_{IR} = (0.81 \pm 0.03)\log M_\star + (35.7 \pm 0.3); R^2 = 0.62. \tag{6}$$

Our SFMS linear relations are consistent with the literature determinations shown in Fig. 6 within the reported scatter.

In order to assess the differences between the CARS hosts and the training sample we compute the residuals along the SFMS relation (Fig. 6 bottom panel). The CARS objects exhibit a scatter around the SFMS of 0.69 dex based on Hα and 0.60 dex based on IR SFR, respectively, ignoring the upper limits. Moreover, the residuals reveal a clear negative correlation with a Pearson correlation coefficient of $r = -0.69$ and $r = -0.61$ for the Hα and IR SFR, respectively. This negative trend might be naïvely interpreted as a result of star-formation quenching where higher mass galaxies appear to be more passive potentially due to the effects of the AGN (e.g., Cicone et al. 2014; Saintonge et al. 2017; Lacerda et al. 2020) considering our AGN selection.

However, the stellar mass is not the only parameter which controls the SFR of a galaxy. The cold gas content was shown to be another fundamental parameter linked to the SFR and explaining part of the scatter in SFR perpendicular to the SFMS (Tacconi et al. 2018; Colombo et al. 2020; Piotrowska et al. 2020; Ellison et al. 2020). Furthermore, the gas-phase metallicity is being discussed to be linked to the SFR and stellar mass, the so-called fundamental mass–metallicity relation (Lequeux et al. 1979; Mannucci et al. 2010; Yates et al. 2012; Curti et al. 2020), but see also Sánchez et al. (2017, 2019). In particular, the metallicity could be related to the metallicity-dependent conversion of L_{CO} to the total cold gas mass (e.g., Genzel et al. 2012; Bolatto et al. 2013; Carleton et al. 2017; Utomo et al. 2017) or the general ability of the gas to cool to form star-forming gas clouds.

In order to quantitatively compare the previous model with the ones introduced further we use the coefficient of determination or the R^2 score (Draper 1998). It provides an indication of how well the fit is for the given dataset with the best possible score of 1.0. Unsuitable models can result in negative R^2 scores and an R^2 score of 0.0 would result from a constant model that always predicts the expected value. For a dataset $y_1 \ldots y_n$ with fitted values $y_{1\,model} \ldots y_{n\,model}$ and a mean value $\bar{y} = \frac{1}{n}\sum_{i=1}^{n} y_i$ the R^2 score is calculated as follows:

$$R^2 = 1 - \frac{\sum_i (y_i - y_{i\,model})^2}{\sum_i (y_i - \bar{y})^2}. \tag{7}$$

As our model above does not take into account the cold gas content nor the gas-phase metallicity of the host galaxy, we expand our one-dimensional linear model into a multi-dimensional linear model for the SFR (hereafter SFMS+gas model) with stellar mass ($M_\star$), CO(1−0) luminosity (L_{CO}) and metallicity (12 + log(O/H)) as the independent parameters. Here, we use the CO(1−0) luminosity from Saintonge et al. (2017) as the main cold gas mass proxy and the oxygen abundance 12 + log(O/H) determined from the ionized gas emission lines in the SDSS spectra as determined by Tremonti et al. (2004) as the main gas-phase metallicity parameter. This leads to the following formulas for the linear multidimensional
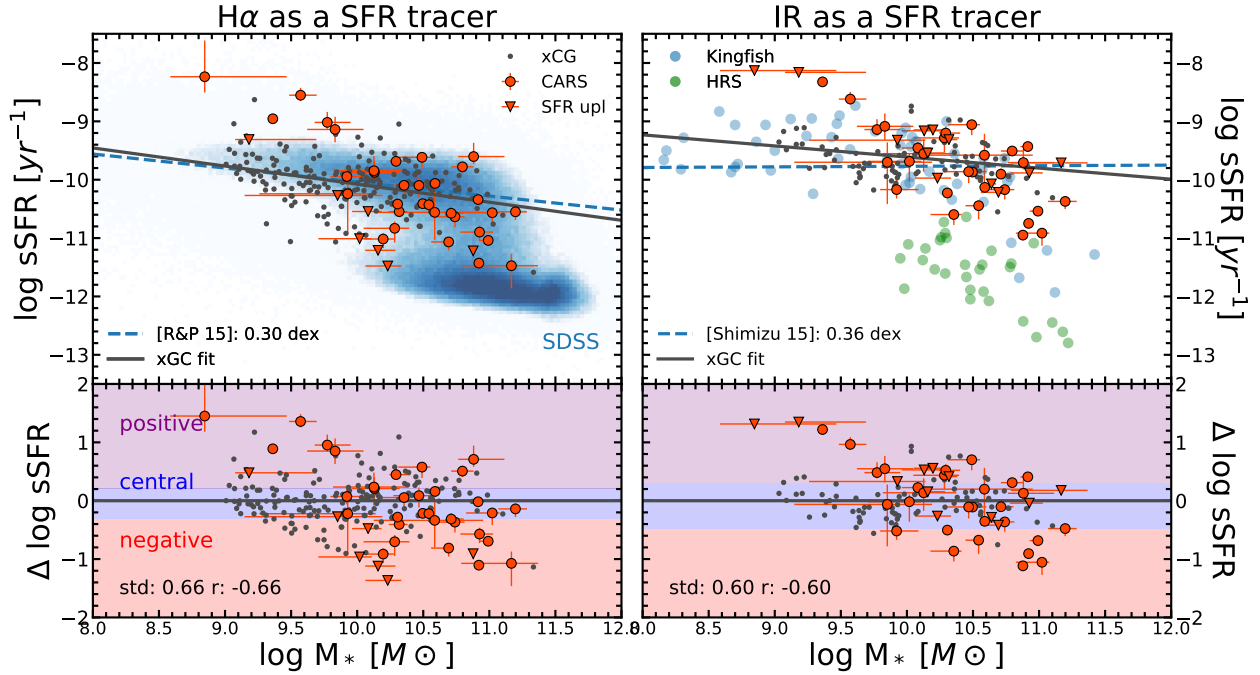
Fig. 6. Comparison of the sSFR against stellar mass for Hα- and IR-based SFR tracers. The CARS objects are shown as red points with error bars, while xCOLD GASS (xCG) are in small gray dots, KINGFISH are in blue and *Herschel* Reference Survey (HRS) in green. Specific SFR is calculated from Hα luminosity (*left panel*) derived after BPT morphology analysis and RAINBOW fitting using the SFR formula $SFR_{H\alpha} = 5.3 \times 10^{-42} \times L_{H\alpha}$ (Calzetti et al. 2007). IR specific SFR (*right panel*) derived from the AGNFITTER modeling using the Murphy et al. (2011) SFR formula. The stellar mass is taken from the AGNFITTER modeling parameters. The background on the left plot is the density map of SDSS galaxies (Brinchmann et al. 2004). Linear models to the star-forming main sequence are shown as black solid lines from Renzini & Peng (2015) and Shimizu et al. (2015), respectively. The best-fit linear relation from the xCG sample is shown as the blue dashed line in both cases. *Lower panel*: residuals around the adopted star-forming main sequence where the colored bands (red, blue, and purple) emphasize three bins used further in Fig. 8.

model

$$\log(L_{H\alpha}/[\mathrm{erg\,s^{-1}}]) = (-0.01 \pm 0.06)\log(M_\star/[M_\odot])$$
$$+ (0.62 \pm 0.04)\log(L_{CO}/[\mathrm{K\,km\,s^{-1}\,pc^2}])$$
$$+ (-0.01 \pm 0.07)(12 + \log(O/H))$$
$$+ (36.2 \pm 0.5) \tag{8}$$

$$\log(L_{IR}/[\mathrm{erg\,s^{-1}}]) = (-0.13 \pm 0.06)\log(M_\star/[M_\odot])$$
$$+ (0.98 \pm 0.04)\log(L_{CO}/[\mathrm{K\,km\,s^{-1}\,pc^2}])$$
$$+ (-1.13 \pm 0.09)(12 + \log(O/H))$$
$$+ (47.0 \pm 0.7) \tag{9}$$

with R^2 scores of $R^2 = 0.64$ and $R^2 = 0.89$, respectively.

As gas content is by far the most dominant driver compared to metallicity and metallicity may not be always measurable, we also determine relations that only rely on stellar mass and gas content:

$$\log L_{H\alpha} = (-0.01 \pm 0.06)\log(M_\star/[M_\odot])$$
$$+ (0.62 \pm 0.04)\log(L_{CO}/[\mathrm{K\,km\,s^{-1}\,pc^2}])$$
$$+ (36.2 \pm 0.3) \tag{10}$$

$$\log L_{IR} = (-0.19 \pm 0.05)\log(M_\star/[M_\odot])$$
$$+ (0.82 \pm 0.04)\log(L_{CO}/[\mathrm{K\,km\,s^{-1}\,pc^2}])$$
$$+ (38.7 \pm 0.3). \tag{11}$$

The quality of these models can be represented by R^2 scores of $R^2 = 0.64$ and $R^2 = 0.84$, respectively. As expected the quality of the model does not become significantly worse and can be

securely used for all samples where metallicity is not available. Here, we use the full model including metallicity because this parameter is available to us and so we can use it in our analysis. In any case the choice of the models does not alter our final results given the similarity of both models and low impact of metallicity.

After building the new model to predict SFR using the xCG training sample, we apply it to the CARS objects with the additional information of $L_{CO(1-0)}$ taken from Bertram et al. (2007) and $12 + \log(O/H)$ inferred from the CARS IFU observations as described above. With the new SFMS+gas model we obtain new predictions for the expected SFR of individual CARS objects and present the corresponding residuals in Fig. 7. In comparison with the previous residuals (Fig. 6 bottom panel), the residuals are significantly smaller. The scatter is reduced by a factor of two as the trend with the gas content is taken into account. The initially observed correlation with stellar mass is significantly flattened, with a correlation coefficient consistent with no remaining mass dependence. One potential issue may arise for AGN hosts as the abundance of cold gas has been suspected to be linked with the AGN either by expelling or heating the cold gas (e.g., Carniani et al. 2017; Kakkad et al. 2017; Perna et al. 2018; Bischetti et al. 2021; Circosta et al. 2021). Considering that the residual sSFR scatter is significantly reduced when incorporating cold gas mass in the SFR prediction indicates that this potential effect is negligible for our sample.

In order to understand if there are any remaining link between the residuals in sSFR and various AGN parameters we divide the residual space into three bins (negative, central, and positive residual bins) and compare the mean values of the AGN
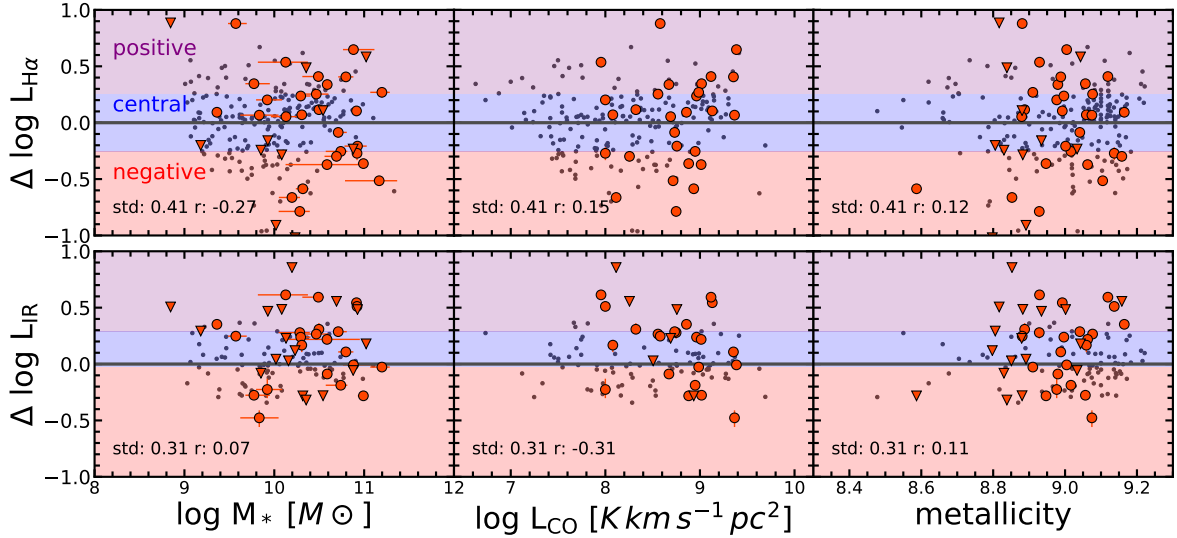
Fig. 7. Difference between measured and expected Hα (*upper panels*) and FIR luminosity (*lower panels*) as a function of stellar mass, CO(1−0) luminosity and 12 + log(O/H) ionized gas metallicity. Here we used our more complex model (Eqs. (1) and (2)) to predict the SFR-sensitive luminosities. The black dots are the data from our xCG training sample and the red symbols are the CARS data with triangles indicating upper limits. The colored bands (red, blue and purple) define three bins in residual luminosity as discussed in the text and used for Fig. 8.

parameters for each bin. The bins are created such, that the number of objects in the bins is approximately equal (with a small excess of objects in the central bin). Objects with upper limits are treated separately as we cannot necessarily associate them to a specific bin. The central residual bin for IR luminosity is shifted slightly toward higher values because of the larger number of upper limits that are too high to be informative. Those objects with upper limits are missing to populate the central and negative residuals bins, but are mostly included in the case of Hα. As we are only interested in the relative changes along the residuals we focussed to have sufficient objects in each bin for statistical reasons. In Fig. 8, we compare bins in residual SFR for the SFMS and the new SFMS+gas models for both Hα and IR SFR tracers allowing us to explore trends with BH mass, AGN luminosity, Eddington ratio and b/a host galaxy axis ratio as reported by Husemann et al. (2022) and Singha et al. (2022) for both proxies.

We find no trends of the residuals to systematically change with the $\log M_{BH}$ and $\log L_{AGN}$ given the uncertainties. While a putative correlation is seen with the fraction of objects containing extended outflows in the SFMS+gas model using the Hα proxy, it is not reflected in the IR tracer and therefore not robust. While the logarithm of the Eddington ratio ($\log \lambda_{Edd}$) has a slight increasing trend (e.g. higher AGN Eddington ratio in SFR excess systems) for the SFMS model, such a trend vanishes for the SFMS+gas model. It is important to note that most of the previous studies that investigated the impact of AGN on the SFR only used stellar mass as a proxy for the expected SFR (e.g., Page et al. 2012; Husemann et al. 2014; Shimizu et al. 2015; Balmaverde et al. 2016; Bernhard et al. 2016; Catalán-Torrecilla et al. 2017; Circosta et al. 2018; Scholtz et al. 2020). The inclusion of the cold gas mass to predict the expected SFR in addition to the stellar mass can significantly alter the derived conclusions about potential positive, negative or no AGN feedback on their host galaxies. It is therefore crucial for future studies to take more parameters into account than just stellar mass to properly characterize the parent population of non-AGN galaxies.

In Fig. 8 the geometrical parameter b/a (tracing the galaxy inclination) shows a clear trend for both Hα and IR SFRs for the

SFR model. When comparing the b/a distribution for the negative and positive residual bins with Kolmogorov–Smirnov and Anderson–Darling tests we find a highly significant difference between them for the IR SFR with a p-value of 0.003, but less significant for Hα. This suggests that dust extinction or hidden star formation is not the driver for this trend. The trend significantly flattens for the SFMS+gas model considering that the overall scatter in the residuals is greatly reduced, so that the difference become insignificant for our sample size. A potential explanation for the tentative trend might be the orientation of the AGN. The CARS objects are unobscured AGN hosts, which means that the ionization cone of the AGN is pointed to the observer. Hence, the cross-section of the AGN ionization cone which can interact with the ISM is increased when the host galaxies are closer to an edge-on geometry. Such misalignments of the galaxies rotation axis and the central AGN engine can have an important influence on the impact of the AGN on the host galaxy, as has already been proposed for various individual galaxies (e.g., García-Burillo et al. 2014; Gallimore et al. 2016; Cresci et al. 2015b; Alonso-Herrero et al. 2018; Husemann et al. 2019; Smirnova-Pinchukova et al. 2019). With the CARS sample we start to see a potential systematic trend across the population where the potential of the AGN to suppress SFR might also dependent on the relative orientation of the central engine with respect to the galaxy. However, our CARS sample is strongly limited by the low number of more edge-on systems and a bigger sample in needed to gain more insight into this process. Our results highlight that the AGN luminosity may not be the only factor determining the ability of the AGN to impact star formation. The efficiency with which the released energy can couple to the host galaxy adds complexity to the picture, where geometry is certainly just one of many additional parameters to be considered.

4.2. Comparison of SFR tracers for AGN host galaxies

Another complexity in investigating the impact of AGN on star formation is caused by the fact that different SFR indicators trace different timescales of star formation. Hα emission is related to
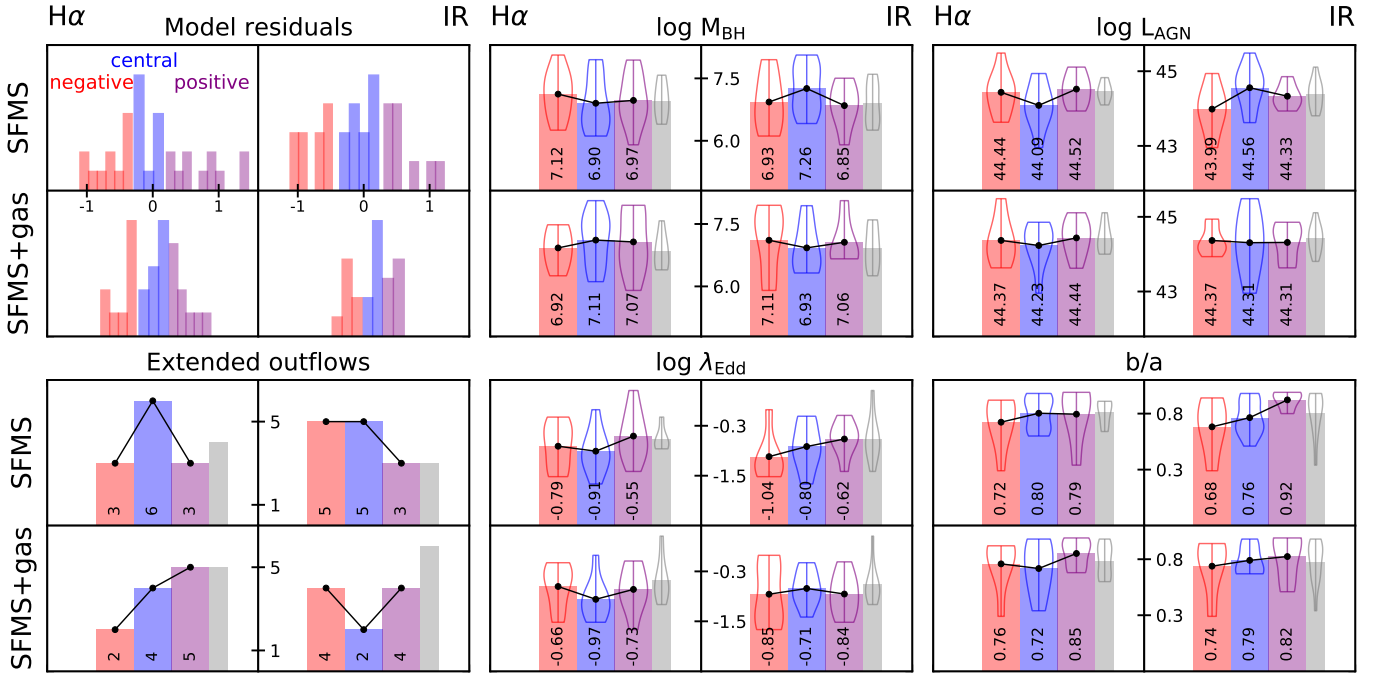
Fig. 8. Comparison of SFR residuals from the SFMS and SFMS+gas model against various AGN parameters. *Upper left panel*: histograms of the residuals for SFMS and SFMS+gas for both Hα and IR models, with the red, blue, and purple colors corresponding to the previous plots (Figs. 6 and 7, background colors). The other panels show the comparison of the AGN parameters taken from Husemann et al. (2022) and Singha et al. (2022): logarithm of BH mass (*upper center*), logarithm of AGN bolometric luminosity (*upper right*), number of the objects, containing extended outflows (*lower left*), logarithm of Eddington ratio (*lower center*), and b/a morphological parameter (*lower right*). Each of the four models is represented with three bins (*from left to right*: negative red, central blue, positive purple) and the forth bin with the upper limits (gray). The error bars of the bins also represent the distribution of the parameters within the bins. The black dots and lines highlight the trend of the mean values that are written over the bins.

the most recent star formation (∼5 Myr) as excited necessarily by hot O stars, whereas IR traces the dust heated by a wider range of stars, and, therefore traces SF over longer timescales (∼100 Myr; e.g. Kennicutt 1998b; Hayward et al. 2014; Flores Velázquez et al. 2021). Both SFR tracers are expected to be implicitly linked to the CO luminosity as a molecular gas mass tracer, because the cold gas is the necessary seed reservoir of which new stars can be formed.

By combining the SFR calibration for the IR and Hα luminosity (Eqs. (1) and (2)) we can make a prediction for their expected relation. Furthermore, we can link the SFR to the CO luminosity given the calibration of Lin et al. (2019). This leads to the following relation between the Hα luminosity and the IR and CO luminosity, respectively.

$$\log\left(\frac{L_{\mathrm{IR}}}{[\mathrm{erg\,s^{-1}}]}\right) = \log\left(\frac{L_{\mathrm{H\alpha}}}{[\mathrm{erg\,s^{-1}}]}\right) + 2.14 \qquad (12)$$

$$\log\left(\frac{L_{\mathrm{CO}}}{[\mathrm{K\,km\,s^{-1}\,pc^2}]}\right) = 0.95\log\left(\frac{L_{\mathrm{H\alpha}}}{[\mathrm{erg\,s^{-1}}]}\right) - 31.05. \qquad (13)$$

Comparing the three luminosities with each other in Fig. 9 we find that the CARS sample and the training sample from the xCG are significantly offset with respect to the predicted relation between Hα and IR luminosity. Despite this, the relation between L_{CO} and $L_{\mathrm{H\alpha}}$ as predicted from the combined Calzetti et al. (2007) and Lin et al. (2019) calibrations agree well with our data. This points to the notion that either the theoretical assumption made by Murphy et al. (2011) is inaccurate or that some of the ongoing star formation is completely obscured in Hα which cannot be recovered with an extinction correction. Nevertheless, the xCG non-AGN sample can be used as a reference because

the impact of extinction on the FIR/Hα ratio should be comparable to our AGN host galaxies. We therefore performed a linear fit directly on the xCG data and obtained the following relation which are shown as the black lines in Fig. 9:

$$\log\left(\frac{L_{\mathrm{IR}}}{[\mathrm{erg\,s^{-1}}]}\right) = 0.85\log\left(\frac{L_{\mathrm{H\alpha}}}{[\mathrm{erg\,s^{-1}}]}\right) + 8.55 \qquad (14)$$

$$\log\left(\frac{L_{\mathrm{CO}}}{[\mathrm{K\,km\,s^{-1}\,pc^2}]}\right) = 0.97\log\left(\frac{L_{\mathrm{H\alpha}}}{[\mathrm{erg\,s^{-1}}]}\right) - 31.95. \qquad (15)$$

Even though the CARS sample scatter is close to the comparison sample scatter, the CARS galaxies are on average located ∼0.2 dex above the fitted L_{IR} to $L_{\mathrm{H\alpha}}$ trend. The question here is whether this offset has a physical meaning or is just caused by low-number statistics and unknown biases of the CARS sample. Here, we claim that this offset is physical, based on two sets of evidence: (1) the CARS data are in a good agreement with the non-AGN reference sample on the L_{CO} to $L_{\mathrm{H\alpha}}$ plot; (2) the training sample also has a few galaxies, located at similarly high $L_{\mathrm{IR}}/L_{\mathrm{H\alpha}}$ ratios which drive the offset in the CARS sample. The xCG objects in this specific area of the $L_{\mathrm{IR}}/L_{\mathrm{H\alpha}}$ diagram are almost exclusively populated with galaxy mergers according to the GalaxyZoo2 classification (Willett et al. 2013; Hart et al. 2016). Those mergers seem to have a lower instantaneous $\mathrm{SFR}_{\mathrm{H\alpha}}$ compared to the slightly longer timescale IR SFR, which can be expected from the rapid star formation history evolution and bursts of star formation on 100 Myr timescale that are observed and predicted by detailed galaxy simulation (e.g., Mihos et al. 1992; Barnes 2004; Springel et al. 2005; Di Matteo et al. 2008; Hopkins et al. 2013). Considering that the offset for the CARS sample is mainly caused by individual galaxies with similarly
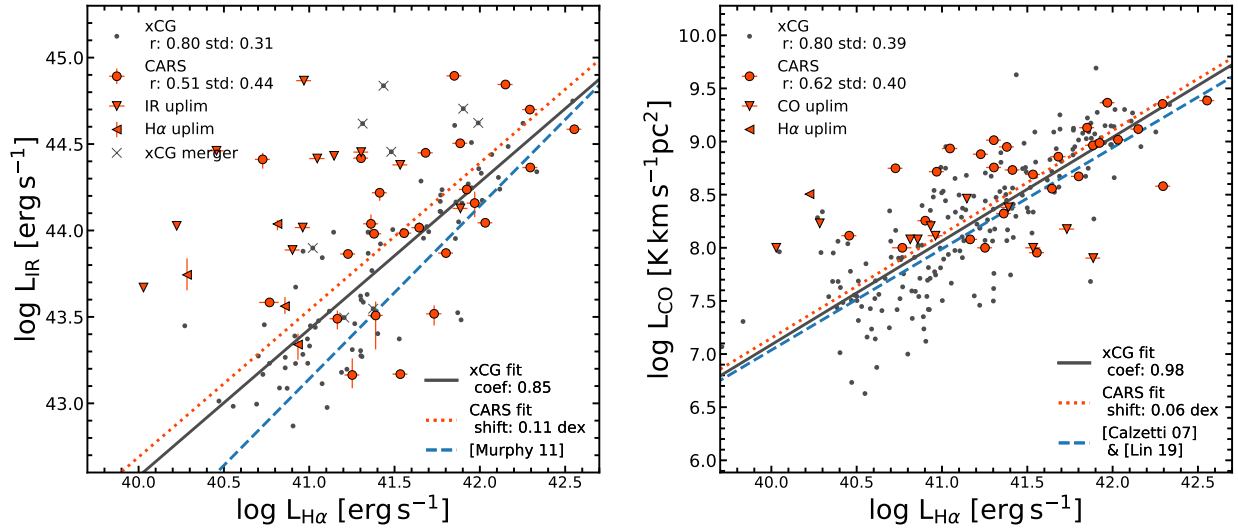
Fig. 9. 8–1000 μm IR luminosity L_{IR} (*left panel*) and the CO (1–0) luminosity L_{CO} (*right panel*) plotted against Hα luminosity. The training sample from the xCG (gray dots) is compared to the CARS objects (red circles and triangles for the 5σ upper limits). Galaxy mergers in the xCG sample as classified by GalaxyZoo2 are additionally marked (black crosses) on the *left panel*. The blue dashed line corresponds to Eqs. (12) and (13) are derived by the combination of literature calibrations as described in the main text. The black lines represent a linear relation fitted to the XCOLD GASS reference sample, see Eqs. (14) and (15). The red dotted line is fitted to the CARS objects with the same slope as the black line, therefore highlight the shift in the normalization.

high $L_{IR}/L_{Hα}$ ratio, as in the non-AGN merger sample, some AGN host galaxies potentially had higher SFR in the past (over a ~100 Myr timescale).

Whether the potential difference in the star formation history is caused by a recent excess of star formation, which might actually be linked to a delayed BH growth (e.g., Wild et al. 2010), or by ongoing suppression of star formation as expected from AGN feedback remains unclear. To shed light on these different possibilities we discuss the difference between current and recent star formation as probed by Hα and FIR emission in the following for individual objects where more information is available and can be interpreted.

4.3. Individual comparison of current and recent SFRs

In the previous subsection we compared different SFR tracers for the CARS sample with respect to the non-AGN comparison sample. Now we look at the SFR difference derived from the different SFR proxies for individual CARS galaxies and try to discuss the potential origins. We visualize the SFR results together with host galaxy morphologies and an indication for the AGN variability in Fig. 10. The AGN variability is set here by the brightness difference in the NIR photometry between old 2MASS and more recent VISTA or PANIC observations separated by a few years. The Hα-, IR- and CO-based SFR are again defined according to Eqs. (2) and (1), respectively. We plot objects with upper limits in either of the SFR traces separately as any difference between the SFR cannot be inferred on an individual basis.

The sign of the relative difference of Hα- and IR-based SFR is highlighted in green and blue color when the IR-based SFR is higher or lower compared to Hα, respectively. Assuming that the SFR timescale is the prime physical explanation for the difference (e.g., Hayward et al. 2014; Davies et al. 2015), where Hα probes more recent star formation than the IR, we can in principle differentiate between declining or enhanced star formation. In Fig. 10 we order the objects from the strongest decline to the highest enhancement in SFR. The objects HE 0253−1641, HE 0119−0118,

HE 1126−0407, HE 0045−2145, HE 2233+0124 and HE 1029−1831 belong to the declining SFR group and HE 0150−0340, HE 0212−0059, HE 0853+0102, HE 0108−4743, HE 0227−0913, HE 1338−1423, and HE 1310−1051 belong to the galaxies with potentially enhanced star formation. Below we discuss different scenarios for those individual cases that may provide physical explanations, but certainly require further tests and observations to verify.

All of these galaxies are disk-dominated and none are bulge-dominated or strongly interacting systems. Strong interactions therefore seem to play a minor role, but we still identify cases where this might be important but not obvious. In addition, bars might suppress the star formation dynamically due to bar quenching (e.g., Khoperskov et al. 2018; Fraser-McKelvie et al. 2020), but we identified nonstar forming and star forming bars in the decreasing SF group, based on the analysis of Neumann et al. (2019). While the majority of the galaxies with declining SFR are indeed barred galaxies, most of them appear star-forming contrary to expectation if they would suppress star formation. AGN or starburst-driven winds may play a role in individual cases of HE 1126−0407 and HE 0045−2145, which have both declining SFR. HE 1126−0407 (aka PG 1126−041) is known to have a powerful ultra-fast outflow driven by the AGN (Wang et al. 1999; Giustini et al. 2011) which may couple more efficiently on kpc scales (Marasco et al. 2020) as the galaxy is significantly inclined with respect to our line-of-sight and central AGN engine orientation. Furthermore, HE 0045−2145 was misclassified in the Hamburg/ESO survey because of the broader lines caused by a starburst-driven outflow (Nevin et al., in prep.). In both cases the outflow might be related to the anticipated decline in SFR. The targets HE 0253−1641 and HE 0119−0118 show high gas dispersion in the AGN-ionized region on kpc scales (see Fig. B.1 in Husemann et al. 2022) which also points to a past or ongoing galactic outflow event in these systems. Such outflow signatures are much weaker in HE 2233+0124, but the galaxy is also more edge on with a misaligned ionization cone similar to HE 1126−0407 so that the impact of the AGN may be amplified. The cause of the potential decline in the SFR of
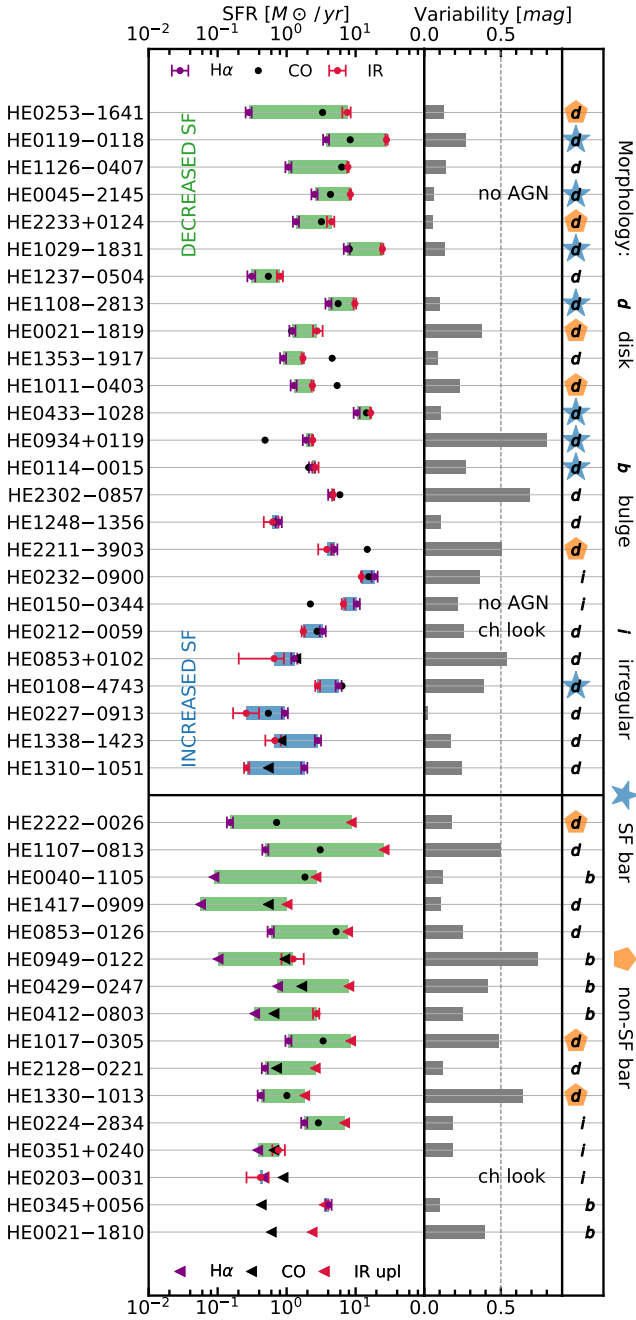
Fig. 10. Comparison of different SFR measurements for individual objects. *Left column*: Hα-, IR-, and CO(1−0)-based SFRs for the CARS objects sorted by the SFR$_{IR}$−SFR$_{Hα}$ difference. *Central column*: near infrared variability; the objects with no AGN or known changing look AGN are also marked here. *Right column*: morphology of the host galaxies. *Lower panel*: contains the objects with either Hα and/or IR SFR uncertainties (upper limits or missing data).

HE 1029−1831 is less clear, but the stellar population modeling in high-angular NIR IFU spectroscopy with SINFONI revealed a recent circumnuclear starburst about 100 Myr ago that is rapidly declining ([Busch et al. 2015](#)). Although the cause of this decline is hard to directly link to AGN feedback or simple gas consumption, it clearly supports the timescale interpretation of the difference in the Hα and FIR-based SFR.

For the objects with increased SFR, we identified HE 1310−1051 to exhibit a strong interaction with a minor companion ([Husemann et al. 2014](#)) and HE 0150−0344 to be a

strongly interacting non-AGN system. In those two cases, the interactions are most likely responsible for a recent burst of star formation. We cannot pin-point any obvious reasons why the star formation may be enhanced in HE 0212−0059, HE 0853+0102, HE 0108−4743, HE 0227−0913 and HE 1338−1423, but we note that the bolometric luminosity is close to the Eddington luminosity for the last three sources as reported in [Husemann et al. (2022)](#) due to their rather low BH mass with respect to the AGN luminosity. This is consistent with the scenario discussed in [Husemann et al. (2022)](#) that low BH mass AGN are likely to be observed in earlier phase of the AGN cycle. In this case, the circumnuclear starburst would be observed much closer than 100 Myr in time with respect to its peak activity. Indeed, narrow-line Seyfert 1 galaxies as high-Eddington ratio AGN show systematically higher SFR based on PAH emission detected with *Spitzer* ([Sani et al. 2010](#)) compared to the broad-line Seyfert 1 counterparts with lower Eddington ratios. This highlights the intriguing connection between the AGN and the circumnuclear starburst, where AGN with increasing SFR are potentially young AGN in a fueling mode powered by the starburst.

Lastly, we obtained some information on AGN variability as a side-product of our analysis when we compared old 2MASS NIR photometry with the more recent VISTA or PANIC observations. Interestingly, we see that the targets with declining SFR show systematically less variability on a few tens of years timescale. It is still speculative whether this points to a much more stable energy output of the AGN on longer timescales and thereby enhancing the impact as a cumulative effect of energy release over time. However, it shows that the process of AGN feedback is complex and the time evolution of the AGN phase with respect to the galaxy needs to be considered as well to get a comprehensive picture. Indeed, in current self-regulated feedback models ([Gaspari et al. 2020](#) for a review) the AGN is expected to flicker on-off with rapid variability that increases toward low-mass systems often due to the chaotic cold accretion feeding the SMBH (e.g., [Gaspari et al. 2015](#); [Tremblay et al. 2018](#); [Rose et al. 2019](#)).

5. Summary and conclusions

In this paper, we presented a complete census of the integrated SFR properties across the entire CARS sample using the entire multiwavelength data set available for this local AGN host galaxy sample. In particular, we inferred robust stellar masses and IR-based SFR from panchromatic SED modeling with AGNFITTER and Hα-based SFR from a careful analysis of spatially resolved optical emission-line diagnostics with our new rainbow algorithm. Using the large xCG sample of local non-AGN galaxies as a control and training set we built different models to predict the SFR for our AGN host galaxies to investigate the role of the AGN in terms of star formation feedback. Our main conclusions from this analysis can be summarized as follows:

- We find that stellar mass alone is an insufficient proxy for the expected SFR in AGN host galaxies. The cold gas content and possibly the metallicity are crucial to consider in order to avoid artificial trends with AGN parameters that could mimic expected AGN feedback trends.
- No systematic suppression of SFR could be detected with respect to the non-AGN galaxy reference sample and there is also no trend with AGN luminosity.
- A potential link between lower than expected SFRs and the axis ratio b/a of the AGN host galaxies was identified. As our sample contains only unobscured AGN, the central

engine (and thus the ionization cones) of low b/a systems must be mis-aligned with the galaxy rotation axis for inclined disks, leading to a higher cross-section of the AGN radiation field which can interact with the galaxy disk. This tentative trend is much weaker and currently insignificant for the SFR+gas model given the low-number of strongly inclined systems, but it may imply that such mis-alignments could amplify the coupling of the released AGN energy with the cold gas disk of the galaxy and thereby impact star formation more efficiently. This should be confirmed with bigger AGN host galaxies samples.

– Interpreting the IR and Hα SFR tracers as proxies for the recent star formation history on $\sim$100 Myr and $\sim$5 Myr timescales respectively, we identified systems with decreasing or increasing SFR. The declining SFR cases might often be associated with galactic outflows while the increasing SFR cases can be associated with interaction or potentially with a young AGN phase.

That we cannot find any strong evidence for a global positive or negative AGN feedback on the SFR across the entire CARS sample is in agreement with various recent studies reporting no immediate impact of AGN on the star formation (e.g., Scholtz et al. 2020). We emphasize that predicting the expected SFR of galaxies is difficult, and using stellar mass alone may not be sufficient. The cold gas mass is fundamental, and its use in such relations allows one to capture the significant scatter in the star-forming main sequence (as already demonstrated in several works for the non-AGN population; e.g., Colombo et al. 2020; Popesso et al. 2020). Despite the lack of a global and obvious impact of AGN on star formation, we diskover subtle effects that should be investigated in the future. Most importantly, the relative orientation of the AGN central engine and associated ionization cones may be relevant for the cross-section of release AGN energy and the cold gas of the galaxy. This is most prominent in disk galaxies and previously studied in several individual cases (e.g., Cecil et al. 2001; Morganti et al. 2015; Mahony et al. 2016; Mukherjee et al. 2018; Husemann et al. 2019), but CARS reveals a potential systematic trend that should be explored with larger samples in the future.

The nondetection of a relation of AGN luminosity, BH mass and Eddington ratio with the global SFR may be related to the different time scales of the AGN phase and star formation in galaxies. In case the AGN phase is short, there would not be enough time passed to see the impact on the global star formation when selecting AGN samples rather than post-starburst system as discussed in the review of Alexander & Hickox (2012) and in Hickox et al. (2014). Indeed, the CARS sample suggest a potential correlation with the duration of a luminous AGN phase as a function of BH mass (Husemann et al. 2022), which is further corroborated by current models of AGN feedback self-regulated via chaotic cold accretion (e.g., Gaspari et al. 2020). The predicted durations are on the order of 1 Myr for a single AGN phase which would be clearly too short to suppress the star formation in the entire host galaxy and can explain our observations. Still, the circumnuclear SFR could be affected on these timescales. We observed interesting patterns of increasing and decreasing SFR by comparing the IR and Hα SFR tracers among the sample that we can partially attribute to outflows, circumnuclear star formation and galaxy interaction. This highlights the potential of this approach, and also the complexity in the galaxy properties to be considered. We plan to expand the diagnostics of the star formation history determination by inferring radio-based SFR for the CARS sample which probe intermediate SFR timescale of a few tens of Myr, filling the gap in the Hα and IR-based SFRs. Furthermore, we expand our SFR investigation by zooming into the circumnuclear region of the galaxies in the CARS sample in the future. This requires the construction of an appropriate control sample with similar resolution which was beyond the scope of this paper.

Overall, we identify cold gas content, relative AGN engine orientation with respect to the host galaxy, as well as the time domain variability as potential key parameters that need to be explored in the future to understand the impact of AGN on their galaxy on a population wide basis. This leads to obvious challenges in the sample selection, sample size and parameter space to be measured to gain more insights into the putative AGN feedback process.

References

Abazajian, K. N., Adelman-McCarthy, J. K., Agüeros, M. A., et al. 2009, ApJS, 182, 543

Aird, J., Coil, A. L., Moustakas, J., et al. 2012, ApJ, 746, 90

Alam, S., Albareti, F. D., Allende Prieto, C., et al. 2015, ApJS, 219, 12

Alexander, D. M., & Hickox, R. C. 2012, New Astron. Rev., 56, 93

Alonso-Herrero, A., Pereira-Santaella, M., García-Burillo, S., et al. 2018, ApJ, 859, 144

Baade, D., Meisenheimer, K., Iwert, O., et al. 1999, The Messenger, 95, 15

Bacon, R., Accardo, M., Adjali, L., et al. 2010, Proc. SPIE, 7735, 773508

Baldry, I. K., Glazebrook, K., Brinkmann, J., et al. 2004, ApJ, 600, 681

Baldwin, J. A., Phillips, M. M., & Terlevich, R. 1981, PASP, 93, 5

Balmaverde, B., Marconi, A., Brusa, M., et al. 2016, A&A, 585, A148

Balogh, M. L., Baldry, I. K., Nichol, R., et al. 2004, ApJ, 615, L101

Barnes, J. E. 2004, MNRAS, 350, 798

Barth, A. J., Sarzi, M., Rix, H.-W., et al. 2001, ApJ, 555, 685

Bassini, L., Rasia, E., Borgani, S., et al. 2019, A&A, 630, A144

Bernhard, E., Mullaney, J. R., Daddi, E., Ciesla, L., & Schreiber, C. 2016, MNRAS, 460, 902

Bertram, T., Eckart, A., Fischer, S., et al. 2007, A&A, 470, 571

Bianchi, L., Shiao, B., & Thilker, D. 2017, ApJS, 230, 24

Bing, L., Shi, Y., Chen, Y., et al. 2019, MNRAS, 482, 194

Bischetti, M., Feruglio, C., Piconcelli, E., et al. 2021, A&A, 645, A33

Bluck, A. F. L., Maiolino, R., Sánchez, S. F., et al. 2020, MNRAS, 492, 96

Bolatto, A. D., Wolfire, M., & Leroy, A. K. 2013, ARA&A, 51, 207

Bongiorno, A., Merloni, A., Brusa, M., et al. 2012, MNRAS, 427, 3103

Bordoloi, R., Lilly, S. J., Knobel, C., et al. 2011, ApJ, 743, 10

Boselli, A., Fossati, M., Gavazzi, G., et al. 2015, A&A, 579, A102

Bouché, N., Hohensee, W., Vargas, R., et al. 2012, MNRAS, 426, 801

Bower, R. G., Benson, A. J., Malbon, R., et al. 2006, MNRAS, 370, 645

Bradley, L., Sipőcz, B., Robitaille, T., et al. 2020, https://doi.org/10.5281/zenodo.4044744

Brammer, G. B., Whitaker, K. E., van Dokkum, P. G., et al. 2009, ApJ, 706, L173

Brinchmann, J., Charlot, S., Heckman, T. M., et al. 2004, ArXiv e-prints [arXiv:astro-ph/0406220]

Brownson, S., Belfiore, F., Maiolino, R., Lin, L., & Carniani, S. 2020, MNRAS, 498, L66

Brüggen, M., & Kaiser, C. R. 2002, Nature, 418, 301

Bruzual, G., & Charlot, S. 2003, MNRAS, 344, 1000

Busch, G., Smajić, S., Scharwächter, J., et al. 2015, A&A, 575, A128

Calistro Rivera, G., Lusso, E., Hennawi, J. F., & Hogg, D. W. 2016, ApJ, 833, 98

Calzetti, D., Kennicutt, R. C., Engelbracht, C. W., et al. 2007, ApJ, 666, 870

Cárdenas Vázquez, M. C., Dorner, B., Huber, A., et al. 2018, PASP, 130, 025003

Carleton, T., Cooper, M. C., Bolatto, A. D., et al. 2017, MNRAS, 467, 4886

Carniani, S., Marconi, A., Maiolino, R., et al. 2017, A&A, 605, A105

Catalán-Torrecilla, C., Gil de Paz, A., Castillo-Morales, A., et al. 2017, ApJ, 848, 87

Cecil, G., Bland-Hawthorn, J., Veilleux, S., & Filippenko, A. V. 2001, ApJ, 555, 338

Chambers, K. C., Magnier, E. A., Metcalfe, N., et al. 2016, ArXiv e-prints [arXiv:1612.05560]

Chapin, E. L., Berry, D. S., Gibb, A. G., et al. 2013, MNRAS, 430, 2545

Chary, R., & Elbaz, D. 2001, ApJ, 556, 562

Chauke, P., van der Wel, A., Pacifici, C., et al. 2019, ApJ, 877, 48

Cicone, C., Maiolino, R., Sturm, E., et al. 2014, A&A, 562, A21

Circosta, C., Mainieri, V., Padovani, P., et al. 2018, A&A, 620, A82

Circosta, C., Mainieri, V., Lamperti, I., et al. 2021, A&A, 646, A96

Colombo, D., Sanchez, S. F., Bolatto, A. D., et al. 2020, A&A, 644, A97

Condon, J. J. 1992, ARA&A, 30, 575

Cresci, G., Mainieri, V., Brusa, M., et al. 2015a, ApJ, 799, 82

Cresci, G., Marconi, A., Zibetti, S., et al. 2015b, A&A, 582, A63

Croton, D. J., Springel, V., White, S. D. M., et al. 2006, MNRAS, 365, 11

Cutri, R. M., Wright, E. L., Conrow, T., et al. 2011, Explanatory Supplement to the WISE Preliminary Data Release Products, Tech. Rep.

Curti, M., Mannucci, F., Cresci, G., & Maiolino, R. 2020, MNRAS, 491, 944

da Cunha, E., Charlot, S., & Elbaz, D. 2008, MNRAS, 388, 1595

Dale, D. A., & Helou, G. 2002, ApJ, 576, 159

Davies, R. L., Rich, J. A., Kewley, L. J., & Dopita, M. A. 2014a, MNRAS, 439, 3835

Davies, R. L., Kewley, L. J., Ho, I. T., & Dopita, M. A. 2014b, MNRAS, 444, 3961

Davies, L. J. M., Robotham, A. S. G., Driver, S. P., et al. 2015, MNRAS, 452, 616

Davies, R. L., Groves, B., Kewley, L. J., et al. 2016, MNRAS, 462, 1616

Davies, R. L., Groves, B., Kewley, L. J., et al. 2017, MNRAS, 470, 4974

Dempsey, J. T., Friberg, P., Jenness, T., et al. 2013, MNRAS, 430, 2534

DePoy, D. L., Abbott, T., Annis, J., et al. 2008, SPIE Conf. Ser., 7014, 70140E

Di Matteo, T., Springel, V., & Hernquist, L. 2005, Nature, 433, 604

Di Matteo, P., Bournaud, F., Martig, M., et al. 2008, A&A, 492, 31

Dopita, M. A., Kewley, L. J., Sutherland, R. S., & Nicholls, D. C. 2016, Ap&SS, 361, 61

Draper, N. R. 1998, Applied Regression Analysis (New York: John Wiley & Sons)

Elbaz, D., Daddi, E., Le Borgne, D., et al. 2007, A&A, 468, 33

Elbaz, D., Dickinson, M., Hwang, H. S., et al. 2011, A&A, 533, A119

Ellison, S. L., Patton, D. R., Simard, L., & McConnachie, A. W. 2008, AJ, 135, 1877

Ellison, S. L., Thorp, M. D., Lin, L., et al. 2020, MNRAS, 493, L39

Faber, S. M., Willmer, C. N. A., Wolf, C., et al. 2007, ApJ, 665, 265

Fabian, A. C. 2012, ARA&A, 50, 455

Fabian, A. C., Sanders, J. S., Taylor, G. B., et al. 2006, MNRAS, 366, 417

Farrah, D., Urrutia, T., Lacy, M., et al. 2012, ApJ, 745, 178

Fernández-Ontiveros, J. A., Tristram, K. R. W., Hönig, S., Gandhi, P., & Weigelt, G. 2018, A&A, 611, A46

Feruglio, C., Maiolino, R., Piconcelli, E., et al. 2010, A&A, 518, L155

Fitzpatrick, E. L. 1999, PASP, 111, 63

Flores Velázquez, J. A., Gurvich, A. B., Faucher-Giguère, C.-A., et al. 2021, MNRAS, 501, 4812

Foreman-Mackey, D., Hogg, D. W., Lang, D., & Goodman, J. 2013, PASP, 125, 306

Fraser-McKelvie, A., Merrifield, M., Aragón-Salamanca, A., et al. 2020, MNRAS, 499, 1116

Gallimore, J. F., Elitzur, M., Maiolino, R., et al. 2016, ApJ, 829, L7

García-Burillo, S., Combes, F., Usero, A., et al. 2014, A&A, 567, A125

Gaspari, M., Brighenti, F., & Temi, P. 2015, A&A, 579, A62

Gaspari, M., Eckert, D., Ettori, S., et al. 2019, ApJ, 884, 169

Gaspari, M., Tombesi, F., & Cappi, M. 2020, Nat. Astron., 4, 10

Genzel, R., Tacconi, L. J., Combes, F., et al. 2012, ApJ, 746, 69

Giustini, M., Cappi, M., Chartas, G., et al. 2011, A&A, 536, A49

Groves, B. A., Heckman, T. M., & Kauffmann, G. 2006, MNRAS, 371, 1559

Harper, S. M., Runyan, M. C., Dowell, C. D., et al. 2018, J. Astron. Instrum., 7, 1840008

Harrison, C. M., Alexander, D. M., Mullaney, J. R., et al. 2012, ApJ, 760, L15

Hart, R. E., Bamford, S. P., Willett, K. W., et al. 2016, MNRAS, 461, 3663

Hasinger, G. 2008, A&A, 490, 905

Hayward, C. C., Lanz, L., Ashby, M. L. N., et al. 2014, MNRAS, 445, 1598

Henden, A. A., Welch, D. L., Terrell, D., & Levine, S. E. 2009, Am. Astron. Soc. Meet. Abstr., 214, 407.02

Hickox, R. C., Mullaney, J. R., Alexander, D. M., et al. 2014, ApJ, 782, 9
Ho, L. C. 2005, ApJ, 629, 680
Holland, W. S., Bintley, D., Chapin, E. L., et al. 2013, MNRAS, 430, 2513
Hopkins, P. F., & Elvis, M. 2010, MNRAS, 401, 7
Hopkins, P. F., Hernquist, L., Cox, T. J., & Kereš, D. 2008, ApJS, 175, 356
Hopkins, P. F., Cox, T. J., Hernquist, L., et al. 2013, MNRAS, 430, 1901
Husemann, B., Jahnke, K., Sánchez, S. F., et al. 2014, MNRAS, 443, 755
Husemann, B., Scharwächter, J., Davis, T. A., et al. 2019, A&A, 627, A53
Husemann, B., Singha, M., Scharwächter, J., et al. 2022, A&A, 659, A124
Jarrett, T. H., Chester, T., Cutri, R., et al. 2000, AJ, 119, 2498
Kakkad, D., Mainieri, V., Brusa, M., et al. 2017, MNRAS, 468, 4205
Karim, A., Schinnerer, E., Martínez-Sansigre, A., et al. 2011, ApJ, 730, 61
Kauffmann, G., Heckman, T. M., Tremonti, C., et al. 2003, MNRAS, 346, 1055
Kennicutt, R. C., Jr. 1998a, ARA&A, 36, 189
Kennicutt, R. C., Jr. 1998b, ApJ, 498, 541
Kennicutt, R. C., Jr., & Kent, S. M. 1983, AJ, 88, 1094
Kewley, L. J., & Ellison, S. L. 2008, ApJ, 681, 1183
Kewley, L. J., Dopita, M. A., Sutherland, R. S., Heisler, C. A., & Trevena, J.
    2001, ApJ, 556, 121
Kewley, L. J., Geller, M. J., & Jansen, R. A. 2004, AJ, 127, 2002
Kewley, L. J., Groves, B., Kauffmann, G., & Heckman, T. 2006, MNRAS, 372,
    961
Kewley, L. J., Rupke, D., Jabran Zahid, H., Geller, M. J., & Barton, E. J. 2010,
    ApJ, 721, L48
Khoperskov, S., Haywood, M., Di Matteo, P., Lehnert, M. D., & Combes, F.
    2018, A&A, 609, A60
Kim, M., Ho, L. C., & Im, M. 2006, ApJ, 642, 702
Koss, M. J., Strittmatter, B., Lamperti, I., et al. 2021, ApJS, 252, 29
Lacerda, E. A. D., Sánchez, S. F., Cid Fernandes, R., et al. 2020, MNRAS, 492,
    3073
Le Févre, O., Saisse, M., Mancini, D., et al. 2003, Proc. SPIE, 4841, 1671
Lequeux, J., Peimbert, M., Rayo, J. F., Serrano, A., & Torres-Peimbert, S. 1979,
    A&A, 500, 145
Leung, G. C. K., Coil, A. L., Azadi, M., et al. 2017, ApJ, 849, 48
Lin, L., Pan, H.-A., Ellison, S. L., et al. 2019, ApJ, 884, L33
Madau, P., & Dickinson, M. 2014, ARA&A, 52, 415
Mahony, E. K., Oonk, J. B. R., Morganti, R., et al. 2016, MNRAS, 455, 2453
Maiolino, R., Gallerani, S., Neri, R., et al. 2012, MNRAS, 425, L66
Maiolino, R., Russell, H. R., Fabian, A. C., et al. 2017, Nature, 544, 202
Mancini, C., Daddi, E., Juneau, S., et al. 2019, MNRAS, 489, 1265
Mannucci, F., Cresci, G., Maiolino, R., Marconi, A., & Gnerucci, A. 2010,
    MNRAS, 408, 2115
Mannucci, F., Belfiore, F., Curti, M., et al. 2021, MNRAS, 508, 1582
Marasco, A., Cresci, G., Nardini, E., et al. 2020, A&A, 644, A15
Marino, R. A., Rosales-Ortega, F. F., Sánchez, S. F., et al. 2013, A&A, 559, A114
Martin, P., & Roy, J.-R. 1994, ApJ, 424, 599
McDonald, M., McNamara, B. R., Calzadilla, M. S., et al. 2021, ApJ, 908, 85
McNamara, B. R., & Nulsen, P. E. J. 2007, ARA&A, 45, 117
McNamara, B. R., Nulsen, P. E. J., Wise, M. W., et al. 2005, Nature, 433, 45
Mignoli, M., Vignali, C., Gilli, R., et al. 2013, A&A, 556, A29
Mihos, J. C., Richstone, D. O., & Bothun, G. D. 1992, ApJ, 400, 153
Mommert, M. 2017, Astron. Comput., 18, 47
Morganti, R., Oosterloo, T., Oonk, J. B. R., Frieswijk, W., & Tadhunter, C. 2015,
    A&A, 580, A1
Mukherjee, D., Wagner, A. Y., Bicknell, G. V., et al. 2018, MNRAS, 476, 80
Mullaney, J. R., Alexander, D. M., Aird, J., et al. 2015, MNRAS, 453, L83
Murphy, E. J., Condon, J. J., Schinnerer, E., et al. 2011, ApJ, 737, 67
Nandra, K., Georgakakis, A., Willmer, C. N. A., et al. 2007, ApJ, 660, L11
Nascimento, J. C. D., Storchi-Bergmann, T., Mallmann, N. D., et al. 2019,
    MNRAS, 486, 5075
Nelson, D., Pillepich, A., Springel, V., et al. 2018, MNRAS, 475, 624
Nesvadba, N. P. H., Lehnert, M. D., De Breuck, C., Gilbert, A. M., & van
    Breugel, W. 2008, A&A, 491, 407
Neumann, J., Gadotti, D. A., Wisotzki, L., et al. 2019, A&A, 627, A26
Nielsen, N. M., Churchill, C. W., Kacprzak, G. G., Murphy, M. T., & Evans, J.
    L. 2015, ApJ, 812, 83
Noeske, K. G., Weiner, B. J., Faber, S. M., et al. 2007, ApJ, 660, L43
Noll, S., Burgarella, D., Giovannoli, E., et al. 2009, A&A, 507, 1793
Page, M. J., Symeonidis, M., Vieira, J. D., et al. 2012, Nature, 485, 213
Peng, C. Y., Ho, L. C., Impey, C. D., & Rix, H.-W. 2002, AJ, 124, 266
Peng, Y.-J., Lilly, S. J., Kovač, K., et al. 2010, ApJ, 721, 193
Perna, M., Sargent, M. T., Brusa, M., et al. 2018, A&A, 619, A90
Pettini, M., & Pagel, B. E. J. 2004, MNRAS, 348, L59
Pillepich, A., Springel, V., Nelson, D., et al. 2018, MNRAS, 473, 4077
Piotrowska, J. M., Bluck, A. F. L., Maiolino, R., Concas, A., & Peng, Y. 2020,
    MNRAS, 492, L6
Popesso, P., Concas, A., Morselli, L., et al. 2020, MNRAS, 496, 2531

Prevot, M. L., Lequeux, J., Maurice, E., Prevot, L., & Rocca-Volmerange, B.
    1984, A&A, 132, 389
Ramos Padilla, A. F., Ashby, M. L. N., Smith, H. A., et al. 2020, MNRAS, 499,
    4325
Renzini, A., & Peng, Y.-J. 2015, ApJ, 801, L29
Rosario, D. J. 2019, Astrophysics Source Code Library [record ascl:1904.011]
Rosario, D. J., Alexander, D. M., Moldon, J., et al. 2021, MNRAS, 505, 5283
Rose, T., Edge, A. C., Combes, F., et al. 2019, MNRAS, 489, 349
Roth, M. M., Kelz, A., Fechner, T., et al. 2005, PASP, 117, 620
Saintonge, A., Catinella, B., Tacconi, L. J., et al. 2017, ApJS, 233, 22
Salim, S., Rich, R. M., Charlot, S., et al. 2007, ApJS, 173, 267
Sánchez, S. F., Rosales-Ortega, F. F., Iglesias-Páramo, J., et al. 2014, A&A, 563,
    A49
Sánchez, S. F., Barrera-Ballesteros, J. K., Sánchez-Menguiano, L., et al. 2017,
    MNRAS, 469, 2121
Sánchez, S. F., Barrera-Ballesteros, J. K., López-Cobá, C., et al. 2019, MNRAS,
    484, 3042
Sanders, R. L., Jones, T., Shapley, A. E., et al. 2020, ApJ, 888, L11
Sani, E., Lutz, D., Risaliti, G., et al. 2010, MNRAS, 403, 1246
Santoro, F., Oonk, J. B. R., Morganti, R., Oosterloo, T. A., & Tadhunter, C. 2016,
    A&A, 590, A37
Schaefer, A. L., Croom, S. M., Scott, N., et al. 2019, MNRAS, 483, 2851
Schawinski, K., Virani, S., Simmons, B., et al. 2009, ApJ, 692, L19
Schawinski, K., Urry, C. M., Simmons, B. D., et al. 2014, MNRAS, 440, 889
Schaye, J., Crain, R. A., Bower, R. G., et al. 2015, MNRAS, 446, 521
Schirmer, M. 2013, ApJS, 209, 21
Schlafly, E. F., & Finkbeiner, D. P. 2011, ApJ, 737, 103
Scholtz, J., Harrison, C. M., Rosario, D. J., et al. 2020, MNRAS, 492, 3194
Schroetter, I., Bouché, N. F., Zabl, J., et al. 2019, MNRAS, 490, 4368
Schulz, B., Marton, G., Valtchanov, I., et al. 2017, ArXiv e-prints
    [arXiv:1706.00448]
Shangguan, J., Ho, L. C., & Xie, Y. 2018, ApJ, 854, 158
Shimizu, T. T., Mushotzky, R. F., Meléndez, M., Koss, M., & Rosario, D. J. 2015,
    MNRAS, 452, 1841
Silva, L., Granato, G. L., Bressan, A., & Danese, L. 1998, ApJ, 509, 103
Silva, L., Maiolino, R., & Granato, G. L. 2004, MNRAS, 355, 973
Silverman, J. D., Lamareille, F., Maier, C., et al. 2009, ApJ, 696, 396
Singha, M., Husemann, B., Urrutia, T., et al. 2022, A&A, 659, A123
Skibba, R. A., Engelbracht, C. W., Dale, D., et al. 2011, ApJ, 738, 89
Smirnova-Pinchukova, I., Husemann, B., Busch, G., et al. 2019, A&A, 626, L3
Smith, M. W. L., Gomez, H. L., Eales, S. A., et al. 2012, ApJ, 748, 123
Smith, K. L., Koss, M., Mushotzky, R., et al. 2020, ApJ, 904, 83
Speagle, J. S., Steinhardt, C. L., Capak, P. L., & Silverman, J. D. 2014, ApJS,
    214, 15
Springel, V., Di Matteo, T., & Hernquist, L. 2005, MNRAS, 361, 776
Stern, J., & Laor, A. 2013, MNRAS, 431, 836
Storchi-Bergmann, T., Schmitt, H. R., Calzetti, D., & Kinney, A. L. 1998, AJ,
    115, 909
Strateva, I., Ivezić, Ž., Knapp, G. R., et al. 2001, AJ, 122, 1861
Tacconi, L. J., Genzel, R., Saintonge, A., et al. 2018, ApJ, 853, 179
Thorp, M. D., Ellison, S. L., Simard, L., Sánchez, S. F., & Antonio, B. 2019,
    MNRAS, 482, L55
Tremblay, G. R., Combes, F., Oonk, J. B. R., et al. 2018, ApJ, 865, 13
Tremonti, C. A., Heckman, T. M., Kauffmann, G., et al. 2004, ApJ, 613, 898
Tumlinson, J., Thom, C., Werk, J. K., et al. 2011, Science, 334, 948
Utomo, D., Bolatto, A. D., Wong, T., et al. 2017, ApJ, 849, 26
Valdes, F., Gruendl, R., & DES Project 2014, ASP Conf. Ser., 485, 379
Vogelsberger, M., Genel, S., Springel, V., et al. 2014a, MNRAS, 444, 1518
Vogelsberger, M., Genel, S., Springel, V., et al. 2014b, Nature, 509, 177
Walcher, C. J., Coelho, P. R. T., Gallazzi, A., et al. 2015, A&A, 582, A46
Walsh, J. L., Barth, A. J., Ho, L. C., & Sarzi, M. 2013, ApJ, 770, 86
Wang, T. G., Brinkmann, W., Wamsteker, W., Yuan, W., & Wang, J. X. 1999,
    MNRAS, 307, 821
Weaver, J., Husemann, B., Kuntschner, H., et al. 2018, A&A, 614, A32
Wild, V., Heckman, T., & Charlot, S. 2010, MNRAS, 405, 933
Willett, K. W., Lintott, C. J., Bamford, S. P., et al. 2013, MNRAS, 435, 2835
Wisotzki, L., Christlieb, N., Bade, N., et al. 2000, A&A, 358, 77
Wittor, D., & Gaspari, M. 2020, MNRAS, 498, 4983
Wolf, C., Onken, C. A., Luvaul, L. C., et al. 2018, PASA, 35, e010
Woo, J.-H., Son, D., & Bae, H.-J. 2017, ApJ, 839, 120
Wyder, T. K., Martin, D. C., Schiminovich, D., et al. 2007, ApJS, 173, 293
Wylezalek, D., & Zakamska, N. L. 2016, MNRAS, 461, 3724
Wylezalek, D., Zakamska, N. L., Greene, J. E., et al. 2018, MNRAS, 474, 1499
Yamamura, I., Makiuti, S., Ikeda, N., et al. 2009, ASP Conf. Ser., 418, 3
Yang, G., Boquien, M., Buat, V., et al. 2020, MNRAS, 491, 740
Yates, R. M., Kauffmann, G., & Guo, Q. 2012, MNRAS, 422, 215
York, D. G., Adelman, J., Anderson, J. E., Jr., et al. 2000, AJ, 120, 1579

Appendix A: SED models
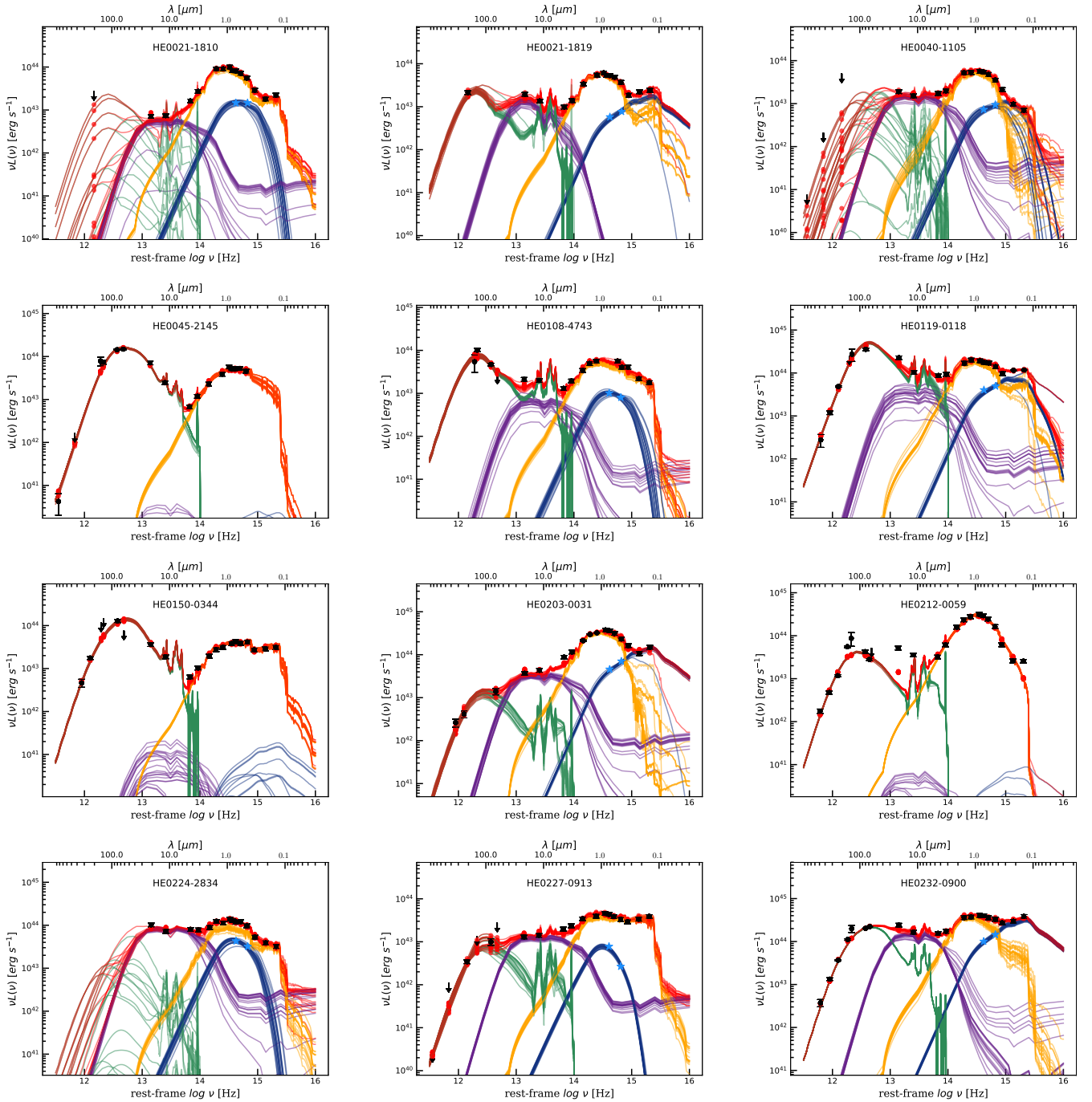
Fig. A.1. Overview of the `AGNfitter` SED modeling results for the entire CARS sample. Black data points represent the measured panchromatic photometry collected for each object. Upper limits are highlighted as black arrows. The red dots are the predicted photometry for XX MCMC relations from the superposition of individual SED components. The red, yellow, blue, purple and green lines correspond to the total SED, the stellar component, the AGN component, the hot dust component and the cold dust component, respectively.
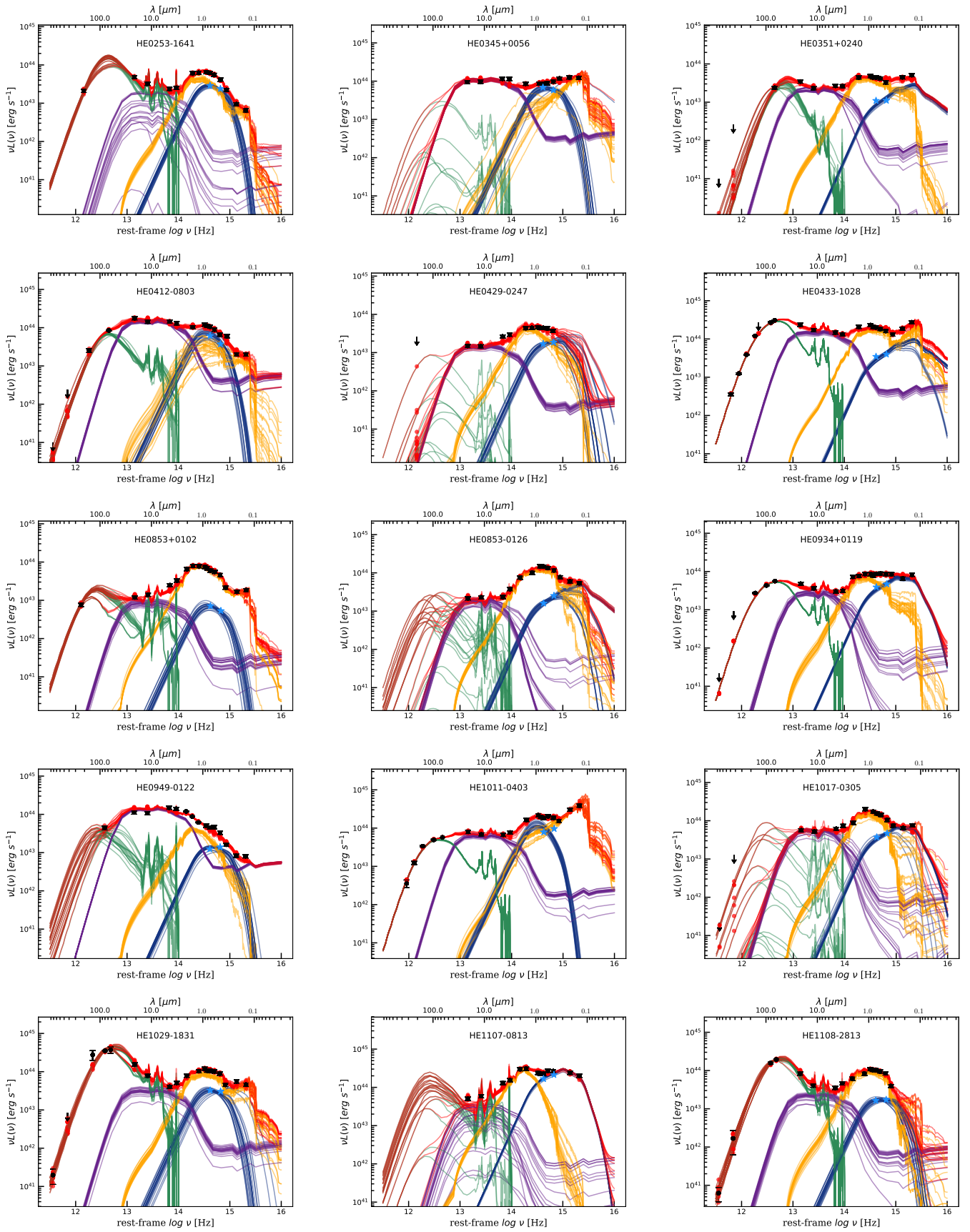
Fig. A.1. continued.
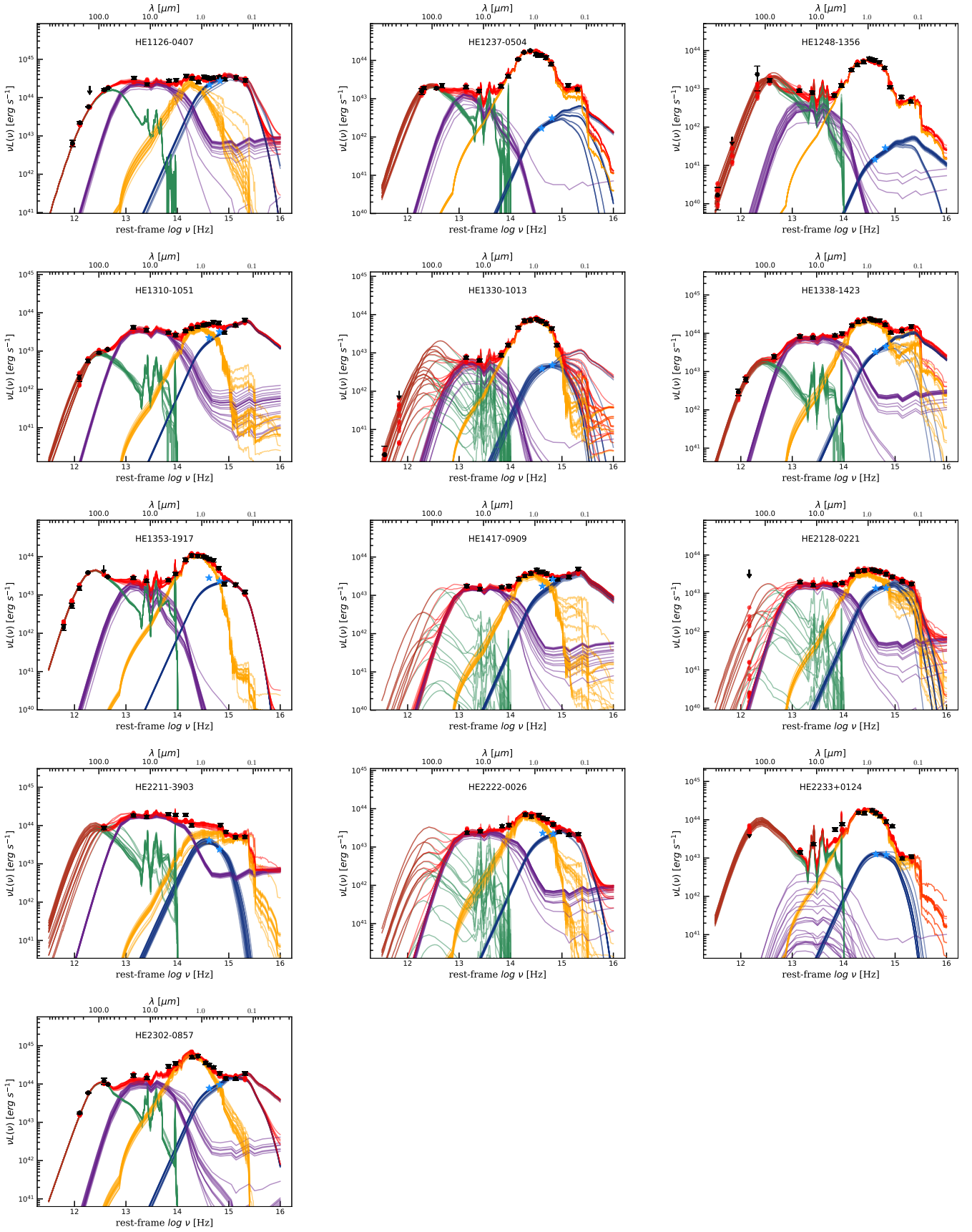
Fig. A.1. continued.

Appendix B: CARS sample BPT morphology

Table B.1. Separation radii for galaxies with star-forming and/or AGN-ionised cloud.

Object	SF radius [arcsec]	AGN radius [arcsec]
HE 0021−1810	15.0	—
HE 0351+0240	—	7.0
HE 0433−1028	9.0	—
HE 1107−0813	7.0	4.0
HE 1108−2813	13.0	—
HE 1237−0504	7.0	—
HE 1353−1917	15.0	5.0
HE 2211−3903	13.0	—
HE 2233+0124	—	3.0

Notes. SF and AGN cloud spaxels are located outside of the corresponding spatial radii.
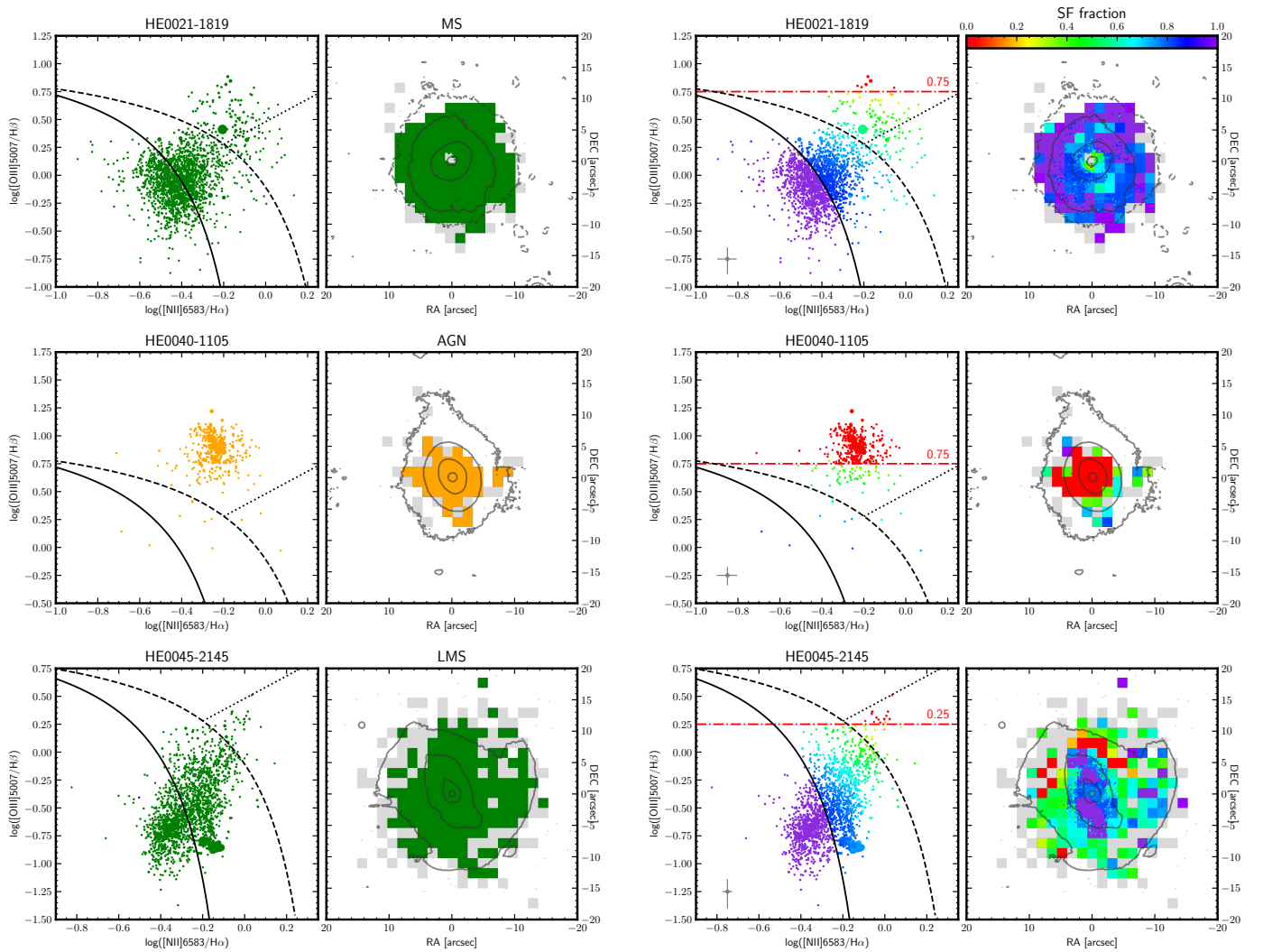
Fig. B.1. BPT morphology and RAINBOW results for the sample. The BPT and a spatial map for each galaxy show SF fraction. The red dotted line shows the threshold for the AGN basis spaxels. The contours on the maps represent MUSE whitelight contours. The gray pixels on the maps represent those pixels, where Hα S/N is more than 3σ, but the other lines are weaker so the datapoint cannot be shown on a BPT.
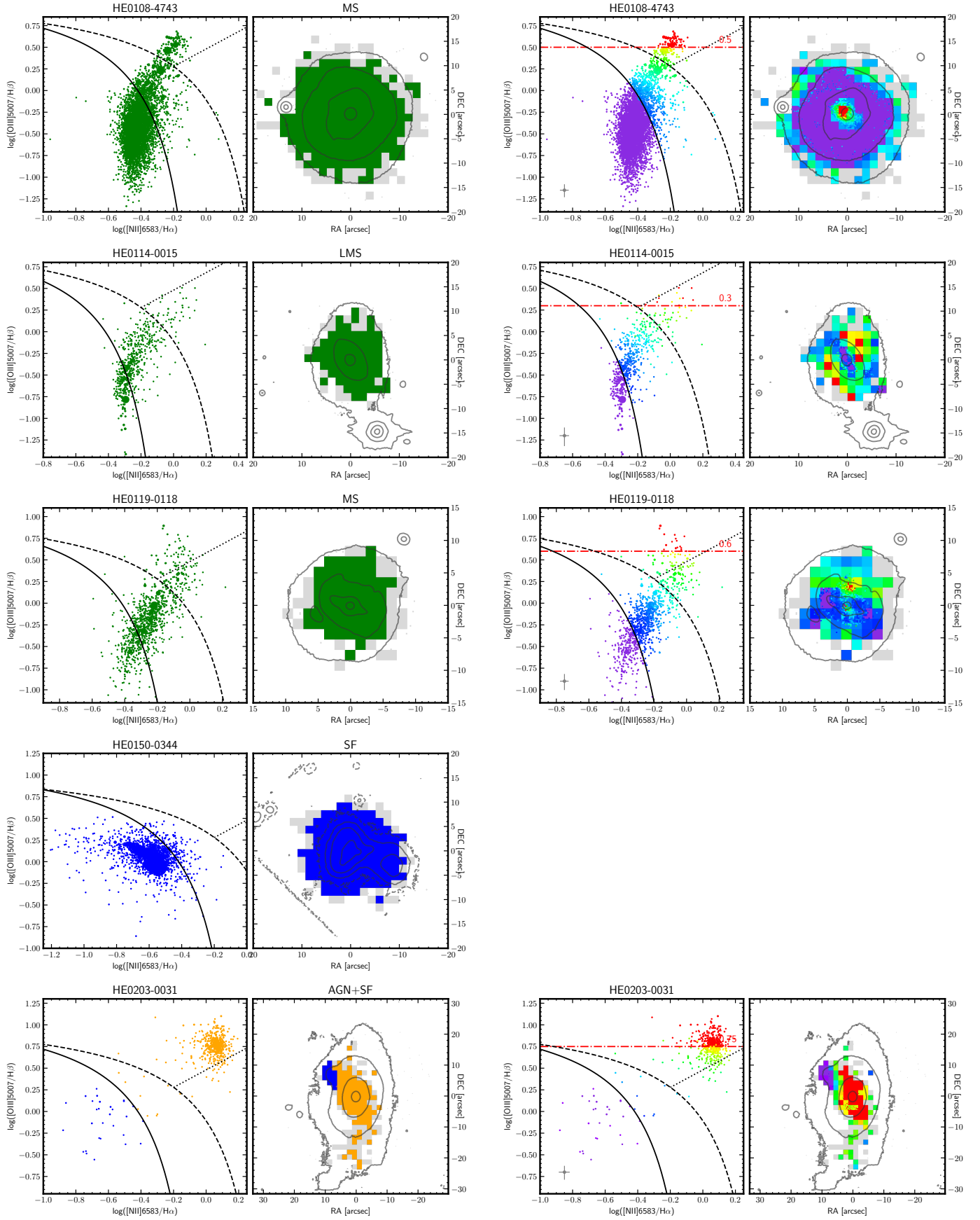
Fig. B.1. continued.
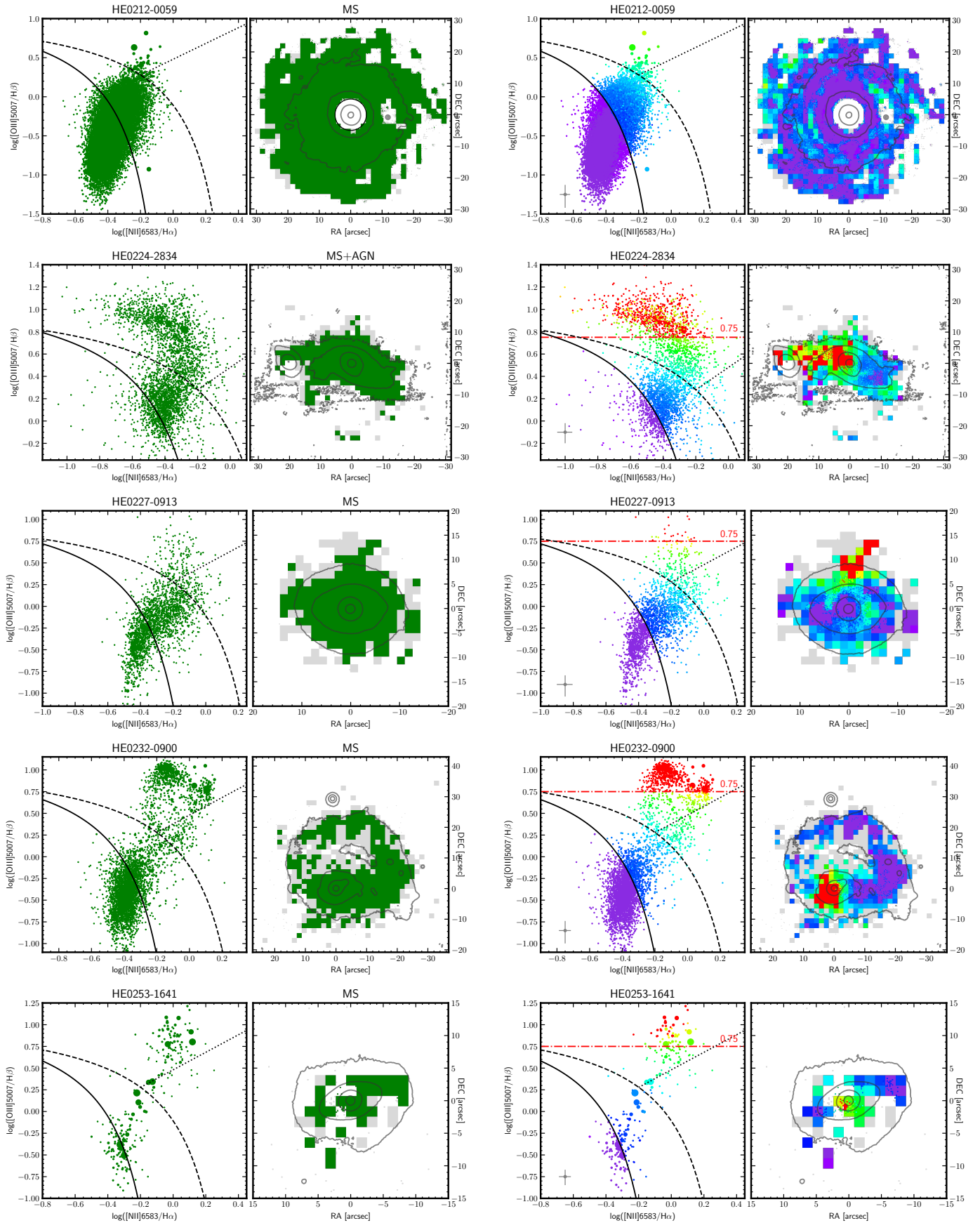
Fig. B.1. continued.
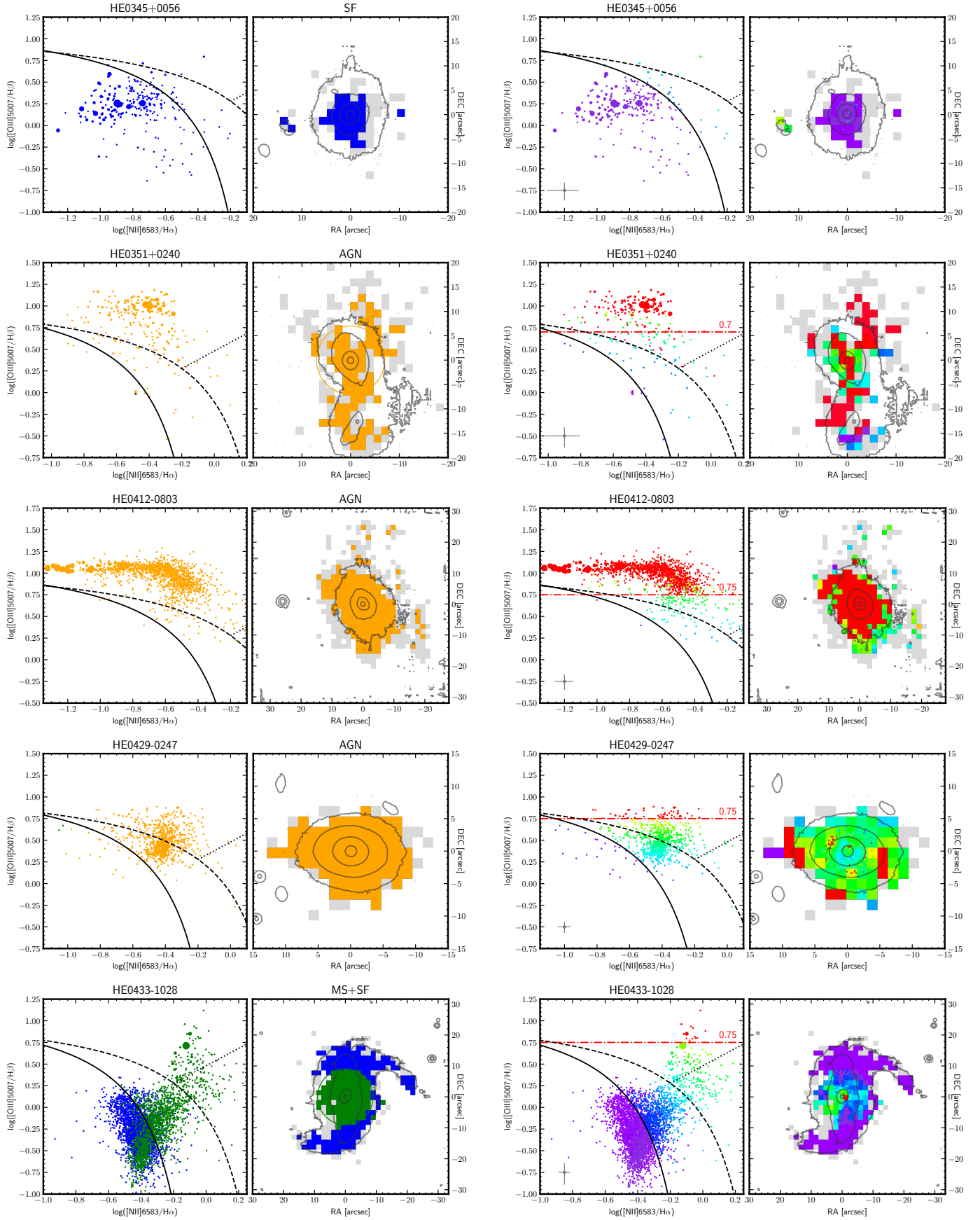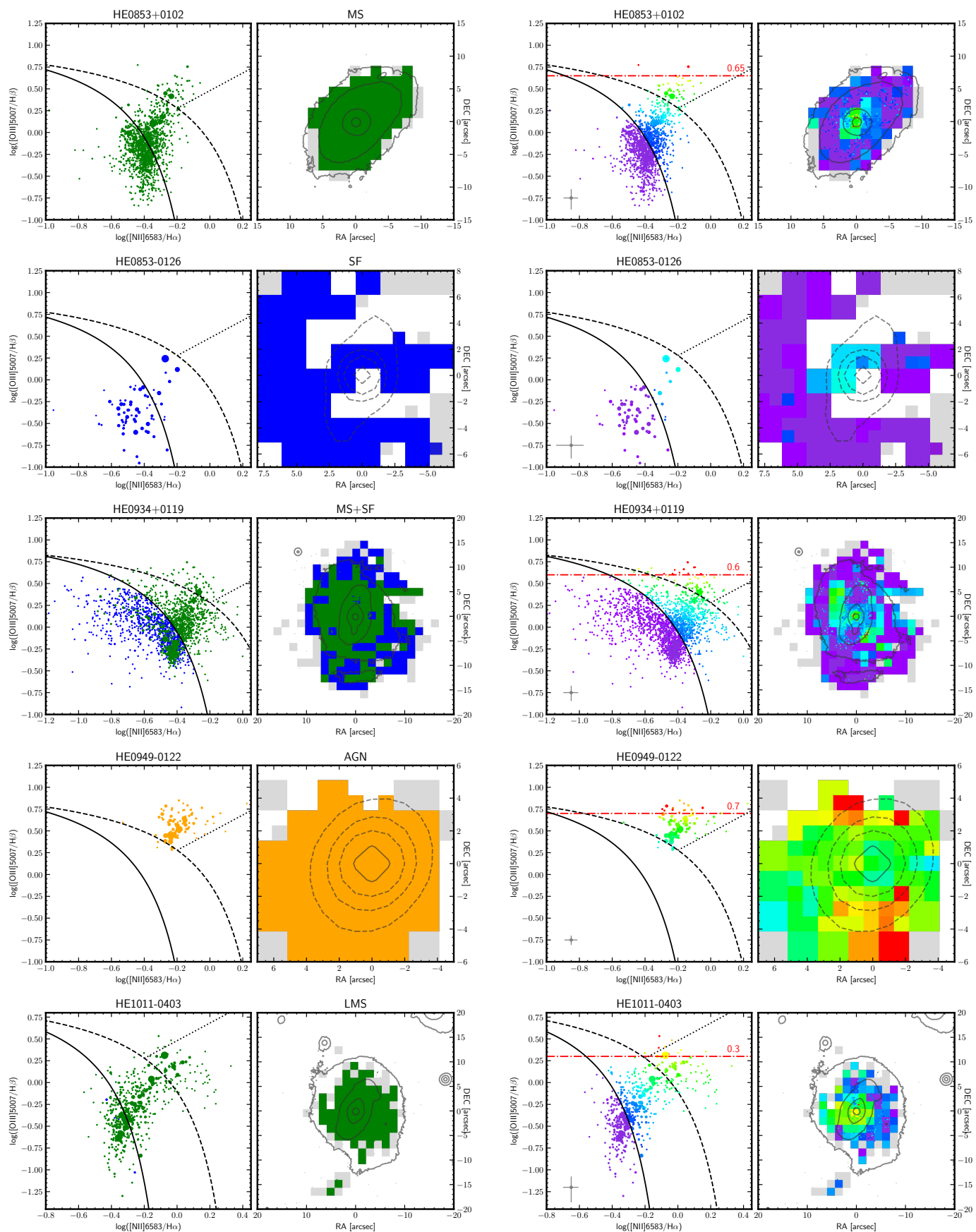
Fig. B.1. continued.
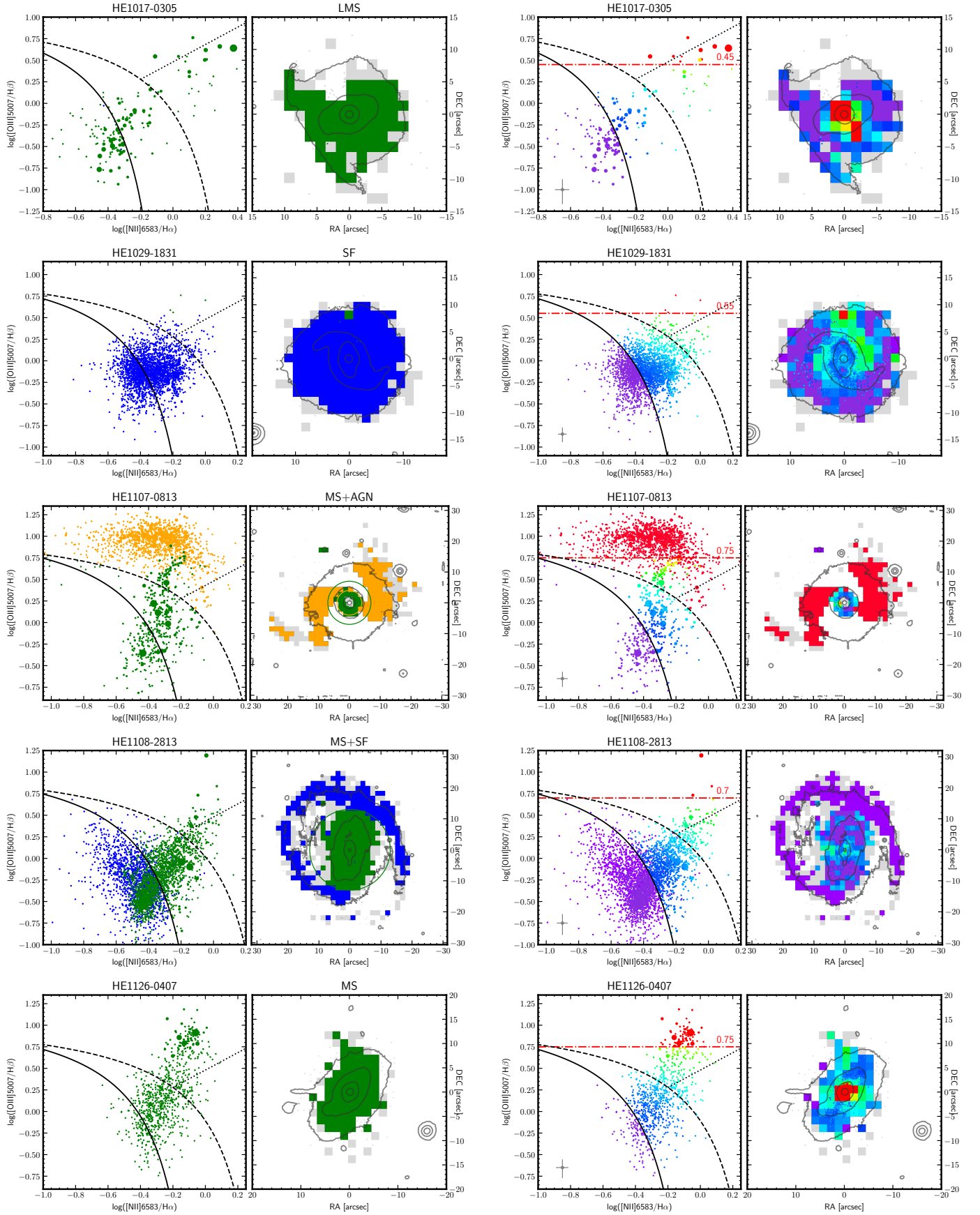
Fig. B.1. continued.
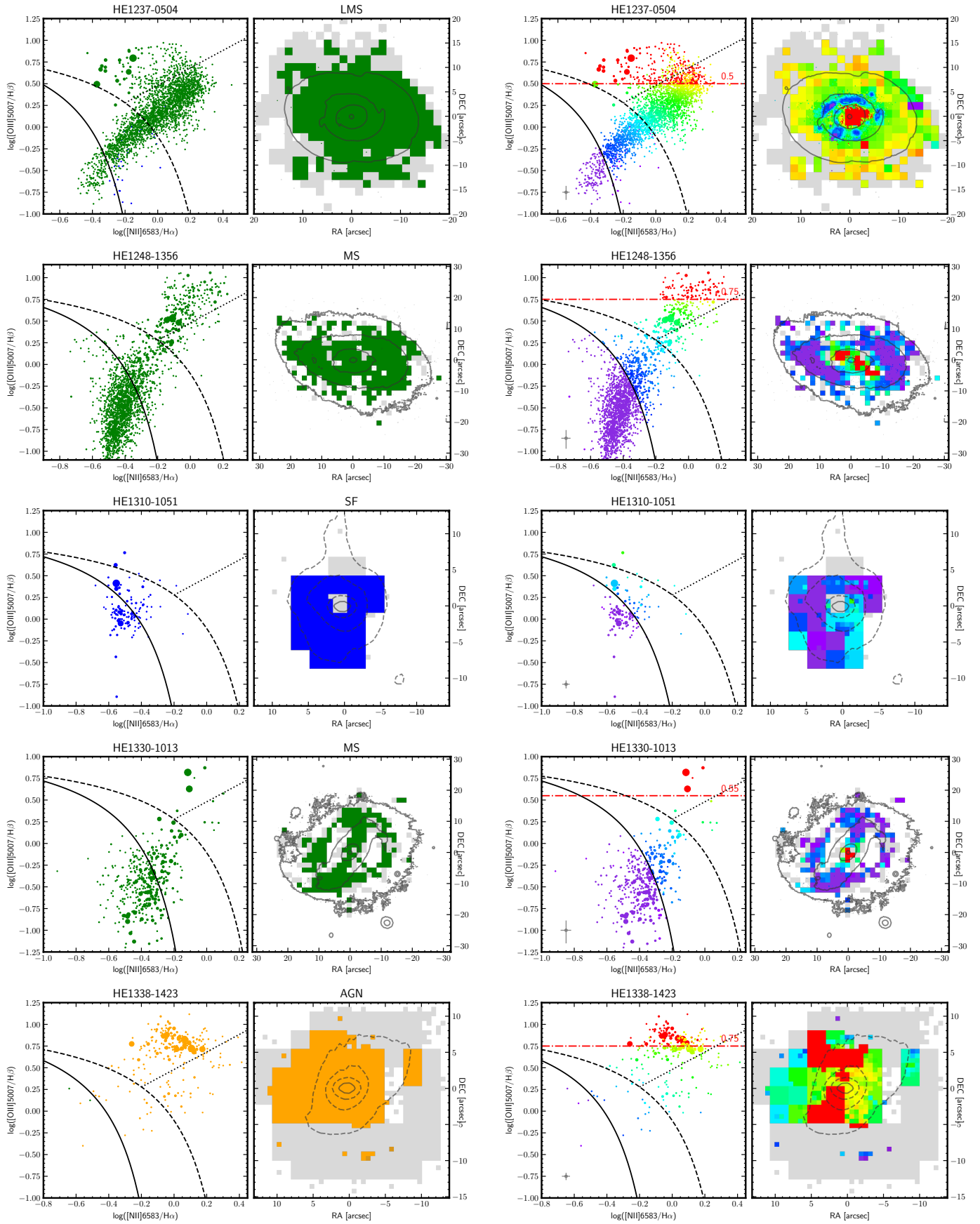
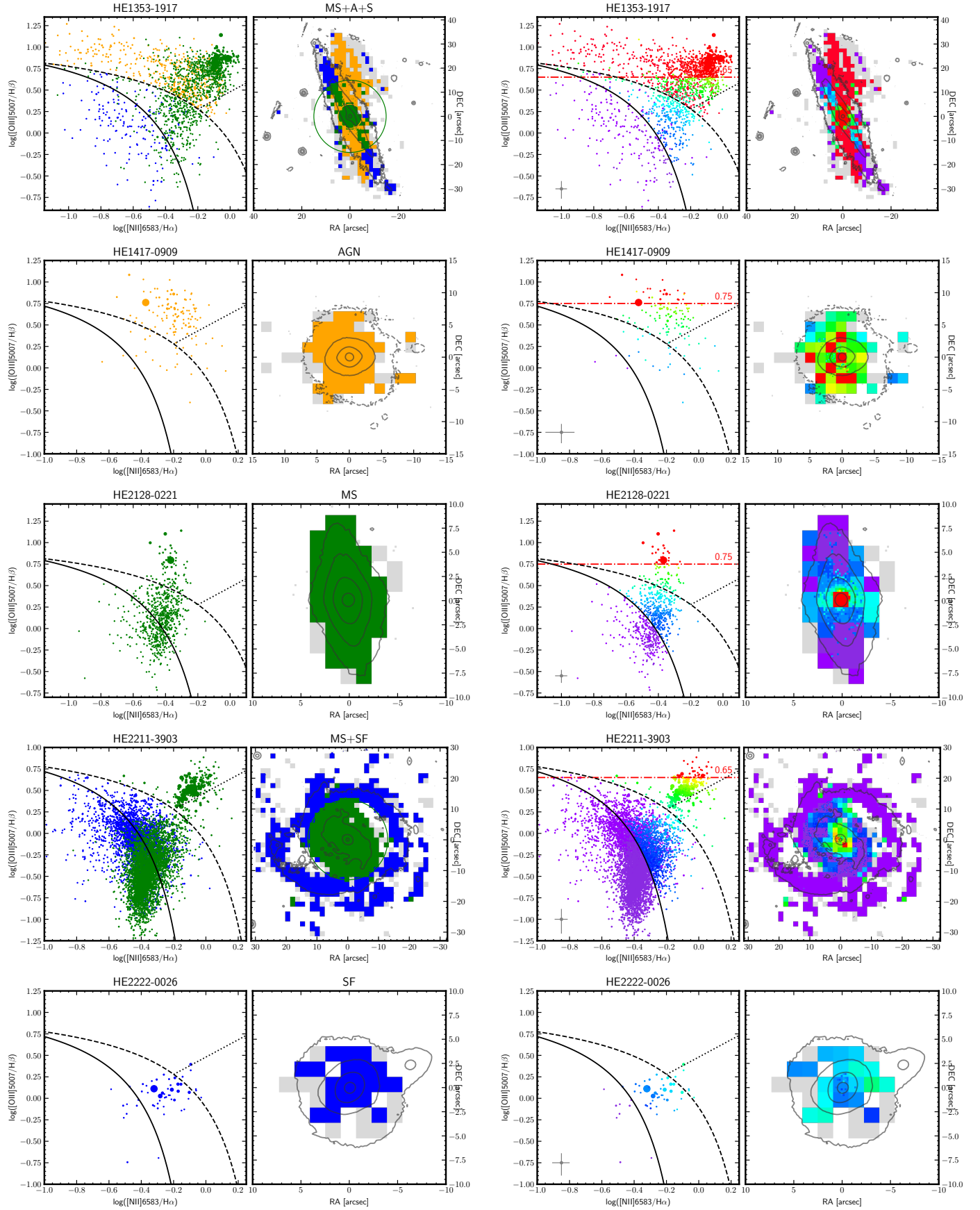**Fig. B.1.** continued.
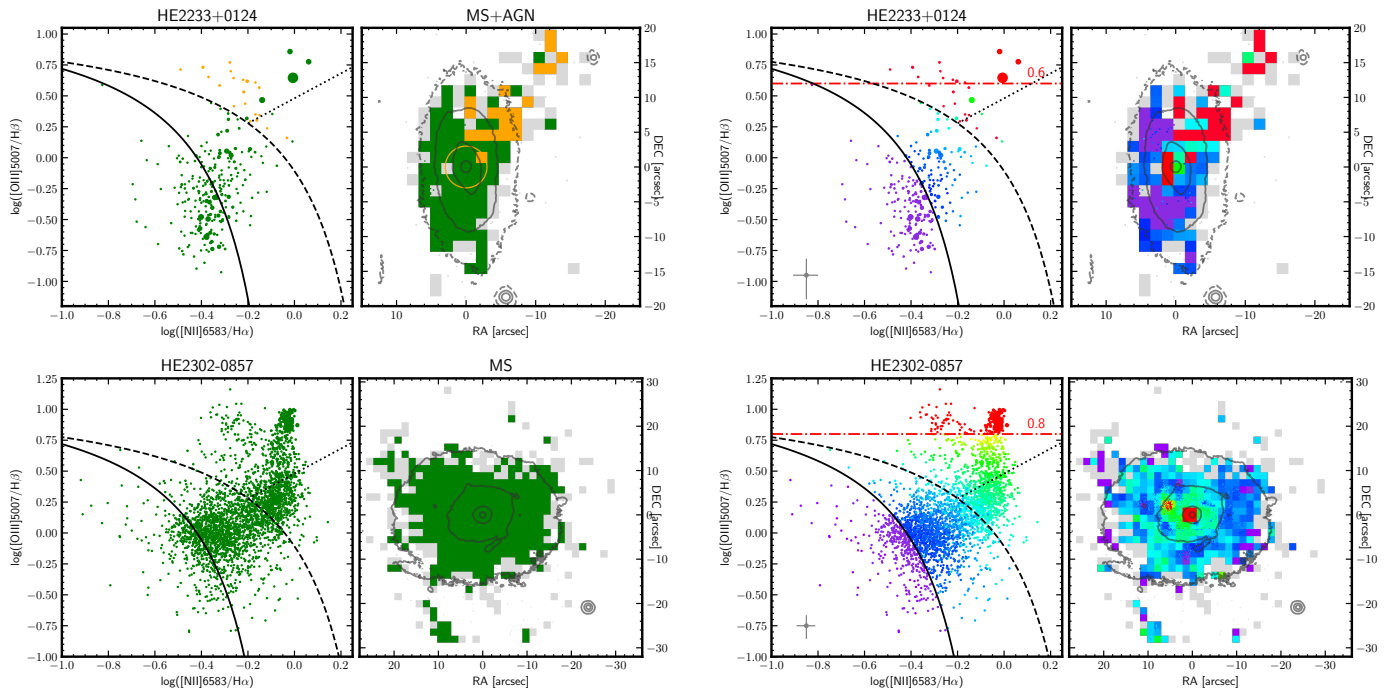
Fig. B.1. continued.

Fig. B.1. continued.

Fig. B.1. continued.

Appendix C: Metallicity maps
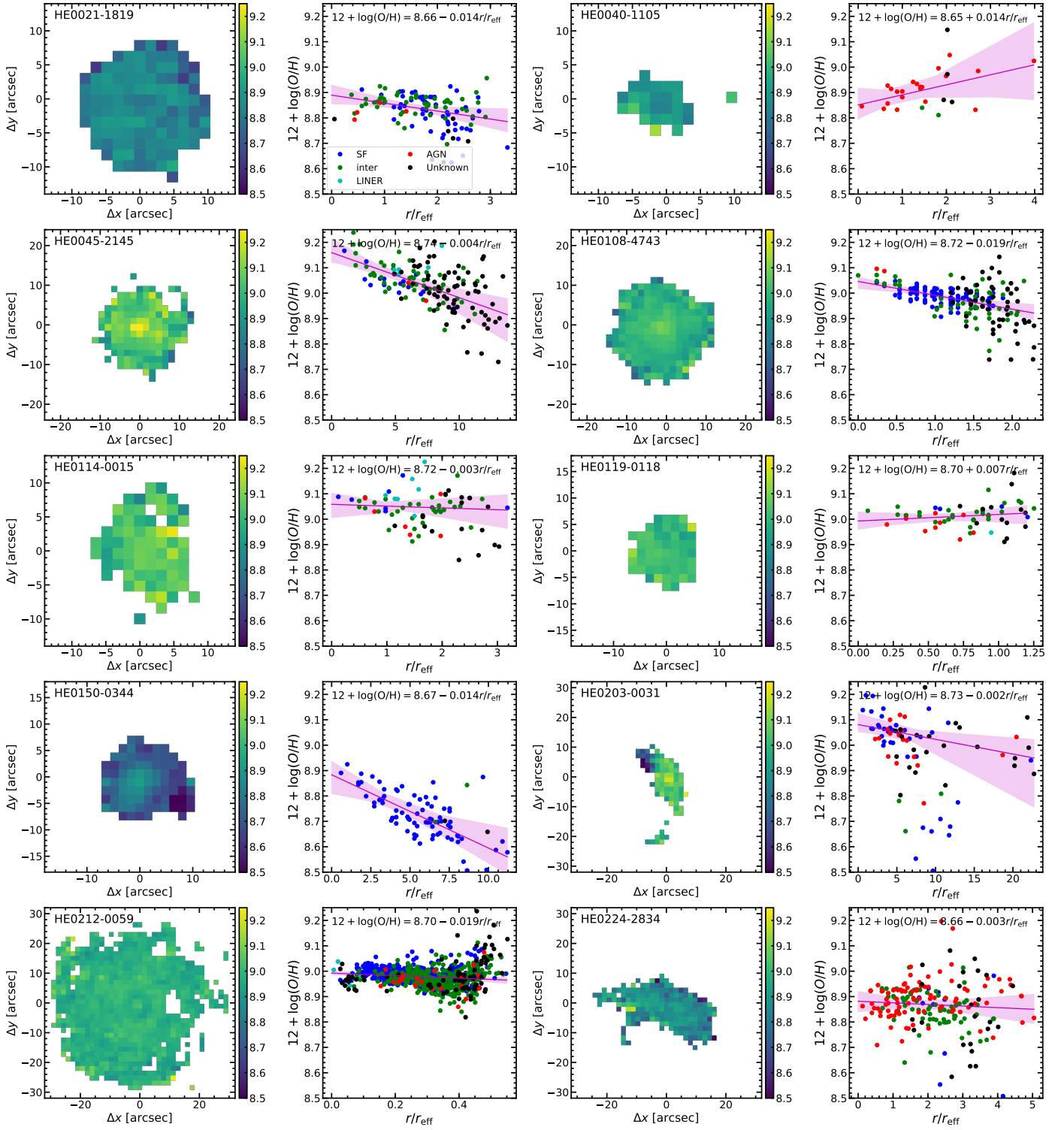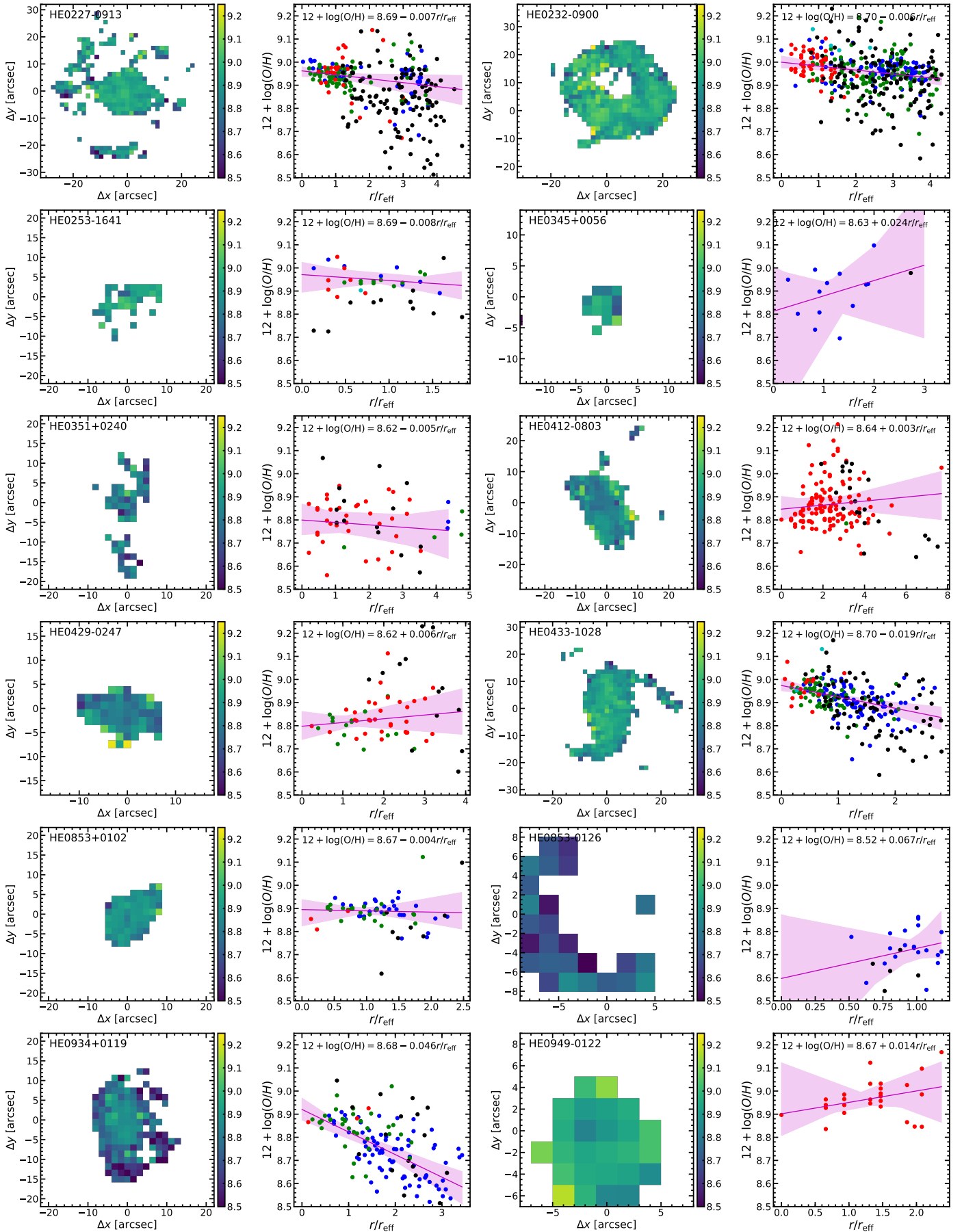

Fig. C.1. Same as Fig. 5 for the entire sample.

Fig. C.1. continued.

Fig. C.1. continued.

Fig. C.1. continued.